UNIVERSITY OF CALIFORNIA

SANTA CRUZ

THE EFFECT OF SEISMIC WAVES ON EARTHQUAKE NUCLEATION AND FAULT STRENGTH

A dissertation submitted in partial satisfaction
of the requirements for the degree of

DOCTOR OF PHILOSOPHY

in

EARTH SCIENCES

by

Nicholas J. van der Elst

June 2012

The Dissertation of
Nicholas J. van der Elst is approved:

_____
Professor Emily E. Brodsky, Chair

_____
Professor Thorne Lay

_____
Professor Noah Finnegan

_____
Tyrus Miller
Vice Provost and Dean of Graduate Studies

Table of Contents **Page**

List of Figures **Page**

The effect of seismic waves on earthquake nucleation and fault strength

by

Nicholas J. van der Elst

Abstract Seismic shaking during earthquakes is a potent reminder of the active tectonic processes shaping the surface of the Earth. In addition to their impacts on the surface, seismic waves can have an effect at depth, altering the conditions on fault zones and triggering other earthquakes. Here I study the effect of seismic waves on faults in order to probe the state of stress in the crust and to provide basic constraints on physical models of earthquake nucleation, propagation, and arrest. In the first section, I quantify the ability of seismic waves to trigger earthquakes, developing a new statistical metric based on changes in earthquake inter-event times. Triggering is identified in California at strain amplitudes down to 3×10^{-9}, and the triggered rate change scales with seismic wave amplitude. This scaling, projected into the near field of moderate magnitude earthquakes (M 3-5.5), can account for 15-60% of observed aftershocks. In the second section, I build on the statistical methods of section 1 to assess whether a recent increase in the global rate of great ($M_W \geq 8$) earthquakes can be attributed to dynamic triggering from other great earthquakes. Triggered rate changes are measured at the sites of each of the 16 $M_W \geq 8$ events that occurred between 1998 and 2011. In only a few cases is triggering detected at sites separated by more than 10º, and systematic rate changes are too small to account for the large increase in earthquake rate. These two sections together place lower and upper

bounds on the role of seismic waves in linking earthquakes across space and time. In the third section, I study the effect of seismic vibration on the sliding strength of an ongoing earthquake, using laboratory experiments to measure the effect of vibration on rapid granular shear flows. I find that noisy shear flows consisting of angular particles weaken and compact substantially at intermediate shear rates (0.1 - 10 cm/s). This compaction and weakening occurs in response to shear-generated acoustic vibration, and acts to counter shear-induced dilatational hardening. Acoustic compaction may be one of many processes contributing to co-seismic weakening of faults.

Acknowledgements

Chapter 1 of this thesis includes a reprint of the following published material:

van der Elst, N. J. and E. E. Brodsky (2010), Connecting near-field and far-field earthquake triggering to dynamic stain, *Journal of Geophysical Research*, 115, B07311, doi:10.1029/2009JB006671.

E. E. Brodsky directed and supervised the research that forms the basis for this chapter and those to follow.

Chapter 2 includes a preprint of material submitted for publication:

van der Elst, N. J., E. E. Brodsky, and T. Lay (*in review* 2012), Precursory remote triggering is absent near the epicenters of impending great earthquakes, *Bulletin of the Seismological Society of America.*

Co-author T. Lay provided research guidance and discussions that led to this paper.

Chapter 3 includes a preprint of material submitted for publication:

van der Elst, N. J., E. E. Brodsky, P.-Y. Le Bas, and P. A. Johnson (*in review* 2012), Auto-acoustic compaction in steady shear flows: Experimental evidence for suppression of shear dilatancy by internal acoustic vibration, *Journal of Geophysical Research.*

Co-authors P.-Y. Le Bas and P. A. Johnson were integral to the experimental component of this work, providing acoustic instrumentation and technical expertise.

Introduction

Earthquakes do not occur in isolation. They are connected along and across fault networks by elastic stresses transmitted through the crust and carried by seismic waves. This leads to clustering of earthquakes in time and space. Aftershocks and foreshocks, which cluster very nearby to a main shock in space and time, may be the most well known expression of this connection, however, stress transfer links earthquakes over longer time scales and greater distances as well. The physical agents responsible for earthquake clustering, or triggering, are several, including static elastic stresses from the earthquake dislocation, transient stresses carried by seismic waves, and viscous afterslip in the deep crust and upper mantle. In this thesis, I focus on the dynamic component of the stress field, that is, the ability of seismic waves to trigger other earthquakes and modify properties of the fault zone.

The study of earthquake interactions, or triggering, is valuable for two reasons. First, triggering provides a window into the strength of faults and the physics of earthquake nucleation. The stresses imparted by seismic waves can be estimated by direct observations of the shaking field, and elastic stresses can be estimated from models of the earthquake source. Given a known trigger, we can interpret the response of a fault zone in terms of laboratory analog experiments and physical models of earthquake nucleation. For instance, we can ask whether faults tend to be in a critically loaded state, such that they are easily pushed to failure by small stresses, or whether they are relatively stable with respect to short-lived perturbations in loading conditions.

However, much work remains to be done in understanding the link between dynamic stresses and earthquake nucleation, as dynamic triggering may involve a number of poorly constrained second-order effects in addition to the transient push toward frictional failure. Seismic waves may alter fault conditions through fluid pressure changes, permeability enhancement, compaction of gouge, and non-linear elastic effects. Understanding dynamic triggering requires both careful seismological observation and basic laboratory studies into the rheology of the fractured rock and granulated gouge that constitute a fault core.

The second reason to study earthquake triggering is that it may be the only viable avenue toward operational earthquake forecasting, where the seismic hazard in a region is estimated in real time based on the observed history of seismicity. Years of observation have not identified reliable short-term precursory phenomena, and current hazard estimates are primarily based on long-term recurrence intervals along major faults. This gives a reasonable estimate of the long-term baseline hazard posed by a fault, in as much as there must exist a long-term balance between tectonic loading and the release of elastic strain in earthquakes. However, earthquakes do not occur uniformly in time, but rather cluster in statistically describable ways. These clustering statistics, which arise from the underlying physical links between earthquakes, may be used to inform probabilistic assessments about future earthquakes.

Chapter 1: Quantifying earthquake triggering by seismic waves.

Statistical approaches that ignore the physical nature of the link between earthquakes have achieved some success in improving the forecasting of moderate magnitude (M5) earthquakes in some regions. It will take time, however, to evaluate whether meaningful reductions in seismic risk may be achieved with a purely statistical approach to operational earthquake forecasting. It is likely that more physically informed models of earthquake interactions will be necessary to truly bridge the gap between the simple statistical models and fault-based long term hazard models. Chapter 1 of this thesis seeks to answer one important question linking earthquake statistics to the physics of triggering: what proportion of near-field aftershocks are triggered by seismic waves? There are current efforts to develop forecasts by calculating static stress changes from simple source models of regional earthquake, and by simulating slip evolution on a geometrical model of the California fault network. These models do not incorporate the dynamic component of earthquake triggering, and may therefore fail to anticipate a sizeable fraction of clustered earthquakes. In this chapter, I quantify the effectiveness of seismic waves at triggering other earthquakes by developing a statistical method that associates changes in earthquake inter-event times to passing seismic waves. I calibrate the triggered rate change as a function of amplitude for distant earthquakes where the triggering agent is known to be seismic waves. Projecting this far field empirical relationship into the near field of moderate-magnitude earthquakes ($M \leq 5.5$), I estimate that a significant fraction (15-60%) of the aftershocks at all distances may be

dynamically triggered. Since the intensity of shaking can be physically observed with seismograms, this information could improve physics-based statistical forecasting.

Chapter 2: Do seismic waves trigger very large earthquakes?

One of the conclusions of Chapter 1 is that, for large enough earthquakes, the reach of dynamic triggering is essentially global. In fact, up to a 1 or 2% of the earthquakes that fall within the borders of California may be triggered by earthquakes so distant that the shaking is noticed only by seismometers. In Chapter 2, I take the implications of this conclusion to the logical limit and ask whether recently increased rates of large devastating $M \geq 8$ earthquakes can be attributed, at least in part, to strong shaking from earlier earthquakes. The last decade has seen an excess of large ($M \geq 8$) earthquakes relative to the decades prior, and the increase in rate seems to coincide with the occurrence of the M9 Sumatra earthquake in 2004. This earthquake – the largest in over 40 years – generated shaking levels around the globe that were found in Chapter 1 to be sufficient to trigger small sequences of triggered quakes in susceptible regions. The statistics of earthquakes interactions suggest that it may be possible for some of these small remotely triggered earthquakes sequences to trigger local aftershocks of their own, which may eventually culminate in an even larger event. Is it possible that the occurrence of very large earthquakes could also be linked through seismic waves? If triggering of great earthquakes occurs via a cascade of smaller triggered events, there should be clear evidence of triggered small earthquakes at the sites of impending large earthquakes. In Chapter 2, I search

systematically for this fingerprint, using the statistical method developed in Chapter 1. Although some small rate changes are possible, I find no evidence of precursory triggered rate changes of a magnitude sufficient to explain the global increase in rate of great earthquakes. I conclude that recent clustering either reflects random variability in earthquake occurrence, or must be explained by a physical mechanism other than a cascade of triggering initiated dynamically by distant earthquakes.

Chapter 3: Seismic waves and the co-seismic strength of fault gouge.

In Chapters 1 and 2, I examine the effect of seismic waves on earthquake nucleation and global seismicity rates. In Chapter 3, I ask a different sort of question: what is the effect of seismic waves on the fault zone of the earthquake that generates them? Faults are not simple planar features in otherwise intact rock. Instead, faults are filled with fractured, crushed, and granulated gouge produced during fault growth and slip. Such materials are not governed simply by frictional or plastic failure, but rather exhibit a rich range of behavior depending on experimental conditions, boundary conditions, and shear rate. In particular, vibration can have a strong effect on the rheology of a granular flow. If we are to understand how seismic waves trigger earthquakes, as observed in Chapter 1, we must first understand the strength of granular media in the presence of vibration.

Much basic work needs to be done to characterize the rheological behavior of granular flow. While continuum models of granular flow have been somewhat

successful in describing the flow for a range of geometries, a universal constitutive law for granular flow remains elusive. One of the key reasons that granular flow is difficult to model with continuum theories is that granular shear flows are strongly heterogeneous and anisotropic in stress, developing networks of force chains that concentrate stresses on some grains while shielding others. The rheology of a granular flow is strongly dependent not only on the packing density, but on the precise arrangement of grains.

In Chapter 3, I report on basic experiments designed to isolate the effect of acoustic vibration on the strength of a granular flow. In these experiments I evaluate the tradeoff between two opposing grain-arrangement effects: shear dilatation, in which grains climb over each other and cause the sample to dilate, and acoustic compaction, in which grains settle into voids and cause the sample to compact under low amplitude vibration. I measure the noise produced during shear and evaluate how this shear-induced vibration may limit the amount of shear dilatation. I show that seismic vibration generated within the fault zone during slip may reduce the coseismic strength of a fault through this mechanism.

Future Directions

The statistical studies contained in Chapters 1 and 2 rely heavily on earthquake catalogs. This is because the statistics are most easily applied to event-based time series, collected consistently over long time periods. Earthquake catalogs are not,

however, the most complete record, especially during the passage of large amplitude seismic waves. Other researchers have had some success using filtered waveforms to detect triggered earthquakes that are missing from the catalogs. The methods developed in this thesis can be extended quite easily to continuous waveform data, as long as small earthquakes can be identified reliably on single seismogram traces. High-quality continuous waveform data had become much more common and accessible in recent years, and the recent occurrence of some large earthquakes in well-instrumented regions (e.g. New Zealand, Baja California, Tohoku) provides a good opportunity to conduct focused regional studies of earthquake triggering using continuous waveforms.

The granular flow and acoustic vibration experiments in Chapter 3 have isolated a particular mechanism that affects granular rheology. These experiments contribute to our basic physical understanding of shear flows of crushed and granulated rock. In order to extend this mechanism confidently to fault zones, however, a number of additional experiments are called for. The experiments should be repeated at higher stresses, under different boundary conditions, and for a wider range of materials with particle size distributions more representative of actual fault zones. The acoustic rheology should also be characterized in the presence of pore fluids and elevated pore pressures.

Chapter 1. Connecting near and farfield earthquake triggering to dynamic strain

Nicholas J. van der Elst and Emily E. Brodsky

Department of Earth and Planetary Science, University of California, Santa Cruz

Abstract: Any earthquake can trigger more earthquakes. This triggering occurs in both the classical aftershock zone, as well as the farfield. These populations of triggered earthquakes may or may not be distinct in terms of triggering mechanism. Here we look for a distinction between the populations by examining how the observed intensity of triggering scales with the amplitude of the triggering strain in each. To do so, we apply a new statistical metric based on earthquake interevent times to a large dataset and measure earthquake triggering as a function of dynamic strain amplitude, where strain is estimated from empirical ground motion regressions. This method allows us to identify triggering at dynamic strain amplitudes down to 3×10^{-9}, orders of magnitude smaller than previously reported. This threshold appears to be an observational limit, and shows that extremely small dynamic strains can trigger faults that are sufficiently near failure. Using a probabilistic model to transform measured interevent times to seismicity rate changes, we find that triggering rates in the farfield scale with peak dynamic strain. This scaling, projected into the nearfield, accounts for 15-60% of earthquakes within 6 km of magnitude 3-5.5 earthquakes. Statistical seismicity simulations validate the interevent time method, and show that the data are consistent with the number of farfield triggered earthquakes being linearly

proportional to peak dynamic strain. We interpret the additional nearfield component as reflecting either static stress triggering, more effective dynamic triggering at higher frequencies, or a concentration of aftershock nucleation sites very near mainshocks.

1-1. Introduction

Triggered earthquakes provide a window into the physics of earthquake nucleation because the forces initiating rupture can be inferred. Because the strain at which a fault is triggered is a measure of its strength, it may be possible to gain insight into the distribution of fault strength by studying the statistics of earthquake triggering [*Brodsky and Prejean*, 2005; *Gomberg*, 2001].

One strategy for ultimately determining the processes involved in triggering is to first identify the stresses that activate the process. The types of stresses that have been proposed as the agents by which one fault transmits a triggering signal to another include coseismic static strain changes, progressive postseismic strain changes (including afterslip and viscous creep), and dynamic strains from radiated seismic waves [*Freed*, 2005]. These agents may each trigger earthquakes through a number of mechanisms, including direct Coulomb frictional failure, reduction in fault strength, and pore fluid pressure changes. Different triggering agents may be expected to be relatively more or less effective at activating different failure mechanisms. Therefore, understanding the relative contribution of triggering agents may help constrain triggering mechanisms.

The proposed triggering agents have different strengths and weaknesses in explaining observed triggering. Coseismic static strain changes are the increase or decrease in strain at one fault due to the relaxation of strain at another during an earthquake. Static strain changes are permanent and therefore can easily explain triggering for an extended period of time [*King et al*., 1994], but the stresses decay in amplitude quickly with distance away from a fault and are thus unlikely to trigger distant earthquakes. Multiple stress interactions, i.e. secondary triggering, or aftershocks of aftershocks, can extend the reach of static stresses to a few times the length of the primary rupture [*Ziv*, 2003], but not to the tens of times observed for remote triggering [*Hill et al*., 1993]. Postseismic static strain changes are generated by afterslip or lower crustal ductile creep and also produce prolonged stresses. Afterslip produces a quasi-static nearfield stress change that has comparable distance decay to coseismic static stress changes and thus cannot explain triggering at great distances. Viscous deformation can propagate to great distances but takes years to reach hundreds of kilometers [*Freed and Lin*, 1998; *Pollitz et al*., 1998], and thus cannot explain distant triggering that is sometimes seen within days or even seconds [*West et al*., 2005]. Dynamic triggering is associated with transient strains carried by radiated seismic waves [*Hill and Prejean*, 2007]. Dynamic strains decay less quickly with distance, and therefore do well at explaining remote triggering, but present a challenge in explaining prolonged triggering [*Brodsky*, 2006; *Gomberg*, 2001].

The above summary highlights that there is more certainty about the agent of triggering for a special subset of earthquake triggering: distant triggering over timescales of less than a few years. These remotely triggered earthquakes are believed to result entirely from dynamic triggering, both because static strains are negligible at large distances, and because distant triggering often coincides with the arrival of surface waves [*Anderson et al*., 1994; *Brodsky et al*., 2000; *Gomberg and Johnson*, 2005; *Hill et al*., 1993]. On the other hand, short-range triggering is much more ambiguous, and has been attributed to static, postseismic, or dynamic agents by different researchers [*Felzer and Brodsky*, 2006; *Gomberg et al*., 2003; *Kilb et al*., 2000; *Perfettini and Avouac*, 2007; *Pollitz and Johnston*, 2006; *Stein et al*., 1994; *Velasco et al*., 2008]. Spatial correlations between calculated coseismic static stress fields and aftershock patterns appear to support coseismic static stress triggering [*King et al*., 1994; *Stein et al*., 1994]. On the other hand, correlations between temporal aftershock evolution and geodetic strain measurements support progressive postseismic strain [*Freed and Lin*, 1998; *Peng and Zhao*, 2009; *Perfettini and Avouac*, 2007]. Still other studies that compare nearfield aftershock locations to the static and dynamic strains for earthquakes with strong directivity conclude that dynamic strains correlate better with the ensuing seismicity [*Gomberg et al*., 2003; *Kilb et al*., 2000].

In this study, we exploit the understanding that dynamic strain is the dominant triggering agent at large distances and relatively short timescales in order to constrain

the contribution of additional triggering agents in the nearfield. We first determine an empirical relationship between a measure of triggering intensity and peak dynamic strain in the farfield, based on the waiting time to early triggered earthquakes. Then we compare this farfield relationship to nearfield observations to assess the proportion of nearfield earthquakes that can be explained by the farfield proportionality. We ultimately find that dynamic triggering can account for a significant portion of nearfield aftershocks, but that there is an additional triggering component in the nearfield. Whether this reflects additional triggering agents (e.g. static strain, afterslip) or the effect of second-order aspects of the dynamic strain (e.g. duration, frequency) we cannot resolve. In the process, we develop a measure of earthquake triggering that is significantly more sensitive to low triggering rates than previous measures and place a new bound on the threshold for farfield dynamic triggering.

The first several sections of this article concern the development of the triggering metric. First, we define a statistic based on earthquake interevent times and establish the expectation for this statistic, assuming a simple probabilistic model for earthquake occurrence times. Next, we delineate populations on the basis of local dynamic strain and describe the data selection and processing. We then apply the method and show that the dynamic triggering relationship determined for farfield quakes can account for roughly half of nearfield aftershock triggering. We also report a new estimate on the dynamic triggering threshold in California of 3×10^{-9} strain, several orders of

magnitude lower than previous estimates. A statistical seismicity simulation is then used to interpret and validate the results. Finally, we evaluate the implications and robustness of the results.

1-2. Measuring earthquake rate changes using interevent times

A comparison of triggering rates in the near and farfield requires a metric that can be applied to both populations of earthquakes. This metric needs to be sensitive enough to detect the very small triggering rates associated with the very small dynamic strains common to the farfield. Previously, triggered earthquakes have been identified by inspecting seismicity rates [*Harrington and Brodsky*, 2006; *Hill et al*., 1993; *Stark and Davis*, 1996] or by filtering waveforms to emphasize short-period energy within the surface wave trains of large, distant earthquakes [*Brodsky et al*., 2000; *Hill and Prejean*, 2007; *Velasco et al*., 2008]. Quantitative estimates of triggering usually involve calculating the likelihood of observing a number of post-trigger events given the previous seismicity rate [*Anderson et al*., 1994; *Gomberg et al*., 2001; *Hough*, 2005]. If the likelihood of the rate increase occurring by chance is low enough, triggering is inferred.

Any estimate that computes likelihood of triggering based on counting the number of triggered earthquakes relative to a pre-trigger count, like the β-statistic [*Matthews and Reasenberg*, 1988], is limited in several ways. First, the pre-trigger seismicity rate must be resolved for comparison, and this is inherently difficult. Because most

earthquakes occur as clusters of aftershocks, the seismicity rate is always changing. Background seismicity level should therefore be measured at a time as close to the purported trigger as possible in as short a window as possible. Different areas will permit different length windows depending on their background level of seismicity, and thus a constant window for an entire dataset may not sufficiently capture the data. Second, an earthquake count can only resolve an integer increase in the number of earthquakes for any individual sequence. A slight advancement in the timing of subsequent earthquakes will only rarely result in an additional triggered earthquake within the counting time window, so only large levels of triggering can be resolved with statistical significance. Finally, an earthquake count also includes all secondarily triggered earthquakes, that is, aftershocks of aftershocks. These secondary earthquakes are not strictly problematic, because they should still be produced in proportion to the number of primary triggered earthquakes when averaged over many events, but they complicate the relationship between trigger amplitude and number of triggered quakes by introducing variance into the measurements.

To detect triggering at very low dynamic strain amplitudes, our metric must use an adaptive time window to measure background rates, be sensitive to small increases in seismicity rates, and be insensitive to secondary aftershocks.

1-2.1 The interevent time ratio *R*

We meet the above requirements by developing a statistic based only on the interevent times between the last earthquake before a trigger and the first earthquake after. We define the interevent time ratio R as

$$R \equiv \frac{t_2}{t_1 + t_2}, \tag{1-1}$$

where t_1 and t_2 are the waiting times to the first earthquake before and after the putative trigger (Figure 1-1). The interevent time ratio R was originally developed to study triggered quiescence [*Felzer and Brodsky*, 2005]; we use it here to look for a triggered rate increase.

Because R is normalized by the average seismicity rate at the time of the trigger, we can pool and compare measurements made within a highly heterogeneous earthquake catalog. The strategy in this study is to measure the distribution of R on a population of earthquakes that are subject to similar triggering conditions. For instance, the population can be a drawn from a variety of areas subject to the same dynamic strain. The metric R

is a random variable distributed between 0 and 1. If there is no triggering in the population, and t_2 is on average equal to t_1, then R is distributed uniformly with a mean value $\bar{R} = ½$. On the other hand, if triggering does occur, t_2 will be on average smaller than t_1 and $\bar{R} < ½$. More triggering results in a smaller $\bar{R}$ (Figure 1-2). Therefore, the statistic $\bar{R}$ provides a measure of triggering intensity within a population of earthquakes.

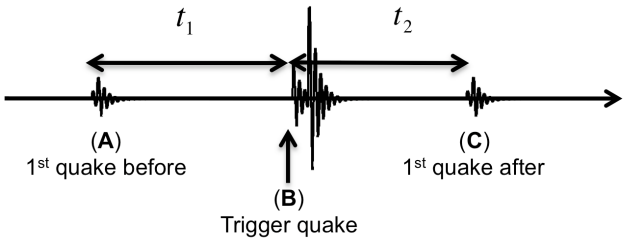

Figure 1-1. Cartoon timeline illustrating the variables contributing to the interevent time ratio R (Equation 1-1). The trigger earthquake is labeled (B), and the first earthquake before and after the trigger are labeled (A) and (C), respectively. The time t_1 is the time to the first earthquake before the trigger, and t_2 is the waiting time to the first earthquake after the trigger.

The interevent time ratio R naturally solves the three problems identified with earthquake counting methods by defining an appropriate time window for each event based on the interevent times, utilizing the statistics of large populations, and focusing on the first recorded earthquake rather than the entire triggered sequence.

One of the unusual features of the interevent time method is that there is no time limit for the inclusion of triggered events. Both instantaneous and delayed triggering are included in the measurements. This comprehensiveness is desirable because of issues of catalog completeness, as well as the physical implications of delayed triggering. Instantaneous triggering ($t_2 \sim 0$) should be reflected in the R distribution as a strong spike at $R \sim 0$ with a uniformly depressed probability density at higher values. Delayed triggered ($0 < t_2 < t_1$), should cause the spike to be spread out to larger R-values (e.g. Figure 2). In principle, the distribution of R should therefore reflect the time-decay of the triggered rate change. For the purposes of this study, however, we

restrict ourselves to calculations involving the sample mean $\overline{R}$ and do not consider the precise shape of the distribution. We will return to the issue of delayed triggering at the end of the paper after the metric has been implemented.

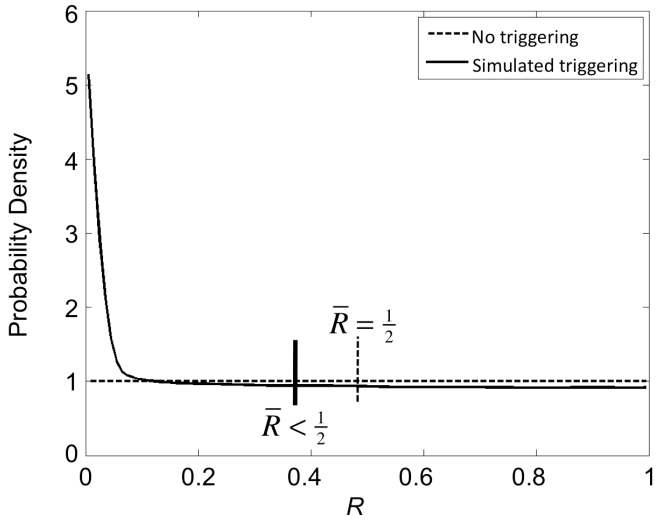

Figure 1-2. Schematic cartoon illustrating the distinction between the distribution of R in a case with no triggering (dashed) and a simulated case of strong triggering (solid). The integral of the probability density is 1 in both cases. The mean value of R is 0.50 in the non-triggered case and 0.46 in the triggered example.

1-2.2. Interpreting *R* as seismicity rate change

The purpose of this study is to compare dynamic triggering levels in farfield and nearfield populations of triggers. However, the range of dynamic strain amplitudes observable in each population is different, at least in the California study region focused on here. This is because even the largest farfield earthquakes generate only low amplitude waves at great distances – so small that equivalent nearfield triggers are too low in magnitude to be detected in regional catalogs. Consequently, we

measure the scaling of $\overline{R}$ with dynamic strain in each population and compare the respective trends. Because $\overline{R}$ must asymptote to 0.5 for zero rate change and to 0 for extreme rate increases, $\overline{R}$ must scale nonlinearly with rate change. This nonlinearity complicates the comparison of trends between the two dynamic strain ranges. In order to compare triggered rate changes in the two populations, we first establish the expected behavior of $\overline{R}$ as a function of rate change.

To derive the expectation of R as a function of seismicity rate change, we use a model that relates interevent times to earthquake rate. If earthquake occurrence were perfectly periodic and uniform, the expectation of R would follow directly from Equation 1-1 with t_1 and t_2 equal to the inverse of the earthquake rate. However, earthquakes are for the most part not periodic. Detailed studies of earthquake catalogs find that the distribution of interevent times is best characterized by a combination of Poisson distributed background earthquakes and triggered aftershocks that decay in time according to Omori's law [*Corral*, 2004; *Gardner and Knopoff*, 1974; *Hainzl et al*., 2006; *Molchan*, 2006; *Saichev and Sornette*, 2006]. The time decaying Omori's law component can be considered a nonhomogeneous Poisson process, that is, a Poisson process where the intensity is a function of time. This is a standard model for aftershock forecasting and is frequently used to analyze the significance of earthquake triggering metrics [*Kagan and Jackson*, 2000; *Marsan*, 2003; *Matthews and Reasenberg*, 1988; *Ogata*, 1999; *Reasenberg and Jones*, 1989; *Wiemer*, 2000].

We use it here to determine the expectation of R as a function of triggered rate change.

Calculating the expectation of R for this nonhomogeneous Poisson process requires an estimate of the background rate and the parameters in Omori's law (Appendix 1-A). These parameters may be heterogeneous in time and space and are impossible to determine for the single earthquakes that go into measurements of R. However, since we deal only with single earthquakes before and after the trigger, the details of the underlying interevent time distribution are relatively unimportant. Rather, we expect R to be primarily sensitive to average rates. This restricted sensitivity allows us to approximate the nonhomogeneous process as a simple stepwise homogeneous process, characterized by an average rate λ_1 before the trigger and a new average rate λ_2 afterward. For the stepwise homogeneous Poisson process, the expectation of R is given by (Appendix 1-A)

$$\langle R \rangle = \frac{1}{n^2}\left[(n+1)\ln(n+1) - n\right], \tag{1-2}$$

which is a function only of the normalized difference in average rate, or fractional rate change,

$$n \equiv \frac{\lambda_2 - \lambda_1}{\lambda_1}. \tag{1-3}$$

As anticipated, the expectation of R scales nonlinearly with rate change for the three models mentioned above: periodic, nonhomogeneous Poisson, and step-wise homogeneous (Figure 1-3).

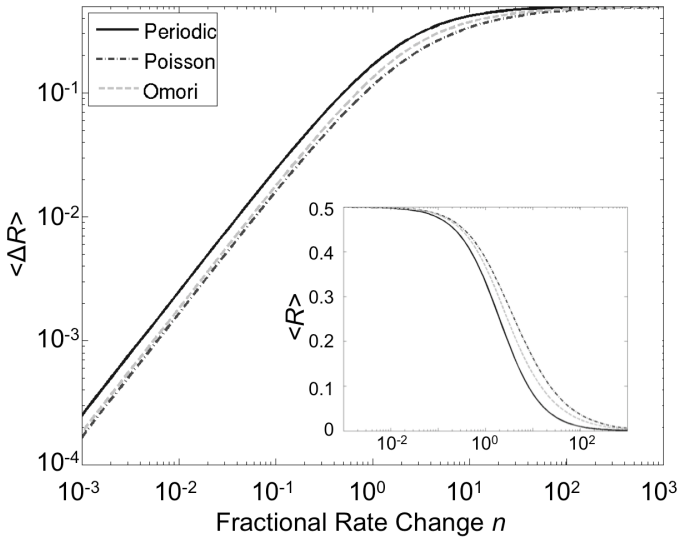

Figure 1-3. Expectation of R (Equation 1-A10), i.e. predicted $\bar{R}$, as a function of fractional rate change for three probabilistic models for earthquake occurrence, as described in the text. 'Omori' refers to the nonhomogeneous Poisson model with Omori decay in triggered rate change. Inset shows the expectation of R on a linear-log scale, while the larger figure shows the value $\langle \Delta R \rangle = 0.5 - \langle R \rangle$ on a log-log scale to emphasize the scaling at small fractional rate changes, like those sought in this study. Fractional rate change is the normalized triggered earthquake rate defined in Equation 1-3. The curves are all very similar, especially similar for small rate change.

To emphasize the scaling for the small fractional rate changes, Figure 1-3 shows both the value of $\langle R \rangle$ and $\langle \Delta R \rangle \equiv 0.5 - \langle R \rangle$. The stepwise homogeneous model is found to be an excellent approximation of the more complex nonhomogeneous model, especially for the small rate changes we expect to deal with in this study. This

demonstrates that the metric R is primarily sensitive to average seismicity rate change, rather than the details of the interevent time model.

As stated above, the nonlinearity in the scaling of $\bar{R}$ complicates the assessment of continuity between discontinuous farfield and nearfield populations. We can address this complication by transforming the observations, using Equation 1-2 to map the measured $\bar{R}$ into a modeled fractional rate change n. That is, we can interpret the measured $\bar{R}$ in terms of the number of triggered earthquakes required to produce that $\bar{R}$. Although we had no *a-priori* expectation for the scaling of $\bar{R}$ with dynamic strain, we do have an expectation for the scaling of n with dynamic strain. Studies of traditional aftershock zones have found that the number of aftershocks scales with mainshock magnitude as $\log N \propto M$ [*Felzer et al*., 2004; *Gasperini and Lolli*, 2006; *Helmstetter et al*., 2005; *Ogata*, 1992; *Yamanaka and Shimazaki*, 1990]. Since peak ground velocity (a proxy for dynamic strain) also scales with magnitude as $\log PGV \propto M$, the aftershock scaling with magnitude is consistent with a power-law scaling of aftershock rate with dynamic strain. Studies comparing aftershock rates directly to peak ground velocities suggest that aftershock rates may even be linearly proportional to dynamic strain, i.e. with a power-law exponent of ~1 [*Gomberg and Felzer*, 2008]. If our probabilistic model (Equation 1-2) is adequate, and assuming that at least the more conservative power-law scaling hypothesis holds, then the transformed statistic n should scale linearly on a log-log scale. In Section 1-4 we will

show that this hypothesis is confirmed by the data. This gives us the tool we need to compare relative triggering rates in near and farfield populations.

In what follows, we refer to n as triggering intensity, to emphasize that it is a transformed statistic and not a direct measurement of fractional rate change. Nevertheless, Equation 1-2 represents a smoothly continuous transformation, and therefore the transformed statistic n should not scale continuously with dynamic strain amplitude unless the primary statistic $\bar{R}$ does so as well.

1-3. Defining Populations

The statistic $\bar{R}$ (or the transformed statistic n) measures triggering intensity in a population of earthquakes. Therefore, the first step in applying the interevent time method to a real dataset is to define reasonable populations so that we can evaluate the different rate changes in each one.

Because long-range triggering is clearly associated with dynamic strain, we start by constructing sets of earthquakes with common dynamic strain amplitude. Other aspects of the seismic waves may be important in terms of triggering earthquakes, such as duration or frequency of the seismic waves. For instance, some studies suggest that higher frequency waves are more effective triggers [*Gomberg and Davis*, 1996], while some attribute more triggering power to lower frequencies [*Brodsky and Prejean*, 2005]. Other studies find that frequency or number of oscillation cycles may

modulate triggering power slightly, but these aspects are of secondary importance to peak amplitude [*Savage and Marone*, 2008]. Comparison between radial aftershock decay and ground motion attenuation at intermediate distances supports a scaling with peak or average ground velocities, independent of duration [*Gomberg and Felzer*, 2008]. Given the uncertainties regarding other aspects of the seismic waves, we choose to define populations based only on peak amplitude. Observed differences between near and farfield triggering intensities may therefore be attributed to second-order aspects of the wave field, and not only to other triggering agents such as static and postseismic strain.

Peak dynamic strain is roughly proportional to the amplitude of seismic waves

$$\varepsilon \approx \frac{A}{\Lambda} \approx \frac{V}{C_S}, \tag{1-4}$$

where A is displacement amplitude, Λ is wavelength, V is particle velocity and C_S is seismic wave velocity [*Love*, 1927]. In principle, dynamic strain can therefore be calculated wherever there is a seismogram. In this study, we use empirical ground motion regressions to approximate seismic wave amplitude, allowing us to extend strain estimates to any point on the map. Ground motions are converted to dynamic strain estimates by dividing by wavelength or wave speed, depending on whether the regression is for displacement or velocity, respectively.

In the nearfield, S-waves should carry the largest dynamic strains, with a dominant period on the order of 1 second [*Boatwright et al*., 2001]. S-wave velocity at seismogenic depths is roughly 3.5 km/s. In the farfield, surface waves with periods near 20 seconds dominate ground motion, as smaller period waves tend to be scattered and attenuated [*Lay and Wallace*, 1995]. Both Love and Rayleigh waves can trigger earthquakes [*Hill*, 2008; *Velasco et al*., 2008], but the 20 second Rayleigh wave, with a velocity of ~3.5 km/s, is usually associated with the surface wave magnitude equation we use to estimate peak ground motions [*Lay and Wallace*, 1995]. We therefore treat this phase as representative of farfield dynamic strains. We note that if triggering is in fact dominated by Love waves, with a velocity of ~4.3 km/s, Equation 1-4 may overestimate strain by ~20% for equivalent amplitude waves.

Previous work has investigated the accuracy of using ground motions as a proxy for dynamic strain at depth by comparing strain estimated from seismometer data to strain measured by strainmeters [*Gomberg and Agnew*, 1996]. This study found that although there was considerable deviation in observed strains from those expected for a simple layered earth model, the dynamic strain amplitudes calculated from ground motions generally agreed within ±20% of the strainmeter measurements for periods between ~10-25 seconds, and within ±50% outside this band. These uncertainties are smaller than the factor of 2 uncertainties related to the empirical regressions used to estimate peak ground motions (see below). Since we are interested in the first-order scaling of triggering intensity with dynamic strain amplitude averaged over many

earthquakes, we consider peak ground motions to be an adequate order-of-magnitude proxy for peak dynamic strains.

1-3.1. Estimating dynamic strain with empirical ground motion regressions

In order to take full advantage of the large number of earthquakes in the catalog, we must calculate dynamic strain at any point on the map for any trigger in the catalog, not only where we have seismic stations and archived waveforms. We therefore use empirical ground motion regressions to estimate strain as a function of distance from the potential trigger earthquakes. Peak ground motions are well studied at near and intermediate distances for estimating seismic hazard, and at regional and teleseismic distances for calibrating magnitude scales [*Abrahamson and Silva*, 2008; *Boatwright et al*., 2003; *Campbell and Bozorgnia*, 2007; *Joyner and Boore*, 1981; *Lay and Wallace*, 1995; *Richter*, 1935]. However, published regressions rarely focus on the very nearfield distances and small magnitudes of interest in this study, and are insufficient for our purposes. Previous researchers comparing aftershock distribution to peak ground motions have performed their own regressions with an emphasis on the nearfield [*Gomberg and Felzer*, 2008]. We also perform our own small-magnitude, nearfield PGV regression, using California Shakemap data [*Wald et al*., 1999]. Boatwright [2003] also used Shakemap data to make an empirical ground motion regression, but used only a small subset of the data available today and did not focus on the small distances of interest in this study.

For the nearfield regression, we follow the Next Generation Attenuation study of Campbell and Bozorgnia [2007] and use an equation of the form

$$\log_{10} \mathrm{PGV} = c_1 + c_1 M - c_3 \log_{10} \sqrt{r^2 + c_4^2} \,, \tag{1-5}$$

where PGV is peak ground velocity in cm/s, M is earthquake magnitude, r is hypocentral distance in km, and c_i are fit parameters. The fit parameters are found by regression analysis using ~2000 PGV measurements from the Shakemap archives (Table 1-1). The details of the regression are given in Appendix 1-B.

For farfield dynamic strain we use the surface wave magnitude relation [*Lay and Wallace*, 1995],

$$\log_{10} A_{20} = M_S - 1.66 \log_{10} \Delta - 2 \,, \tag{1-6}$$

where A_{20} is in μm and Δ is in degrees. This equation is commonly used to assign a catalog magnitude based on measured amplitude at some distance. We turn the procedure around and use the catalog magnitude to calculate amplitude. This approach uses the long-period waves (T = 20 s) as indicators of the peak dynamic strain, implicitly assuming that the short-period body waves are attenuated at large distances. The displacement A is converted to velocity for the 20 second waves by the approximation $V \approx 2\pi A_{20}/T$ [*Aki and Richards*, 2002]. Equation 1-6 was historically calibrated using a similar catalog of global earthquakes to the one we use for potential triggers, and so provides a good measure of average amplitude despite being imperfect for any individual earthquake. The standard magnitude error for this

regression, reflecting both inter-event variations (e.g. source depth) and intra-event variations (e.g. radiation pattern), has been tabulated for a selection of seismic stations [*Rezapour and Pearce*, 1998], and we compute a pooled standard error of 0.28 units. Through Equation 1-6, this corresponds to a factor of ~2 uncertainty in the estimated strain amplitude. The surface wave magnitude equation is designed for distances on the order of at least 800 km [*Lay and Wallace*, 1995] and this sets the minimum distance for the population of long-range triggers in this study.

Table 1-1. PGV regression parameters (with 95% confidence bounds), Equation 1-5.

	c_1	c_2	c_3	c_4 (km)
Unconstrained	-2.29 (-2.79, -1.80)	0.85 (0.75, 0.96)	1.29 (1.58, 1.00)	0 (0, 0)
Constrained (c_2=1)	-2.83 (-3.13, -2.56)	1	1.34 (1.59, 1.03)	0 (0, 0)

1-3.2. Defining populations over space

A large farfield quake may trigger numerous earthquakes distributed throughout the study area. We therefore split the study region into spatial bins and calculate *R* for each of these bins (Figure 1-4). This generates a number of *R*-values for each trigger and ensures that the measurements are not dominated by any single region with particularly high activity. Using a spatial bin that is much smaller than the wavelength of the long-range trigger also ensures that measured triggering intensity reflects the dynamic strain at that site. These *R*-values are then pooled according to peak dynamic strain as calculated by Equation 1-6, rather than according to their particular trigger.

In this way, each strain bin incorporates numerous triggers at various combinations of distance and magnitude.

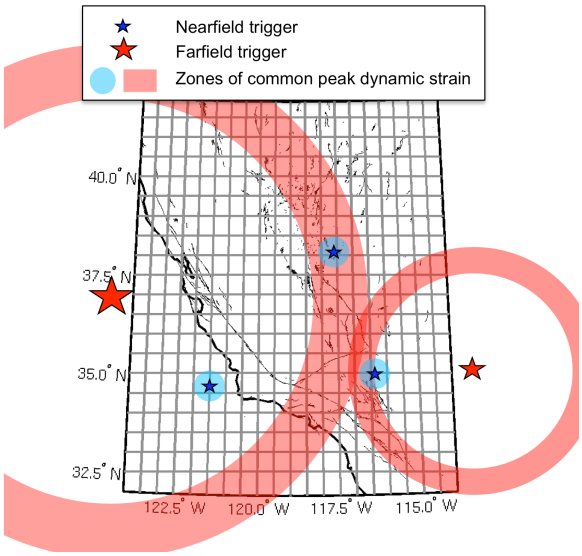

Figure 1-4. Cartoon illustrating the construction of earthquake populations for analysis with the interevent time method. For the long-range case (red), various combinations of magnitude and distance are combined to create populations of earthquakes bracketing potential triggers of common dynamic strain amplitude at the site of the triggered quakes. The study area is gridded, and the interevent time ratio R is calculated in each bin for each trigger. Zones of common dynamic strain form arcs within the study zone. For the short-range case (blue), populations are constructed by combining all earthquakes within some small radius of potential triggers of common magnitude. Spatial grid is not to scale.

The higher the number of bins, the higher the number of bracketing pairs for each trigger quake, down to a lower size limit where single earthquakes begin to be isolated. A bin size of $0.1^{\circ} \times 0.1^{\circ}$ gives the maximum number of bracketing pairs for the whole catalog of potential triggers, but we perform the analysis using several different bin sizes to ensure robustness of the results with respect to parameter choices (Section 1-6.3).

To measure the time ratio R for nearfield triggering, we search for the first earthquake before and after a potential trigger in a disk centered on the trigger earthquake

epicenter. The radius of the disk is set to give the same area as in the farfield bins, e.g. for a farfield bin of 0.1° × 0.1° we define the nearfield radius as ~6.2 km. The time ratios R are then associated with the mean peak dynamic strain over the area of the disk. Assuming radial symmetry (i.e. approximating the trigger as a point source) and using Equations 1-4 and 1-5, the average peak dynamic strain in the nearfield disk is

$$\bar{\varepsilon} = \frac{\overline{PGV}}{C_S} = \frac{1}{C_S \pi D^2} \int_0^D PGV(r) 2\pi r \, dr \,, \qquad (1\text{-}7)$$

where C_S is shear wave velocity, PGV(r) is given by Equation 1-5, and D is the radius of the disk.

We estimate the uncertainty in nearfield peak dynamic strain by bootstrap resampling the Shakemap data directly, refitting the regression formula, and recalculating the mean peak strain according to Equation 1-7. This is preferable to using the uncertainties in the regression constants themselves, because it accounts for strong correlations between the regression parameters. We resample 1000 times and report 95% confidence levels.

1-3.3 Earthquake catalogs

Using the interevent time method on earthquake populations requires large catalogs for both potential trigger earthquakes and for local seismicity. The trigger catalog is drawn from the global ANSS catalog from 1984 through April 2008. We choose the ANSS catalog because it includes both global earthquakes and local California

earthquakes in a self-consistent catalog. More specialized regional or global catalogs may contain more carefully determined moment magnitudes and refined earthquake locations, but given the order of magnitude nature of our strain estimates, the small potential increase in accuracy is not worth the sacrifice in consistency.

For the global catalog, a depth cutoff is imposed at 100 km, because deep earthquakes do not generate significant surface waves. Only earthquakes with surface wave amplitude greater than ten micrometers displacement are treated as potential triggers. This minimum corresponds to a M_S4.5 earthquake at 800 km. We find that this cutoff is sufficiently small to resolve an observational threshold for long-range triggering.

Potential nearfield triggers are drawn from the ANSS catalog for the California and Japan study regions. Other regional catalogs have considerably smaller location errors than the ANSS catalog, but contain considerably fewer earthquakes. However, location error should not be a significant source of error for this study, because the required spatial precision is on the order of the spatial bin size. We therefore choose the catalog with the largest number of earthquakes. The interevent time method should not be sensitive to regional variations in completeness magnitude, because the incompleteness should affect the pre and post-trigger catalogs in a consistent way. However, we impose a magnitude threshold of 2.1, based on the roll-off in the Gutenberg Richter distribution for the catalog as a whole, to protect against large swings in completeness level with time. An upper magnitude cutoff is imposed to

prevent the rupture length from exceeding the radius of aftershock collection. For a spatial bin size of $0.1^{\circ} \times 0.1^{\circ}$, this corresponds to roughly magnitude 5.5. The study area extends from 114° to 124° west, and from 32° to 42° north.

We also look at the scaling of triggering intensity with dynamic strain in Japan. Here we use the JMA catalog from 1997 through March 2006. For consistency with California, we limit the catalog of local events to shallower than 15 km within the land area of the four main islands of Japan. The magnitude of completeness for the JMA catalog of shallow crustal earthquakes may be below 2.1, but we impose this larger magnitude cutoff for consistent comparison with California.

1-3.4. Practicalities of implementation

In order to evaluate the significance of $\overline{R}$ as an indicator of triggering, we require confidence bounds on $\overline{R}$. We use the bootstrap method to generate confidence bounds by randomly resampling the *R* distribution for a given population to generate a suite of estimates of $\overline{R}$ [*Casella and Berger*, 2002]. The confidence bounds on triggering intensity *n* are then calculated by applying the transformation (Equation 1-2) to the bounds computed for $\overline{R}$.

We also take into consideration two potential sources of undesirable bias for realistic sets of earthquakes: (1) the superposition of Omori's law on measurements made in aftershock sequences and (2) the finiteness of the earthquake catalog. The reader

should note that understanding these practicalities is important for implementing the interevent time method, but not crucial for understanding the results presented in subsequent sections.

The superposition of Omori's Law on the measurements is a significant issue for local triggering, but not farfield, and thus could affect the two populations differently. Consider the three earthquakes shown in Figure 1-1. The metric R is designed to measure whether or not earthquake B affects the timing of earthquake C. However, for the nearfield case, it is possible that earthquakes B and/or C are aftershocks of earthquake A. In this case, the times t_1 and t_2 are not uncorrelated. An Omori rate decay ($\sim t^{-1}$) is instead superimposed on the timing of both the trigger quake (quake B) and the subsequent quake. Measuring R in an aftershock sequence, where seismicity rates are decreasing, can spuriously associate the trigger with a seismicity rate decrease. On the other hand, the farfield population is not subject to this effect, as it is very unlikely that a distant earthquake B is an aftershock of a local earthquake A.

Since the Omori's Law bias only affects the nearfield population of quakes, it could interfere with the comparison of triggering intensity between the populations. This bias is suppressed by requiring that any event treated as a trigger (earthquake B) must be larger than the preceding local event (earthquake A). The condition ensures that the rate increase due to the trigger is much larger than any Omori-law rate decrease associated with the prior quake. A higher magnitude difference better ensures against

bias, at the cost of reducing the number of eligible trigger quakes. We find that $\bar{R}$ is stable for a magnitude difference of at least one unit. One magnitude unit corresponds to a roughly tenfold increase in total triggering power [*Reasenberg and Jones*, 1989], and Omori's law ensures that the difference is in general much greater than this, because the influence of the previous earthquake decays rapidly with time.

The second potential source of bias is related to the finiteness of the catalog. This is especially problematic in regions where seismicity rates are low. To understand this effect, consider an ideal catalog with no triggering and uniformly distributed earthquake interevent times. Now consider a distant earthquake with a time near the beginning of the catalog as a potential trigger. Since there is no triggering in this hypothetical catalog, the times to the first earthquake before and after (t_1 and t_2) should be distributed identically, taking values between 0 and infinity, and $\bar{R}$ should be 0.5. However, for a finite catalog, larger values of t_1 and t_2 are missing, because they fall outside the bounds of the catalog. For our hypothetical trigger near the beginning of the catalog, we can only measure R when t_1 happens to be small enough to appear in the catalog, while t_2 can take much larger values and still make it into the catalog. This sampling bias causes $\bar{R}$ to differ from 0.5. The bias is unique for each spatial bin, as it depends on the particular combination of trigger times and the average seismicity rate in the bin.

We compute this bias stochastically by determining $\bar{R}$ for 1000 simulated catalogs in which local earthquake occurrence times are replaced by uniformly distributed random times. The calculated bias is subtracted from the values of $\bar{R}$ measured for the actual catalog. This means that, in effect, $\bar{R}$ is reported relative to a simulated control case with zero triggering. For simplicity, the bias-corrected mean is referred to below as $\bar{R}$.

Correcting for the finite catalog bias somewhat reduces the apparent triggering for the farfield triggers, but does not significantly alter the nearfield data, presumably because nearfield triggers tend to be located in regions with very high seismicity rates. The selection criteria for avoiding the Omori's law bias is only applied to the nearfield triggers. We demonstrate that these bias corrections are adequate by applying the interevent time method to a simulated earthquake catalog in Section 1-5. First, however, we show the results for the real seismicity catalogs.

1-4. Observed triggering intensity as a function of dynamic strain

1-4.1 Proof of concept: Denali

We begin attacking real data by measuring the interevent times for a well-known case of pervasive triggering in order to establish that $\bar{R}$ and n behave as designed. The 2002 magnitude 7.9 Denali earthquake generated peak dynamic strains on the order of $2\text{-}3\times10^{-7}$ for the California study area, according to the empirical regressions, and is known to have triggered significant seismicity [*Gomberg et al*., 2004; *Prejean et*

al., 2004]. For this initial case study, we disregard dynamic strain amplitude variations and define a population consisting of the full gridded study area. The resulting *R* distribution reflects significant triggering (Figure 1-5). The sample mean $\bar{R}$ (with 95% confidence limits) is 0.475 (0.461-0.488), corresponding to a fractional rate change *n* of 0.16 (0.08-0.26) according to Equation 1-2. A simple earthquake count in the 24 hours before and after the Denali earthquake indicates a 22% seismicity rate increase in the following 24 hours. These estimates agree within error. We conclude that *R* is capable of capturing triggering in a case with known seismicity rate increases.

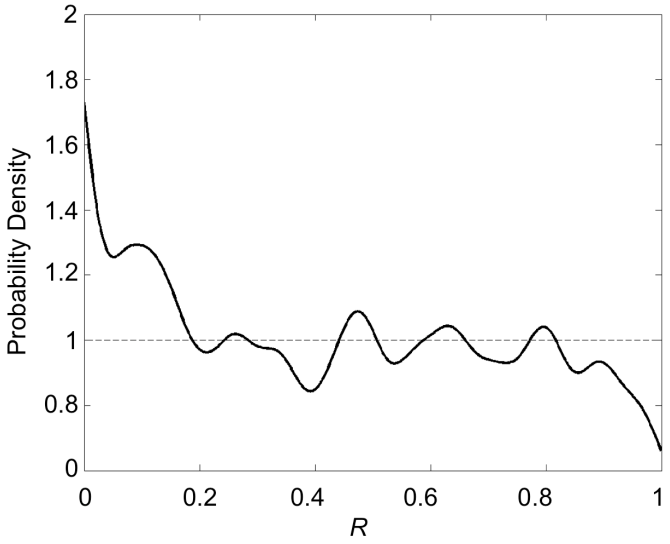

Figure 1-5. Distribution of *R* for the 2002 M7.9 Denali earthquake. Individual *R*-values are computed in 0.1° × 0.1° spatial bins. The high proportion of small *R*-values demonstrates triggering in a large proportion of the bins. The mean of *R* is 0.475. Data are smoothed by a 0.09 unit cosine filter for clarity.

1-4.2 Triggering intensity in the full catalog

The real utility of the method becomes apparent when it is applied to the full ANSS dataset with over 3000 potential farfield triggers, and 12,000 nearfield triggers meeting our criteria. Figure 1-6 shows measured *R* distributions for different dynamic

strain amplitudes, corresponding to various combinations of magnitude and distance for the long-range dataset, and various magnitudes at constant distance for the short-range data. The distributions show evidence of both immediate triggering ($t_2 \sim 0$), in the form of large spikes at $R \approx 0$, and protracted or delayed triggering ($0 < t_2 < t_1$), in the form of a gradual decrease in probability density with increasing R. The distributions show larger proportions of small R for higher dynamic strain amplitudes, as expected.

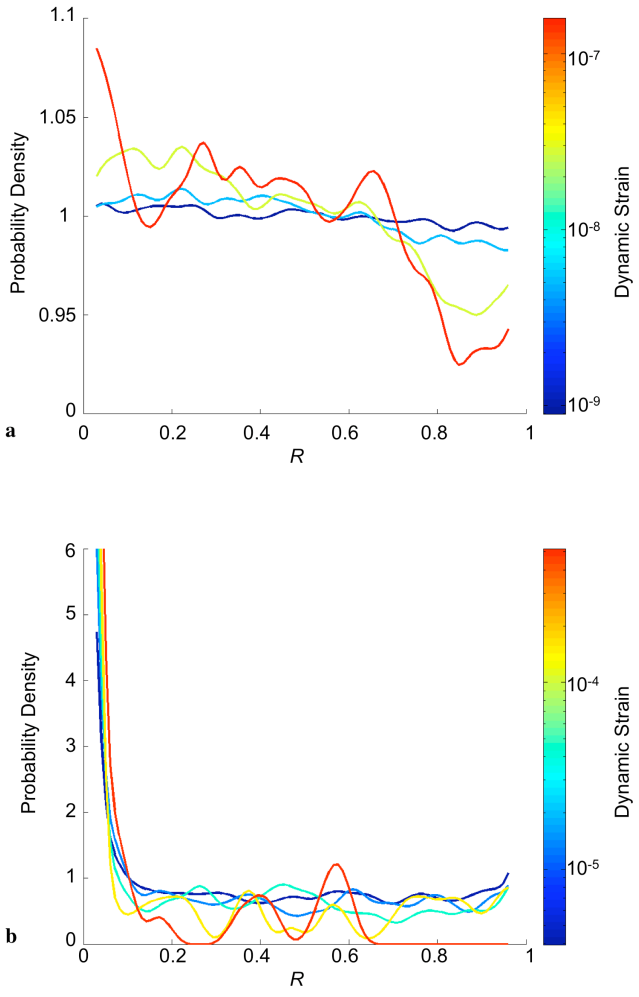

Figure 1-6. Empirical probability densities (distributions) for R. **(a)** Long - range California data (trigger distance > 800 km) for four dynamic strain increments. **(b)** Short-range data, for magnitudes 3.1 to 5.1 in five increments. Curves have been smoothed for clarity using a cosine weighted running average with a window width of 0.09 units. The oscillations at this wavelength are therefore a spurious effect of the smoothing. Curves are truncated at the limits to avoid plotting edge effects of the smoothing.

To assess whether the intensity of dynamic triggering in the farfield can account for the observed intensity of triggering in the nearfield, we plot the sample mean $\bar{R}$ and the transformed triggering intensity *n*, calculated from Equation 1-2, as a function of peak dynamic strain for both nearfield and farfield populations (Figure 1-7a,b). To emphasize the scaling of $\bar{R}$ at small strains, Figure 1-7a shows the value $\Delta\bar{R} = 0.5 - \bar{R}$, as in Figure 1-3. Triggering intensity in the farfield scales with the amplitude of peak dynamic strain. Comparing the triggering intensity for the nearfield population to a trendline fit to the farfield data, we find that the farfield (dynamic) triggering relationship can account for roughly half of the nearfield triggering intensity (Figure 1-7d). Although triggering intensity is best interpreted as a qualitative measure of actual rate change, the relative values should be fairly robust. The uncertainty is large, but the hypothesis that both populations of triggered quakes are produced in simple proportion to peak dynamic strain can be rejected at the 95% confidence level. Nevertheless, the farfield triggering relationship accounts for a significant portion of the nearfield aftershocks, accounting for about 60% of earthquakes within ~6 km of a M3.1 nearfield trigger and about 15% within the same distance of a M5.5 trigger.

We can define a dynamic triggering threshold in the farfield as the smallest dynamic strain for which the 95% confidence limits on $\bar{R}$ fall above 0.5. By this definition, the dynamic triggering threshold in California is approximately 3×10^{-9} strain. Note

that this threshold is not dependent on the transformation from $\overline{R}$ to triggering intensity n, because the significance is evaluated through bootstrap resampling of $\overline{R}$ itself. For a crustal shear modulus of 30 GPa, this corresponds to a dynamic stress of 0.1 kPa.

This estimate is several orders of magnitude smaller than previously reported for dynamic triggering [*Brodsky and Prejean*, 2005; *Gomberg and Davis*, 1996; *Gomberg and Johnson*, 2005; *Stark and Davis*, 1996]. We attribute this improvement in sensitivity to the interevent time method, which can detect small rate changes by using large populations. The threshold is discussed in more detail below.

We also apply the interevent time method to Japan, assuming that the nearfield regression determined in California can be applied to shallow crustal earthquakes in Japan at these small distances. In Japan, the dynamic strains from the largest farfield earthquakes are large enough to overlap in amplitude with the smallest of the nearfield triggers. Where the two populations overlap, we again find a small additional nearfield component, though not at the 95% confidence level (Figure 1-7c). Unfortunately, the uncertainty ranges are too large to assess the relative contributions with any confidence.

Figure 1-7 (facing). (a) The mean interevent time ratio $\bar{R}$, in terms of the deviation from the value in the absence of triggering ($\Delta\bar{R} = 0.5 - \bar{R}$). Compare to Figure 1-3. Long-range (>800 km) triggers are in red and short-range triggers (<6 km) are in blue. Vertical and horizontal error bars are 95% confidence limits. The green point corresponds to the Denali earthquake. The red horizontal bar shows the 2σ uncertainty associated with the farfield peak ground motion estimates. **(b)** Triggering intensity n ($\bar{R}$ transformed via Equation 1-2) as a function of peak dynamic strain in California and **(c)** Japan. The black dashed line in panels (a) and (b) shows the weighted least squares fit to the California farfield data, along with 95% confidence levels. The best-fit curve for California is also shown in (c) for comparison with Japan. **(d)** The fraction of nearfield triggered quakes accounted for by the farfield scaling relationship. First and second error bars represent 64% and 95% confidence limits, respectively.

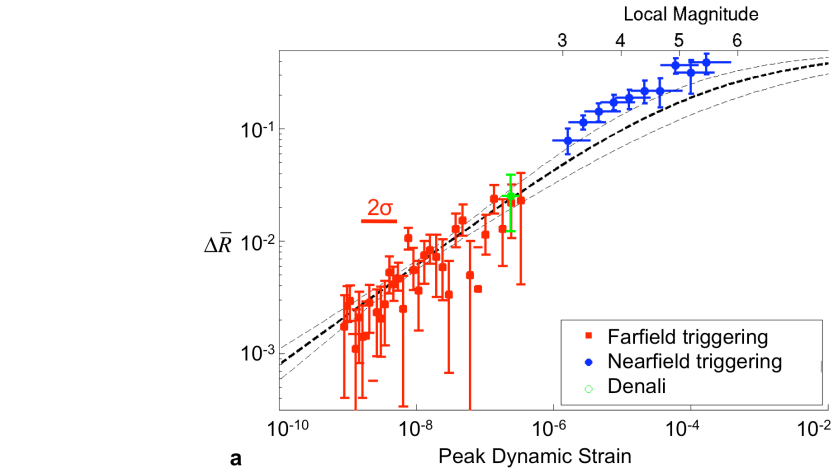
Local Magnitude
3 4 5 6
10^{-1}
$\Delta\bar{R}$ 10^{-2}
10^{-3}
2σ
Farfield triggering
Nearfield triggering
Denali
10^{-10} 10^{-8} 10^{-6} 10^{-4} 10^{-2}
Peak Dynamic Strain

a

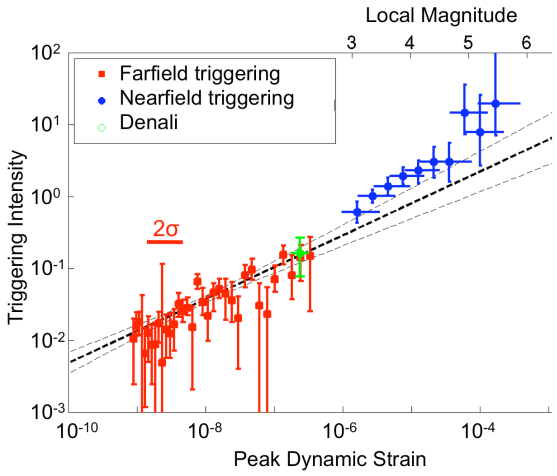
Local Magnitude
3 4 5 6
10^{2} 10^{1} 10^{0} 10^{-1} 10^{-2} 10^{-3}
Triggering Intensity
Farfield triggering
Nearfield triggering
Denali
2σ
10^{-10} 10^{-8} 10^{-6} 10^{-4}
Peak Dynamic Strain

b

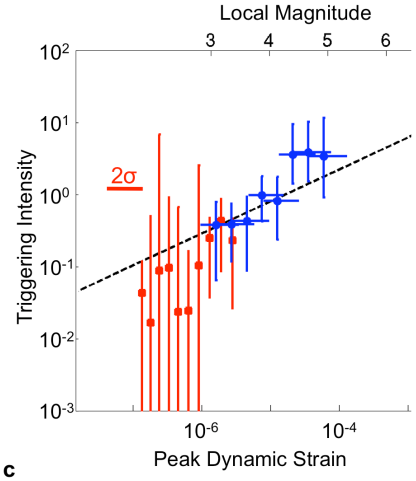
Local Magnitude
3 4 5 6
10^{2} 10^{1} 10^{0} 10^{-1} 10^{-2} 10^{-3}
Triggering Intensity
2σ
10^{-6} 10^{-4}
Peak Dynamic Strain

c

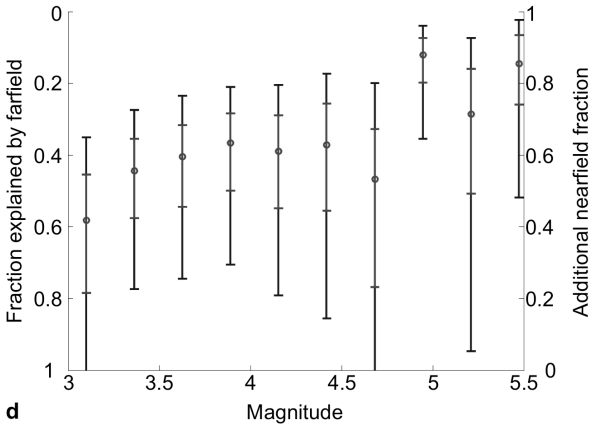
0 0.2 0.4 0.6 0.8 1
Fraction explained by farfield
1 0.8 0.6 0.4 0.2 0
Additional nearfield fraction
3 3.5 4 4.5 5 5.5
Magnitude

d

Triggering intensity in shallow crustal Japan (Figure 1-7c) is reduced relative to California in both the near and farfield populations, with a higher dynamic triggering threshold of 10^{-6} strain. The relative paucity of long-range triggering in Japan has been documented before [*Harrington and Brodsky*, 2006], but this study shows that the reduced triggering susceptibility extends to the nearfield, as well. This difference in triggerability may reflect the difference in tectonic style (compressive vs. transpressive) between the two study areas.

1-4.2 Dynamic strain threshold

The interevent time method resolves triggering at dynamic strains as low as 3×10^{-9}. Many faults are regularly exposed to such small dynamic strain amplitudes without being triggered [*Spudich et al.*, 1995]. The scaling of $\bar{R}$ with dynamic strain may therefore best reflect the *distribution* of fault strengths. The very low triggering intensity at the threshold would then reflect the scarcity of faults so very near failure.

The dynamic strain threshold is also smaller than tidal strain fluctuations [*Cochran et al.*, 2004; *Scholz*, 2003]. This is somewhat puzzling, because tidal strains might be expected to activate all available nucleation sites on a daily basis and set a lower limit for dynamic triggering. Strain tensors associated with crustal earthquakes are likely oriented with more variety than those due to the tides, however, and may access faults that tides are incapable of triggering. In addition, the forcing at the relatively long periods of the tides may be intrinsically different from the dynamic strains imposed at

the short periods of seismic waves [*Beeler and Lockner*, 2003; *Gomberg et al.*, 1997; *Savage and Marone*, 2008].

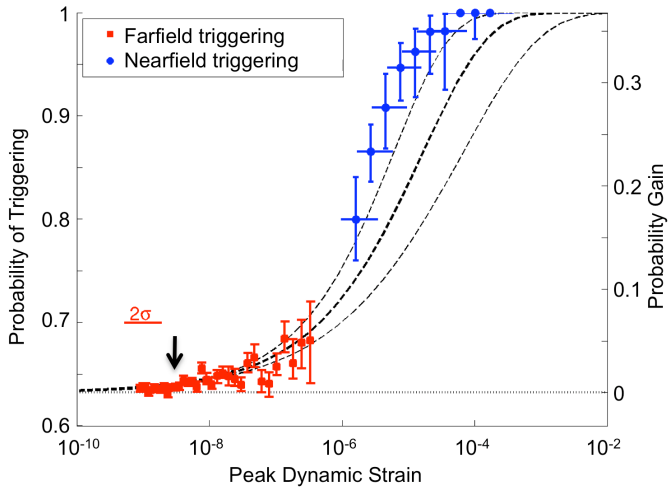

Figure 1-8. Probability of having an earthquake within the pre-trigger recurrence interval (Equation 1-8) as a function of peak dynamic strain, in California. Colors and error bars are as in Figure 1-7. The horizontal dotted line shows the baseline probability of having an earthquake within its own recurrence interval in the absence of triggering (~63%). The black dashed line is the best-fit line from Figure 1-7a,b transformed using Equation 1-8, and shows that the rapid increase in probability is consistent with a smooth increase in triggering intensity. The threshold for dynamic triggering (black arrow) is seen to be an observational threshold, with the probability of observed triggering going smoothly to zero with decreasing dynamic strain.

Evaluating the probability of triggering as a function of dynamic strain (Figure 1-8) aids in the interpretation of the observed triggering threshold. Probability is calculated from the triggering intensity n using the same Poissonian statistical model as before (Appendix 1-C). This is not a new development, as the Poisson model is commonly used to transform an estimate of the number of triggered events into a probability of

earthquake occurrence in a given time period [*Reasenberg and Jones*, 1989]. We discuss the probability of triggering in order to address 1) whether we would expect to resolve triggering below the threshold we have identified, and 2) why previous studies may have failed to identify triggering at the very low levels identified here.

The probability of triggering an earthquake within its own recurrence interval, as a function of n, is given by

$$P\left(N_{EQs} \geq 1\right) = 1 - \exp\left\{-\left(n+1\right)\right\}. \qquad (1\text{-}8)$$

The baseline probability of having an earthquake in the absence of any rate change ($n = 0$) is ~63%. A positive n produces a positive probability gain. Figure 1-8 shows that the probability gain decreases smoothly to zero as n decreases. For the $\sim 3\times10^{-9}$ strain bin in California, there are $\sim 10^5$ interevent time measurements ($\sim 10^3$ triggers $\times$ $\sim 10^2$ bins containing local earthquakes) and this number of events is sufficient to find $\overline{R}$ less than than 0.5 at the 95% confidence level. We estimate (based on an assumed $\sqrt{n}$ scaling of the confidence bounds) that an order of magnitude more observations would be needed to push the observable threshold an order of magnitude lower. This exceeds the size of the earthquake catalog, and we infer that the absence of detected triggering at dynamic strains of less than 3×10^{-9} reflects an observational limit and not necessarily a physical threshold. If triggering occurs at lower dynamic strain amplitudes, we would not expect to resolve it.

Understanding the probability of triggering also helps explain why previous studies have not identified dynamic triggering at the threshold reported here. Previous estimates of the dynamic triggering threshold have been based on waveform inspection, counting statistics, and/or likelihood methods. If triggering intensity $n>1$, the change in seismicity rate is comparable to the background rate, and triggering is easily observable by inspection. Perhaps the conventional division between aftershocks and the more recently discovered farfield triggered populations results from the ease of observing large seismicity increases ($n > 1$) compared to the more subtle farfield triggering ($n < 1$). For a Poisson process, the variance is equal to the average rate, so $n > 1$ also roughly corresponds to the threshold for statistical significance using an earthquake count. Therefore, only the seismicity rate increases corresponding to $n > 1$, i.e. dynamic strains of nearly 10^{-5}, are easily observable by these methods. Likelihood-based methods, in which triggered earthquakes are identified by determining whether the modeled likelihood of their occurrence is otherwise small, cannot resolve triggering where the triggering probability itself is very small. Figure 1-8 shows that the probability of observing a triggered earthquake does not exceed 5% below 10^{-6} dynamic strain. If triggering results in an additional earthquake fewer than 5% of the time, we cannot be 95% confident that the resulting earthquake count did not occur by chance. These considerations may explain why previous studies have not identified dynamic triggering at the level of 3×10^{-9} strain.

1-5. Validation and calibration through statistical seismicity simulations

1-5.1 The effect of triggering cascades on the measured scaling of triggering intensity with strain.

We have shown that triggering intensity scales with dynamic strain in both near and farfield populations, with a moderate additional component in the nearfield. However, there is a problem interpreting the quantitative slope of this trend. Previous work using earthquake counting and carefully declustered seismicity catalogs has shown that the number of local aftershocks following a mainshock of magnitude M goes as $10^{\alpha M}$, with $\alpha \approx 1$ [*Felzer et al*., 2004; *Helmstetter et al*., 2005]. Since dynamic strain scales with magnitude as $\varepsilon \propto 10^{M}$ (Equations 1-5 and 1-6), this implies a linear scaling of aftershock rate with peak dynamic strain. Studies comparing aftershock spatial decay directly to peak ground velocities also find aftershock rates to be consistent with a linear scaling with strain [*Felzer and Brodsky*, 2006; *Gomberg and Felzer*, 2008]. In contrast, this study suggests that triggering intensity varies with dynamic strain roughly as $n \propto \varepsilon^{0.5}$ in both populations (Figure 1-7b). We will now show that this discrepancy arises from the application of a probability model derived for isolated earthquake sequences to a catalog containing superimposed triggering cascades. In essence, the transformation fails to take into account that the interevent times are effectively sampled from two underlying distributions: the distribution of interevent times for triggered earthquakes, and the distribution of times for background or uncorrelated quakes. The observed distribution of R is therefore a superposition of the two distributions illustrated in Figure 1-2. Fortunately, this effect can be quantified and calibrated using statistical simulations.

As described in Section 1-2.2, the sample mean $\bar{R}$ is transformed to triggering intensity n via a probabilistic model for earthquake occurrence times. This transformation is adequate for recovering the qualitative scaling of triggering rate change with dynamic strain amplitude. However, in order to recover absolute rates, we must employ a more sophisticated model that considers the effect of earthquake cascades. The simple transformation from $\bar{R}$ to n implicitly assumed that we correctly associate earthquakes with their respective triggers, but a real catalog contains numerous superimposed triggering cascades. The first earthquake before and after a trigger may or may not then be causally related. If they belong to a different earthquake sequence, they will introduce R-values sampled from a uniform distribution, and the resulting distribution will be some combination of the two curves illustrated in Figure 1-2. This has the effect of dampening the observed triggering signal.

1-5.2 Modeling earthquake cascades: ETAS

To evaluate whether the presence of superimposed earthquake cascades can explain the discrepancy between our recovered slope in Figure 1-7b and previous work based directly on earthquake counts, we generate an artificial earthquake catalog that follows the usually observed statistics of magnitude, timing, and triggering distributions (Appendix 1-D). Because causality is known in the simulation, we can investigate how the use of the first earthquake before and after the trigger affects the

recovered scaling relationship.

A well-established method for generating such a catalog is the epidemic triggered aftershock sequence (ETAS) [*Ogata*, 1992]. ETAS uses well-known empirical statistical seismicity laws as probability distributions to generate stochastic seismicity catalogs. Numerous researchers have used ETAS models to study the complex statistical repercussions of simple earthquake cascades [*Felzer et al*., 2002; *Felzer et al*., 2004; *Hardebeck et al*., 2008; *Helmstetter and Sornette*, 2003; *Holliday et al*., 2008]. Here we use ETAS to study the effects of superimposed earthquake triggering sequences on our transformation of $\bar{R}$ to an estimate of fractional rate change.

We first apply the interevent time method to a zero-dimensional ETAS catalog. The zero dimensional model simulates earthquakes in time only, disregarding spatial distribution, in order to isolate the effect of the earthquake cascade. The triggering law in the simulation corresponds to the case of the nonhomogeneous Poisson process with an Omori decay, and the number of triggered earthquakes scales with $\alpha = 1$. We measure $\bar{R}$ for this simulated catalog using the first earthquake before and after each trigger (unknown causality) and also along individual branches of the triggering cascade (known causality). Both the stepwise homogeneous Poisson and the nonhomogeneous (Omori) model are then used to transform $\bar{R}$ to a triggered rate change.

If interevent times are measured with respect to known branches of the cascade, that is, if the causal relationships are known, the transformation from $\bar{R}$ to n recovers the scaling law that was put into the model (Figure 1-9). If we instead use the first earthquake before and after a putative trigger, a scaling with $\alpha = 0.5$ is recovered, similar to that recovered for the real catalog. This demonstrates that the apparent discrepancy between our scaling and that found in other studies is due to the inclusion of some non-causally related interevent times in the R distribution. The simulation therefore suggests that our interevent time observations are consistent with the number of triggered earthquakes being directly proportional to dynamic strain, as found in previous studies. Consequently, the triggering intensity calculated by our transformation represents a lower bound on the real fractional rate change.

We have claimed that triggering intensity n serves as a good qualitative measure of the scaling with dynamic strain amplitude as long as it scales in a consistent manner with $\bar{R}$. The zero-dimensional simulation shows that n indeed scales consistently, but the zero-dimensional simulation only considered nearfield aftershock triggering, not triggering from distant earthquakes unconnected to the local earthquake cascade. It is possible that the effect of unknown parentage will be different in the near and farfield. Since our conclusions about the relative contribution of dynamic strains in triggering nearfield earthquakes is based on a projection of the farfield relationship, we need to confirm that the two populations are affected identically, despite the imperfect transformation to modeled rate change (i.e. Equation 1-2).

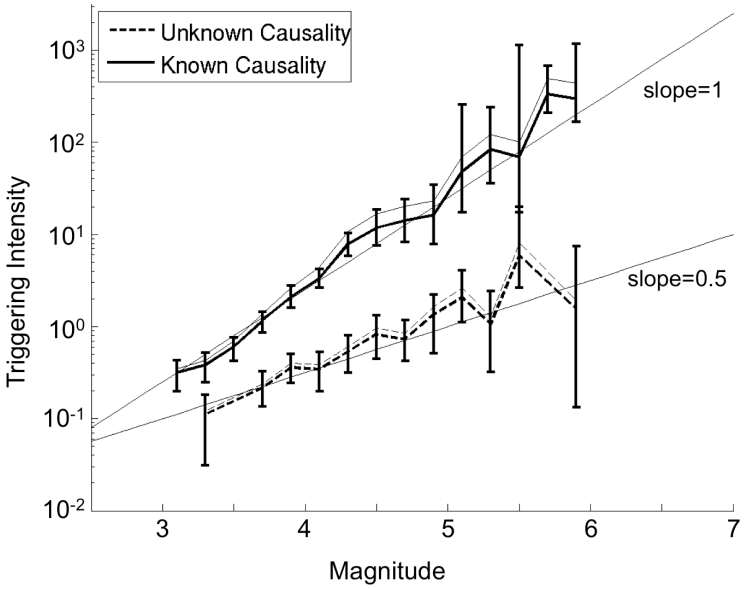

Figure 1-9. Testing the effect of the earthquake cascade on the transformation of $\bar{R}$ to triggering intensity n. A zero-dimensional (time only) ETAS model is used to generate a simulated seismicity catalog in which the triggering law and causal relationships are known. The nonhomogeneous trans-formation, using Omori's law, (thick lines) and the stepwise homogeneous transformation (thin lines) recover similar triggering intensities. If the interevent time ratio R is calculated using the first causally related earthquake before and after the trigger, the transformation recovers the imposed triggering law (solid curves). If the R calculation is not restricted to known causally related earthquakes (as occurs for real catalogs), the method recovers a reduced scaling exponent (dashed curves). Error bars are 95% confidence limits. Reference lines show a slope of 1 (the input relationship) and 0.5.

1-5.3 Space-time ETAS simulation

To verify the robustness of the comparison between populations, we apply the interevent time method to a simulated earthquake catalog in which earthquakes are produced in simple proportion to peak dynamic strain at all distances. If the interevent time method recovers a continuous trend between the simulated near and farfield

populations, we can then interpret the observed offset between the real populations as reflecting an additional nearfield triggering component.

To appropriately represent the two populations defined in this study, we use a full space-time simulated ETAS catalog (Appendix 1-D). We make a key modification to the model, introducing farfield triggering in direct proportion to dynamic strain, as calculated from the empirical ground motion regression in Equation 1-6. We also modify the nearfield triggering rules to reflect the empirical PGV constants in Equation 1-5. This requires very minor adjustments of published ETAS parameters. In order to match the known scaling of aftershock productivity with mainshock magnitude, we set the regression constant $c_2 = 1$. This produces a negligibly larger misfit than the unconstrained PGV regression, and does not significantly change the spatial decay (Table 1-1). This allows us to generate both nearfield aftershock triggering and long-range triggering from distant sources with a consistent triggering rule.

Applying the interevent time method, we recover a continuous trend for a representative set of ETAS parameter taken from the literature (Table 1-2) (Figure 1-10). This verifies that the method is capable of qualitatively measuring triggering in an ideal catalog with triggering proportional to strain. We are therefore justified in interpreting the offset in nearfield and farfield triggering as reflective of an additional nearfield triggering process.

In the previous section, we found that the transformation from $\bar{R}$ to triggering intensity n underestimates the actual productivity scaling α, due to the superposition of triggering cascades. In the space-time ETAS simulations we find that the slope of the trend is also reduced relative to the input value, and varies slightly for different simulation runs, perhaps correlating with the fraction of triggered vs. background earthquakes in a particular realization. The precise relationship between the absolute value of n and the other statistics of the catalog is beyond the scope of this study.

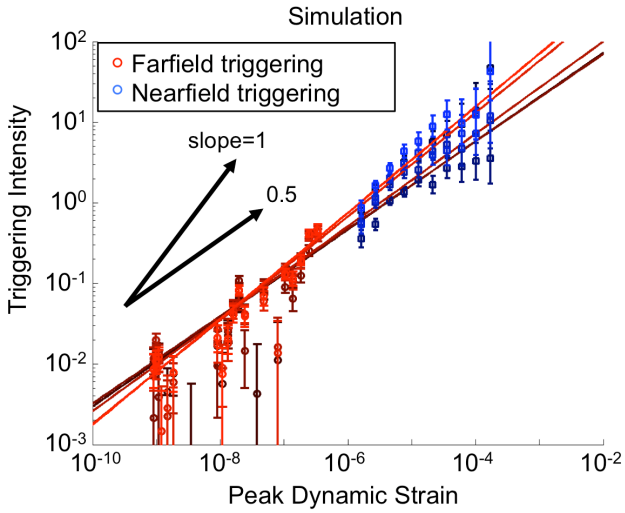

Figure 1-10. Triggering intensity n, determined by the interevent time method, plotted as a function of peak dynamic strain for simulated seismicity catalogs. Triggering is simulated as an identical function of peak dynamic strain in both near (blue hues) and farfield (red hues) populations. Different point brightnesses correspond to different simulation realizations. The recovery of a continuous trend between near and far-field populations validates the method, and demonstrates that the offset in the observed trend (Figure 1-7b) can be confidently interpreted as reflecting an additional nearfield triggering component. Lines of slope = 1 (the input relationship) and slope = 0.5 are plotted to show that the recovered scaling is again reduced relative to the input.

Table 1-2. ETAS Parameters for California

Source	A[a]	c (days)[b]	p[b]	κ (events km^{-2} strain^{-1})[c]
[Hardebeck et al., 2008]	0.008	0.095	1.34	454

[a] Productivity constant, [b] Omori's law parameters, [c] Dynamic triggering productivity (Eq. 1-D7)

1-6. Discussion

1-6.1 Implications for dynamic triggering

Triggering intensity scales with peak dynamic strain in the farfield. Triggering in the farfield (further than 800 km) can be confidently attributed to a dynamic agent, because the triggered earthquakes are well beyond the several source dimensions affected by static and postseismic stresses, and the waiting times to the first triggered earthquakes are much less than the ~10 years required to propagate stresses viscously to these distances, as discussed in the introduction. The empirical proportionality between dynamic strain and triggering intensity can account for a significant portion of triggering in the nearfield, but not all. Additional nearfield triggering may reflect any or all of the following factors: 1) the effect of prolonged static or postseismic strain near the mainshock, 2) a dependence on frequency content, where higher frequency dynamic waves are more effective triggers, or 3) the concentration of potential nucleation sites (e.g. secondary fault strands, damage zones) in the regions very near to mainshocks. If the nearfield triggering component reflects static stress triggering, then this observation suggests that dynamic and static strains produce roughly equivalent numbers of earthquakes in the nearfield of intermediate magnitude

earthquakes. Therefore, both effects must be taken into account to explain aftershock numbers and spatial distributions.

It is important to note that the interevent time measurements do not simply reflect unusual behavior at the beginning of aftershock sequences. In fact, for small nearfield triggers near the magnitude of completeness, the first triggered event is often the only aftershock in the sequence. Furthermore, stacked sequences consisting of only the first aftershocks of small mainshocks follow the same Omori's law decay as single aftershock sequences of large mainshocks [*Felzer et al*., 2004; *Felzer and Brodsky*, 2006]. This implies that there is no physical distinction between the first cataloged aftershock and subsequent aftershocks in a sequence.

How do dynamic strains, which produce no permanent load change, nonetheless account for a significant portion of nearfield triggering? The low threshold for dynamic triggering suggests that arbitrarily small dynamic strains can trigger earthquakes on nucleation sites that are sufficiently near failure. Without a physical threshold for dynamic triggering, the question is one of a balance of timescales – the timescale over which a nucleation site is loaded to failure quasi-statically vs. the time between dynamic strain events large enough to push the fault the rest of the way. If the dynamic trigger recurrence time is smaller than the quasi-static time to failure, the fault will be triggered dynamically. A fault far from failure is unlikely to be triggered by any but the largest dynamic strain events. However, as the fault nears failure, not

only are smaller and smaller dynamic strains required for triggering, but the availability of sufficient triggers increases due to the greater abundance of small earthquakes.

In fact, a simple scaling argument shows that a fault is just as likely to be triggered by a small dynamic strain event as by a large one. The ETAS models show that the data are consistent with the number of dynamically triggered earthquakes being linearly proportional to dynamic strain. The number of earthquakes triggered by an earthquake of magnitude M therefore goes roughly as $\sim 10^{M}$. The Gutenberg-Richter distribution gives that the number of earthquakes with magnitude M goes as $\sim 10^{-M}$. Therefore, the total triggering power for each magnitude bin as a whole is constant:

$$N = N_{Triggers} \times N_{Triggered} = 10^{-M} \cdot 10^{M} = \text{constant} . \qquad (1\text{-}9)$$

Small amplitude triggers and earthquakes with magnitudes below the level of catalog completeness are therefore very important in triggering subsequent earthquakes. Similar arguments for the importance of small earthquakes have been made previously based on statistical considerations [*Felzer et al*., 2004; *Felzer and Brodsky*, 2006; *Helmstetter et al*., 2005; *Sornette and Werner*, 2005a; b].

The low observational threshold and the linear relationship between triggering intensity and dynamic strain amplitude place constraints on the mechanics of triggering. For example, these observations are not consistent with the exponential dependence between stress/strain and the number of triggered earthquakes predicted

by classical rate and state friction [*Brodsky*, 2006; *Dieterich*, 1994; *Gomberg*, 2001]. The simplest way to reproduce the farfield observations may be to invoke a population of nucleation sites with a uniform distribution of dynamic triggering thresholds and a Coulomb-type nucleation criterion.

1-6.2 How delayed earthquakes can be triggered earthquakes

Studies frequently identify only those earthquakes occurring during the passage of seismic waves as dynamically triggered. In applying the interevent time technique, we include arbitrarily delayed 'first' earthquakes after the trigger. This inclusion is based on several considerations.

First, the designation of an earthquake as 'first' is a threshold-dependent, observational distinction. For a lower catalog detection threshold, we should always be able to find an earlier quake. This consideration is especially important for nearfield triggering, where the detection threshold can be temporarily elevated, and a tremendous number of early aftershocks are usually missing from earthquake catalogs [*Kagan*, 2004; *Peng et al*., 2007]. Operationally, it is impossible to distinguish between primary, secondary, and delayed triggered earthquakes, as they share identical space, time, and magnitude statistics [*Brodsky*, 2006; *Felzer et al*., 2004; *Kagan*, 2004]. Regardless, the rates of all of these classifications of earthquakes should be correlated, and secondary or delayed triggered earthquakes should reflect the intensity of the primary triggering process.

Second, we wish to allow for the possibility that dynamic strains can trigger earthquakes by inducing a semi-permanent change in the properties of the fault patch, rather than only through transiently exceeding the fault strength. Several studies have identified or posited long-lasting changes in the mechanical properties or effective stresses within fault zones related to the passage of high-amplitude seismic waves [*Brodsky et al*., 2003; *Elkhoury et al*., 2006; *Johnson and Jia*, 2005; *Parsons*, 2005; *Taira et al*., 2009]. Delayed triggering may then simply reflect the prolonged nature of the triggering process.

Regardless of whether delayed triggering reflects an incompletely observed earthquake cascade or a prolonged physical perturbation of the fault conditions, the inadvertent inclusion of uncorrelated (non-triggered) events will not invalidate the interevent time method, because these interevent times are drawn from a uniform distribution of R values and will not impart a false positive bias.

1-6.3. Robustness of the observations with regard to parameters

The binning of the data and the separation of triggered quakes into farfield and nearfield populations required the introduction of arbitrary parameters. We want to be certain that our conclusions are robust with respect to these parameter choices. The success of the method in recovering a continuous trend for a control case using a simulated catalog with a continuous triggering law is a good confirmation, but we

also check the robustness of the observations with respect to the data selection parameters.

The first arbitrary parameter is the spatial bin size. The results shown in Figure 1-7 and 1-8 use a bin size of 0.1°, because this maximizes the number of *R* values we can calculate. Figure 1-11 confirms that the measurements are not sensitive to the spatial bin size, as long as the number of data points remains high. We show results for bin sizes between ~8 km^2 and 123 km^2 (0.025° - 0.1° on a side). For larger bins, either the reduced quantity of data or the masking of triggered activity by unrelated local aftershocks causes confidence limits to exceed the mean triggering signal.

The distance cutoff for farfield triggers also does not influence the results. Trials using minimum far-field cutoff distances of 800 km through 3200 km all recover essentially the same farfield scaling (Figure 1-12).

Finally, to make sure the long-range triggering signal is not generated entirely by isolated geothermal areas, we plot the contribution of each spatial bin to the total measured triggering intensity, combining all the farfield amplitude bins (Figure 1-13). Geothermal regions (particularly Long Valley and the Salton Trough) contribute strongly, but virtually all regions of active seismicity in California contribute to the long-range triggering signal.

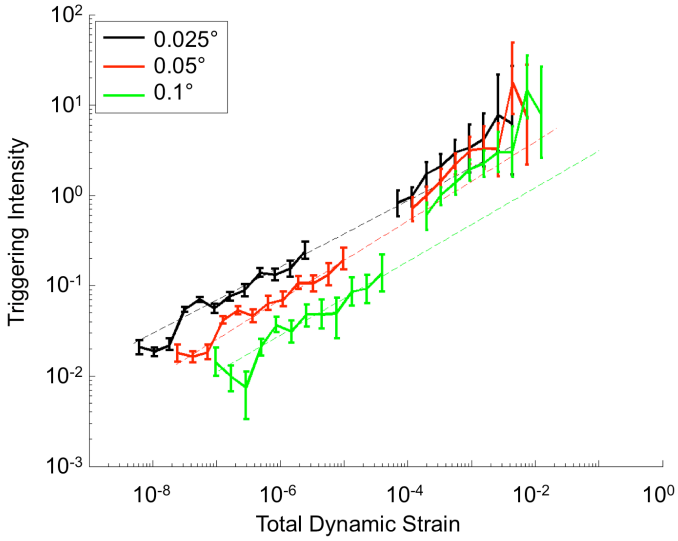

Figure 1-11. Triggering intensity as a function of dynamic strain for different bin sizes. Curves on the left are farfield data; curves on the right are nearfield. The legend gives the farfield spatial bin dimension in degrees for each curve. The nearfield aftershock radius is scaled to cover the same area as the farfield bins. For clarity of presentation, data are plotted against the peak dynamic strain integrated over the bin, rather than the averaged dynamic strain, and are therefore offset. The slopes of the curves and the absolute values of the triggering intensity change slightly with bin size, but the offset between trends is robust.

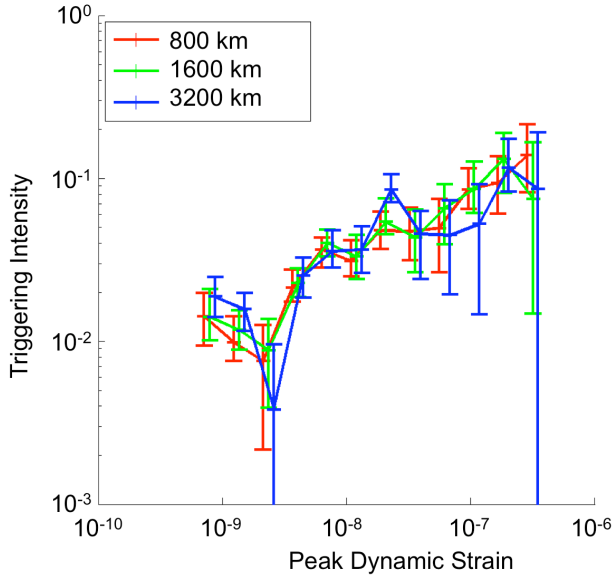

Figure 1-12. Sensitivity to long-range trigger cutoff distance for the California dataset. The legend gives the minimum distance used for potential farfield trigger earthquakes. Results are not sensitive to distance cutoffs above 800 km, although uncertainties grow larger because of the reduced catalog size for larger cutoffs. We do not investigate distance cutoffs below 400 km, because the surface wave magnitude relation (Equation 1-6) is not appropriate for such small distances.

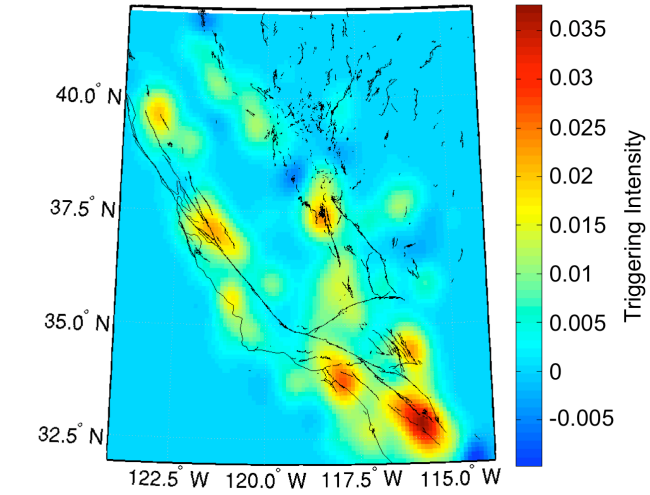

a

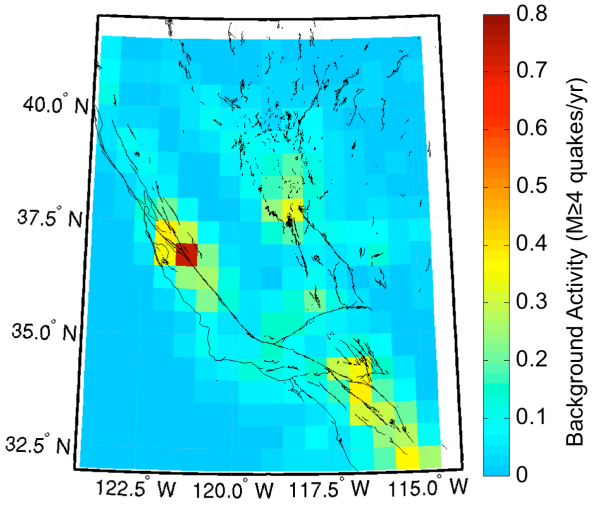

b

Figure 1-13. The geographical distribution of triggering susceptibility in California partially reflects the background activity rate. **a)** Triggering intensity in 0.1° spatial bins for dynamic strains above 10^{-9}. **b)** Background seismicity rate [*Hardebeck et al*., 2008], expressed in terms of the number of magnitude 4 and greater earthquakes per year in each ~0.5° bin. The plots are qualitatively similar, implying that all regions of active seismicity are triggerable, and no single region dominates the triggering signal. Both maps are smoothed by a 0.3° Gaussian kernel.

1-6.4 Relation to previous work

Dividing earthquakes into populations with common strain is a novel way of looking at the scaling of triggering intensity with dynamic strain. Previous work has shown the relevance of dynamic triggering in the nearfield by comparing the falloff in aftershock density away from a mainshock to the falloff of seismic waves at near and intermediate distances [*Felzer and Brodsky*, 2006; *Gomberg and Felzer*, 2008]. These correlations cannot be trivially mapped to a particular function of dynamic strain, however, because the decay in triggering intensity is superimposed on the decay of available nucleation sites away from the mainshock. It is therefore necessary to carefully analyze the statistics of non-triggered (background) seismicity in order to extract the triggering function. The method defined here does not suffer from this ambiguity with respect to a background distribution, because each value of R reflects the seismicity rate change at a single site. We therefore do not need to be concerned about the geometry of the local fault network.

1-7. Conclusion

The observations presented here have the following implications: Farfield triggering scales with peak dynamic strain. This scaling, projected into the nearfield, accounts for 15-60% of earthquakes within 6 km of magnitude 3-5.5 earthquakes. The additional nearfield triggering component may reflect static stress triggering, frequency dependence for dynamic triggering, or concentration of nucleation sites very near mainshocks. Extremely small dynamic strains can trigger faults if they are

sufficiently near failure, down to the observed level of 3×10^{-9} dynamic strain. ETAS simulations in which earthquakes are produced in direct proportion to dynamic strain reproduce the observed scaling of triggering intensity vs. strain, suggesting that dynamic triggering intensity is linearly proportional to peak dynamic strain amplitude. This places a useful constraint on models for earthquake triggering mechanisms.

Appendix 1-A: Expectation of *R* for a Poisson process with a step change in intensity

To find the expectation of the interevent time ratio R as a function of rate change, we first derive the distribution of R using an assumed distribution of interevent times t_1 and t_2, based on a probabilistic model. As discussed in the text, the most widely accepted model for the interevent time distribution is the nonhomogeneous Poisson process. We approximate this model with a stepwise homogeneous process. In a homogeneous Poisson process events occur randomly in time with some average rate λ, known as the intensity. If the intensity λ is independent of time, the interevent times follow an exponential distribution.

$$f(t) = \lambda \exp\{-\lambda t\}. \tag{1-A1}$$

In a non-homogeneous Poisson process, the intensity λ is a function of time, and the interevent times are distributed as

$$f(t) = \lambda(t) \exp\left\{-\int_0^t \lambda(\tau) d\tau\right\}, \tag{1-A2}$$

where $\lambda(t)$ is the intensity at time t. The term within the exponential in both cases is the expected number of events at time t. We define the expected number of events $N(t)$ as

$$N(t) \equiv \int_0^t \lambda(\tau) d\tau \tag{1-A3}$$

for use in subsequent equations.

The joint distribution of two independent interevent times is the product of two exponential distributions.

$$f(t_1,t_2) = \lambda_1(t_1)\lambda_2(t_2)\exp\left\{-N_1(t_1) - N_2(t_2)\right\}, \tag{1-A4}$$

where the subscripts 1 and 2 refer to intensities and times before and after the trigger, respectively.

We derive the joint distribution of R (Equation 1-1) and a dummy variable $T = t_2$, by substituting these variables into Equation 1-A4 and multiplying by the absolute value of the Jacobian of the variable transformation [*Casella and Berger*, 2002; *Walpole and Myers*, 1989]. Expressed in terms of R and T,

$$\begin{aligned} t_1 &= \frac{T}{R} - T, \\ t_2 &= T. \end{aligned} \tag{1-A5}$$

The Jacobian of the transformation can be thought of as describing how areas under the distribution are expanded or contracted through the transformation. It is given by

$$J = \det\begin{pmatrix} \partial t_1/\partial R & \partial t_1/\partial T \\ \partial t_2/\partial R & \partial t_2/\partial T \end{pmatrix} = \det\begin{pmatrix} -\frac{T}{R^2} & \frac{1}{R} - 1 \\ 0 & 1 \end{pmatrix} = -\frac{T}{R^2}. \tag{1-A6}$$

The joint distribution for R and T is then

$$f(R,T) = \lambda_1\left(\frac{T}{R} - T\right)\lambda_2(T)\exp\left\{-N_1\left(\frac{T}{R} - T\right) - N_2(T)\right\}\left|-\frac{T}{R^2}\right|. \tag{1-A7}$$

The marginal distribution of R is obtained by integrating Equation 1-A7 with respect to T.

$$f(R) = \int_0^\infty \lambda_1\left(\frac{T}{R} - T\right)\lambda_2(T)\exp\left\{-N_1\left(\frac{T}{R} - T\right) - N_2(T)\right\}\frac{T}{R^2}dT \ . \qquad \text{(1-A8)}$$

The expectation of R is defined as

$$\langle R\rangle = \int_0^1 R f(R) dR \ . \qquad \text{(1-A9)}$$

Substituting Equation 1-A8 into 1-A9 gives

$$\langle R\rangle = \int_0^1\int_0^\infty \lambda_1\left(\frac{T}{R} - T\right)\lambda_2(T)\exp\left\{-N_1\left(\frac{T}{R} - T\right) - N_2(T)\right\}\frac{T}{R}dT\, dR \ . \qquad \text{(1-A10)}$$

For an otherwise homogenous Poisson process with a step change in intensity λ, the solution to Equation 1-A10 is

$$\langle R\rangle = \frac{\lambda_1\lambda_2}{(\lambda_2 - \lambda_1)^2}\left(\frac{\lambda_1}{\lambda_2} + \ln\left(\frac{\lambda_2}{\lambda_1}\right) - 1\right). \qquad \text{(1-A11)}$$

Let us now define the fractional rate change as the number of triggered earthquakes in some post-trigger time interval normalized by the number that would be expected for the pre-trigger rate:

$$n \equiv \frac{N_2(t) - N_1(t)}{N_1(t)} \ . \qquad \text{(1-A12)}$$

For the step-wise homogeneous Poisson process, where λ_1 and λ_2 are each independent of time, this becomes

$$n = \frac{\lambda_2 - \lambda_1}{\lambda_1}. \tag{1-A13}$$

The expectation of R for the stepwise homogeneous process (Equation 1-A11) can then be rewritten solely as a function of fractional rate change n

$$\langle R \rangle = \frac{1}{n^2}\left[(n+1)\ln(n+1) - n\right]. \tag{1-A14}$$

Equation 1-A14 is Equation 1-2 in the main text with the parameter n identified as triggering intensity. The sample mean $\bar{R}$ is transformed to triggering intensity n by equating $\bar{R}$ with the expectation $\langle R \rangle$ and solving numerically for n.

We can also calculate the expectation of R for the non-homogeneous (Omori-decaying) Poisson process, given an estimate of the parameters in Omori's law. In this case, the post trigger rate is given by

$$\lambda_2(t) = \lambda_1 + \frac{k}{(t+c)^p}. \tag{1-A15}$$

The number of expected events as a function of time is then

$$\begin{aligned} N_2(t) &= \lambda_1 t + \frac{k}{1-p}\left[(t+c)^{1-p} - c^{1-p}\right], && p \neq 1. \\ N_2(t) &= \lambda_1 t + k\ln\left(\frac{t}{c}+1\right), && p = 1. \end{aligned} \tag{1-A16}$$

Substituting these definitions of λ_2 and N_2 into Equation 1-A10, we integrate numerically to find the expectation of R.

The transformation from observed $\bar{R}$ to fractional rate change n with the nonhomogeneous Poisson process is carried out by iteratively solving for the parameter k through Equation 1-A10, and then calculating the fractional rate change n (Equation 1-A12) using Equation 1-A16 for $N_2(t)$. A natural timescale for calculating n is $t = \lambda_1^{-1}$, the expected time to the first event given the pre-trigger rate λ_1. The definition of fractional rate change n for the nonhomogeneous model then reduces to

$$n = \frac{k}{1-p}\left[\left(\lambda_1^{-1} + c\right)^{1-p} - c^{1-p}\right], \qquad p \neq 1$$
$$n = k \ln\left(\frac{1}{c\lambda_1} + 1\right), \qquad p = 1 \tag{1-A17}$$

In this case, we need to estimate a representative background rate, as well as the Omori's law parameters. The fractional rate change recovered using Equation 1-A17 is very similar to that recovered by the stepwise homogeneous transformation, as reflected by Figure 1-3.

Appendix 1-B: Shakemap Peak Ground Velocity regression

We begin with an equation modified from the Next Generation Attenuation study of Campbell and Bozorgnia [2007],

$$\log_{10} \mathrm{PGV} = c_1 + c_2 M - c_3 \log_{10} \sqrt{r^2 + c_4^2}\,, \tag{1-B1}$$

where PGV is peak ground velocity in cm/s, M is earthquake magnitude, r is hypocentral distance in km, and c_i are fit parameters. This is Equation 1-5 in the main

text. This equation differs from Campbell and Bozorgnia [2007] only in the lack of magnitude dependence for the attenuation with distance. We also try a functional form that includes an exponential attenuation term, but find that attenuation is negligible at the small distances studied.

The regression dataset consists of peak velocities from seismic stations within 15 km hypocentral distance from all California earthquakes having an archived Shakemap (http://earthquake.usgs.gov/earthquakes/shakemap). As of Nov. 2009, this constitutes just over 2000 PGV measurements, with 140 within the ~6.2 km range defined as the nearfield in this study. PGV is corrected to hard rock values following the Shakemap methodology, which uses NEHRP site classifications based on shallow shear wave velocity [*Wald et al*., 2006, Section 2.4.3]. Data flagged as outliers during the generation of the Shakemaps are excluded. Since Shakemaps are generated very rapidly after a quake, earthquake magnitudes and locations listed in the Shakemap archive are often preliminary. Earthquake magnitudes and locations are therefore taken from the ANSS catalog for California, which combines locations from both Northern and Southern California seismic networks and is a more authoritative source. To reduce the potential impact of errors in earthquake locations, only data from earthquakes with catalog depths of at least 2 km are considered.

A MATLAB nonlinear optimization algorithm (FMINCON) is used to solve for the constants in Equation 1-B1, with the constraint that constants c_2, c_3, and c_4 be

positive. To make the regression as representative of nearfield measurements as possible, the data are weighted by the space between data points. This is roughly equivalent to fitting the regression curve to binned data. The best-fit regression parameters are given in Table 1-1, row 1. The 95% confidence levels for each parameter are computed from 1000 bootstrap resamplings of the Shakemap data. The regression always finds $c_4 = 0$ km, and therefore we do not report error bounds on this parameter. However, due to the lack of data at very small distances, we must consider this parameter somewhat ill-constrained. The regression and regression misfit are plotted against distance and magnitude in Figure 1-B1, along with several other published regressions for comparison. This regression is the most appropriate proxy for dynamic strain in our magnitude and distance range, as it is conditioned entirely on data within this range.

For use in the ETAS simulation, we also perform a regression in which the magnitude scaling constant c_2 is constrained to equal 1 (Table 1-1, row 2). This is for consistency with known aftershock scaling with magnitude. This constraint does not significantly alter the spatial component of the regression.

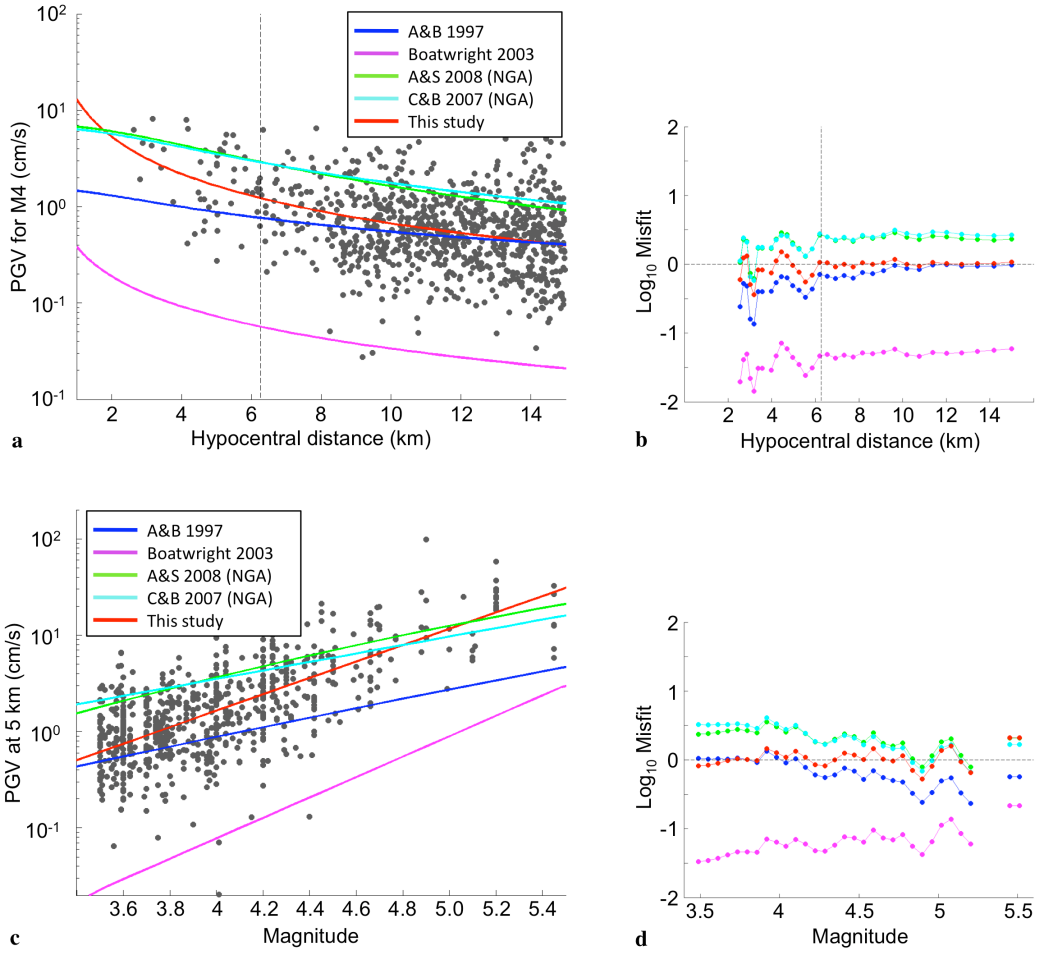

Figure 1-B1. Peak Ground Velocity regression based on California Shakemap data. **(a)** PGV as a function of distance for a M4 reference earthquake, using several published regressions (blue [*Atkinson and Boore*, 1997], magenta [*Boatwright et al.*, 2003], green [*Abrahamson and Silva*, 2008], cyan [*Campbell and Bozorgnia*, 2007]), as well as the regression found in this study (red curve). Grey dots are individual PGV measurements, rescaled to the reference magnitude, using the regression from this study. The vertical dashed line at ~6.2 km marks the boundary of the nearfield region defined in this study. **(b)** Log_{10} misfit (the predicted PGV divided by the observed PGV) for each of the regressions in panel (a) as a function of distance. Misfits are averaged over magnitudes 3.5-5.5. Vertical dashed line as in panel (a). **(c)** PGV as a function of magnitude at a reference distance of 5 km. **(d)** Log_{10} misfit as a function of magnitude for the various regressions, averaged over distances from 0 to 15 km.

Appendix 1-C: Calculation of Earthquake Probability from $\bar{R}$

Appendix 1-A shows how to transform the distribution of *R* into fractional earthquake rate change *n*, assuming Poisson distributed interevent times. The same statistical model can be used to calculate the probability of triggering an earthquake given the estimated rate change. For a homogeneous Poisson process, the probability of observing exactly *m* events in time period *t*, given the average event rate λ, is given by

$$P\left(N_{EQ} = m \mid \lambda t\right) = \frac{\left(\lambda t\right)^m e^{-\lambda t}}{m!} . \qquad \text{(1-C1)}$$

The probability of observing one or more events is equal to one minus the probability of observing zero events.

$$P\left(N_{EQ} > 0 \mid \lambda t\right) = 1 - P\left(N_{EQ} = 0 \mid \lambda t\right) = 1 - \exp\left\{-\lambda t\right\} . \qquad \text{(1-C2)}$$

Over one recurrence interval (time $t = \lambda_1^{-1}$), the probability of observing at least one event given fractional rate change *n* is

$$P\left(N_{EQ} \geq 1 \mid n\right) = 1 - \exp\left\{-\left(n+1\right)\right\} . \qquad \text{(1-C3)}$$

That is, if the average seismicity rate were one earthquake per day, the probability of seeing an earthquake on any given day, in the absence of triggering, is about 63%. Equation 1-C3 then gives the adjusted probability of seeing that "daily" earthquake given the increase in seismicity rate measured by *n*. Equation 1-C3 is Equation 1-8 in the main text.

Appendix 1-D: Modified ETAS simulation

The Epidemic-Type Aftershock Sequence (ETAS) model uses empirical probability distributions to stochastically generate realistically clustered earthquake catalogs [*Ogata*, 1998]. We briefly summarize the governing equations here and direct the interested reader to the studies cited in the main text for more information.

(1) Earthquake magnitudes are assigned from a Gutenberg-Richter probability distribution,

$$N(M) = 10^{a-bM}, \tag{1-D1}$$

where N is the number of earthquakes with magnitude greater than or equal to M, and a and b are constants, with b typically around 1.

(2) The temporal decay of aftershock sequences is governed by the Modified Omori's law, which states that aftershock rate decreases approximately as 1 over the time since the mainshock.

$$R(t) \propto (c+t)^{-p}, \tag{1-D2}$$

where R is the instantaneous aftershock rate, c is a constant that effectively keeps the rate finite at zero time, and p is the decay exponent.

(3) An aftershock productivity law is necessary to close the equations in time and magnitude. Previous work shows that number of aftershocks scales exponentially with mainshock magnitude [*Felzer et al*., 2004; *Helmstetter et al*., 2005].

$$N_{AS} \propto 10^{\alpha M} , \tag{1-D3}$$

where α is a constant near 1 and M is mainshock magnitude. Equations 1-D2 and 1-D3 are related, in that the integral of $R(t)$ over the duration of the aftershock sequence equals N_{AS}, and we define a productivity constant A such that

$$N_{AS} = \int_0^\infty \frac{A \cdot 10^{\alpha(M - M_{\min})}}{(c+t)^p} dt , \tag{1-D4}$$

where M_{min} is the minimum magnitude in the simulation. For $p > 1$, N_{AS} is finite. For $p \leq 1$, N_{AS} must be calculated over a finite time period. Equation 1-D4 is calibrated to reproduce Båth's Law (with α = 1), which states that the largest aftershock of a sequence is on average ~1 magnitude unit below the mainshock magnitude.

(4) A full space-time simulation also requires a law describing the spatial clustering of aftershocks. For example, Felzer and Brodsky [*Felzer and Brodsky*, 2006] give

$$\rho(r) \propto r^{-\gamma} , \tag{1-D5}$$

where ρ is linear aftershock density at distance r from the mainshock, and γ is a constant.

We replace rules (3) and (4) with an equivalent rule that also reproduces Bath's Law and a power-law decrease in linear aftershock density, but is based on dynamic strain rather than magnitude. The equivalent rule specifies that the number of aftershocks per unit area scales linearly with peak dynamic strain.

$$N_{AS} = \kappa \varepsilon_{dyn} . \tag{1-D6}$$

Accordingly, we set $\gamma = c_3$ from the constrained PGV regression (Table 1-1, row 2).

The constant of proportionality κ is found by dividing the number of aftershocks predicted by Equation 1-D4 by the peak dynamic strain integrated over the aftershock zone (Equation 1-7). This gives

$$\kappa = \frac{C_S A \cdot 10^{-c_1 - M_{\min}} c^{1-p} (1-\gamma)}{2\pi (p-1)\left(D_{\max}^{1-\gamma} - D_{\min}^{1-\gamma}\right)}, \tag{1-D7}$$

where C_S is the shear wave speed, c_1 is the first PGV regression parameter (Table 1-1, row 2), A, c, p, are the ETAS constants, and D_{max} and D_{min} are the maximum and minimum bounds of the local aftershock zone, imposed to make the simulation numerically tractable. For the ETAS simulation, we refit the PGV regression constraining $c_2 = 1$, consistent with $\alpha = 1$ in Equation 1-D3. The fit parameters for the constrained regression are reported in Table 1-1, row 2.

Remotely triggered earthquakes are generated in proportion to κ times their dynamic strain amplitude. In this way, triggering associated with both local earthquakes and

the surface waves of distant earthquakes is simulated simultaneously in a self-consistent manner.

We use a version of Felzer and Felzer's Matlab code, modified to include a separate catalog of global triggers (pasadena.wr.usgs.gov/office/kfelzer/AftSimulator.html) [*Felzer et al*., 2002]. This code was also used by Hardebeck et al., [2008]. An estimate of the spatially varying California background seismicity rate is included with the code (Figure 1-13b), as well as estimates of ETAS parameters representative of California (Table 1-2). The dimensions of the aftershock zone, specified for computational efficiency and to keep the number of aftershocks finite, are left at the default values of $D_{min} = 0.001$ km and $D_{max} = 500$ km, respectively.

References

Abrahamson, N., and W. Silva (2008), Summary of the Abrahamson and Silva NGA ground-motion relations, *Earthquake Spectra*, *24*(1), 67-97.

Aki, K., and P. G. Richards (2002), *Quantitative seismology*, 2nd ed., xviii, 700 pp., University Science Books, Sausalito, Calif.

Anderson, J. G., J. N. Brune, J. N. Louie, Y. H. Zeng, M. Savage, G. Yu, Q. B. Chen, and D. Depolo (1994), Seismicity in the Western Great Basin apparently triggered by the Landers, California, Earthquake, 28 June 1992, *Bulletin of the Seismological Society of America*, *84*(3), 863-891.

Atkinson, G. M., and D. M. Boore (1997), Some comparisons between recent ground motion relations, *Seismological Research Letters*, *68*(1), 24-40.

Beeler, N. M., and D. A. Lockner (2003), Why earthquakes correlate weakly with the solid Earth tides: Effects of periodic stress on the rate and probability of earthquake occurrence, *Journal of Geophysical Research-Solid Earth*, *108*(B8), doi:10.1029/2001jb001518.

Boatwright, J., K. Thywissen, and L. C. Seekins (2001), Correlation of ground motion and intensity for the 17 January 1994 Northridge, California, Earthquake, *Bulletin of the Seismological Society of America*, *91*(4), 739-752.

Boatwright, J., H. Bundock, J. Luetgert, L. Seekins, L. Gee, and P. Lombard (2003), The dependence of PGA and PGV on distance and magnitude inferred from northern California ShakeMap data, *Bulletin of the Seismological Society of America*, *93*(5), 2043-2055.

Brodsky, E. E., V. Karakostas, and H. Kanamori (2000), A new observation of dynamically triggered regional seismicity: Earthquakes in Greece following the August, 1999 Izmit, Turkey earthquake, *Geophysical Research Letters*, *27*(17), 2741-2744.

Brodsky, E. E., E. Roeloffs, D. Woodcock, I. Gall, and M. Manga (2003), A mechanism for sustained groundwater pressure changes induced by distant earthquakes, *Journal of Geophysical Research-Solid Earth*, *108*(B8), doi:10.1029/2002jb002321.

Brodsky, E. E., and S. G. Prejean (2005), New constraints on mechanisms of remotely triggered seismicity at Long Valley Caldera, *Journal of Geophysical Research*, *110*(B4), doi:10.1029/2004jb003211.

Brodsky, E. E. (2006), Long-range triggered earthquakes that continue after the wave

train passes, *Geophysical Research Letters*, *33*(15), L15313, Doi:15310.11029/12006gl026605.

Campbell, K. W., and Y. Bozorgnia (2007), Campbell-Bozorgnia NGA ground motion relations for the geometric mean horizontal homponent of peak and spectral ground motion parameters, Report 2007/02, Pac. Earthquake Eng. Res. Cent., Berkeley, Calif.

Casella, G., and R. L. Berger (2002), *Statistical inference*, 2nd ed., xxviii, 660 pp., Thomson Learning, Australia ; Pacific Grove, CA.

Cochran, E. S., J. E. Vidale, and S. Tanaka (2004), Earth tides can trigger shallow thrust fault earthquakes, *Science*, *306*(5699), 1164-1166.

Corral, A. (2004), Long-term clustering, scaling, and universality in the temporal occurrence of earthquakes, *Physical Review Letters*, *92*(10), Doi 10.1103/Physrevlett.1192.108501.

Dieterich, J. (1994), A Constitutive Law for Rate of Earthquake Production and Its Application to Earthquake Clustering, *Journal of Geophysical Research-Solid Earth*, *99*(B2), 2601-2618.

Elkhoury, J. E., E. E. Brodsky, and D. C. Agnew (2006), Seismic waves increase permeability, *Nature*, *441*(7097), 1135-1138.

Felzer, K. R., T. W. Becker, R. E. Abercrombie, G. Ekstrom, and J. R. Rice (2002), Triggering of the 1999 M-W 7.1 Hector Mine earthquake by aftershocks of the 1992 M-W 7.3 Landers earthquake, *Journal of Geophysical Research*, *107*(B9), doi:10.1029/2001jb000911.

Felzer, K. R., R. E. Abercrombie, and G. Ekstrom (2004), A common origin for aftershocks, foreshocks, and multiplets, *Bulletin of the Seismological Society of America*, *94*(1), 88-98.

Felzer, K. R., and E. E. Brodsky (2005), Testing the stress shadow hypothesis, *Journal of Geophysical Research*, *110*(B5), B05S09.

Felzer, K. R., and E. E. Brodsky (2006), Decay of aftershock density with distance indicates triggering by dynamic stress, *Nature*, *441*(7094), 735-738.

Freed, A. M., and J. Lin (1998), Time-dependent changes in failure stress following thrust earthquakes, *Journal of Geophysical Research-Solid Earth*, *103*(B10), 24393-24409.

Freed, A. M. (2005), Earthquake triggering by static, dynamic, and postseismic stress transfer, *Annual Review of Earth and Planetary Sciences*, *33*, 335-367.

Gardner, J. K., and L. Knopoff (1974), Sequence of Earthquakes in Southern-California, with Aftershocks Removed, Poissonian, *Bulletin of the Seismological Society of America*, *64*(15), 1363-1367.

Gasperini, P., and B. Lolli (2006), Correlation between the parameters of the aftershock rate equation: Implications for the forecasting of future sequences, *Physics of the Earth and Planetary Interiors*, *156*(1-2), 41-58.

Gomberg, J., and D. Agnew (1996), The accuracy of seismic estimates of dynamic strains: An evaluation using strainmeter and seismometer data from Pinon Flat Observatory, California, *Bulletin of the Seismological Society of America*, *86*(1), 212-220.

Gomberg, J., and S. Davis (1996), Stress strain changes and triggered seismicity at The Geysers, California, *Journal of Geophysical Research*, *101*(B1), 733-749.

Gomberg, J., M. L. Blanpied, and N. M. Beeler (1997), Transient triggering of near and distant earthquakes, *Bulletin of the Seismological Society of America*, *87*(2), 294-309.

Gomberg, J. (2001), The failure of earthquake failure models, *Journal of Geophysical Research-Solid Earth*, *106*(B8), 16253-16263.

Gomberg, J., P. A. Reasenberg, P. Bodin, and R. A. Harris (2001), Earthquake triggering by seismic waves following the Landers and Hector Mine earthquakes, *Nature*, *411*(6836), 462-466.

Gomberg, J., P. Bodin, and P. A. Reasenberg (2003), Observing Earthquakes Triggered in the Near Field by Dynamic Deformations, *Bulletin of the Seismological Society of America*, *93*(1), 118-138.

Gomberg, J., P. Bodin, K. Larson, and H. Dragert (2004), Earthquake nucleation by transient deformations caused by the M=7.9 Denali, Alaska, earthquake, *Nature*, *427*(6975), 621-624.

Gomberg, J., and P. Johnson (2005), Seismology - Dynamic triggering of earthquakes, *Nature*, *437*(7060), 830-830.

Gomberg, J., and K. Felzer (2008), A model of earthquake triggering probabilities and application to dynamic deformations constrained by ground motion observations, *Journal of Geophysical Research-Solid Earth*, *113*(B10), B10317, doi:10310.11029/12007jb005184.

Hainzl, S., F. Scherbaum, and C. Beauval (2006), Estimating background activity based on interevent-time distribution, *Bulletin of the Seismological Society of America*, *96*(1), 313-320.

Hardebeck, J. L., K. R. Felzer, and A. J. Michael (2008), Improved tests reveal that the accelerating moment release hypothesis is statistically insignificant, *Journal of Geophysical Research*, *113*(B8), B08310, doi:08310.01029/02007jb005410.

Harrington, R. M., and E. E. Brodsky (2006), The absence of remotely triggered seismicity in Japan, *Bulletin of the Seismological Society of America*, *96*(3), 871-878.

Helmstetter, A., and D. Sornette (2003), Predictability in the epidemic-type aftershock sequence model of interacting triggered seismicity, *Journal of Geophysical Research*, *108*(B10), doi:10.1029/2003jb002485.

Helmstetter, A., Y. Y. Kagan, and D. D. Jackson (2005), Importance of small earthquakes for stress transfers and earthquake triggering, *Journal of Geophysical Research*, *110*(B5), B05S08.

Hill, D. P., P. A. Reasenberg, A. Michael, W. J. Arabaz, G. Beroza, D. Brumbaugh, J. N. Brune, R. Castro, S. Davis, D. Depolo, W. L. Ellsworth, J. Gomberg, S. Harmsen, L. House, S. M. Jackson, M. J. S. Johnston, L. Jones, R. Keller, S. Malone, L. Munguia, S. Nava, J. C. Pechmann, A. Sanford, R. W. Simpson, R. B. Smith, M. Stark, M. Stickney, A. Vidal, S. Walter, V. Wong, and J. Zollweg (1993), Seismicity remotely triggered by the magnitude 7.3 Landers, California, Earthquake, *Science*, *260*(5114), 1617-1623.

Hill, D. P., and S. G. Prejean (2007), *Dynamic Triggering*, Treatise on Geophysics, Ed. H. Kanamori, Elsevier.

Hill, D. P. (2008), Dynamic stresses, Coulomb failure, and remote triggering, *Bulletin of the Seismological Society of America*, *98*(1), 66-92.

Holliday, J. R., D. L. Turcotte, and J. B. Rundle (2008), A review of earthquake statistics: Fault and seismicity-based models, ETAS and BASS, *Pure and Applied Geophysics*, *165*(6), 1003-1024.

Hough, S. E. (2005), Remotely triggered earthquakes following why California is moderate mainshocks (or, why California is not falling into the ocean), *Seismological Research Letters*, *76*(1), 58-66.

Johnson, P. A., and X. Jia (2005), Nonlinear dynamics, granular media and dynamic earthquake triggering, *Nature*, *437*(7060), 871-874.

Joyner, W. B., and D. M. Boore (1981), Peak Horizontal Acceleration and Velocity from Strong-Motion Records Including Records from the 1979 Imperial-Valley, California, Earthquake, *Bulletin of the Seismological Society of America*, *71*(6), 2011-2038.

Kagan, Y. Y., and D. D. Jackson (2000), Probabilistic forecasting of earthquakes, *Geophysical Journal International*, *143*(2), 438-453.

Kagan, Y. Y. (2004), Short-term properties of earthquake catalogs and models of earthquake source, *Bulletin of the Seismological Society of America*, *94*(4), 1207-1228.

Kilb, D., J. Gomberg, and P. Bodin (2000), Triggering of earthquake aftershocks by dynamic stresses, *Nature*, *408*(6812), 570-574.

King, G. C. P., R. S. Stein, and J. Lin (1994), Static Stress Changes and the Triggering of Earthquakes, *Bulletin of the Seismological Society of America*, *84*(3), 935-953.

Lay, T., and T. C. Wallace (1995), *Modern Global Seismology*, Academic Press, San Diego.

Love, A. E. H. (1927), *Mathematical Theory of Elasticity*, Cambridge Univ., Cambridge, UK.

Marsan, D. (2003), Triggering of seismicity at short timescales following Californian earthquakes, *Journal of Geophysical Research-Solid Earth*, *108*(B5), Doi 10.1029/2002jb001946.

Matthews, M. V., and P. A. Reasenberg (1988), Statistical methods for investigating quiescence and other temporal seismicity patterns, *Pure and Applied Geophysics*, *126*(2-4), 357-372.

Molchan, G. (2006), Interevent time distribution in seismicity: A theoretical approach by (vol 162, pg 1135, 2005), *Pure and Applied Geophysics*, *163*(7), 1453-1455.

Ogata, Y. (1992), Detection of precursory relative quiescence before great earthquakes through a statistical-model, *Journal of Geophysical Research*, *97*(B13), 19845-19871.

Ogata, Y. (1998), Space-time point-process models for earthquake occurrences, *Ann. Inst. Stat. Math.*, *50*(2), 379-402.

Ogata, Y. (1999), Seismicity analysis through point-process modeling: A review, *Pure and Applied Geophysics*, *155*(2-4), 471-507.

Parsons, T. (2005), A hypothesis for delayed dynamic earthquake triggering, *Geophysical Research Letters*, *32*(4), L04302, doi:04310.01029/02004gl021811.

Peng, Z., J. E. Vidale, M. Ishii, and A. Helmstetter (2007), Seismicity rate immediately before and after main shock rupture from high-frequency waveforms in Japan, *J. Geophys. Res.*, *112*(B03306)

Peng, Z. G., and P. Zhao (2009), Migration of early aftershocks following the 2004 Parkfield earthquake, *Nature Geoscience*, *2*(12), 877-881.

Perfettini, H., and J. P. Avouac (2007), Modeling afterslip and aftershocks following the 1992 Landers earthquake, *Journal of Geophysical Research-Solid Earth*, *112*(B7), Doi 10.1029/2006jb004399.

Pollitz, F. F., R. Burgmann, and B. Romanowicz (1998), Viscosity of oceanic asthenosphere inferred from remote triggering of earthquakes, *Science*, *280*(5367), 1245-1249.

Pollitz, F. F., and M. J. S. Johnston (2006), Direct test of static stress versus dynamic stress triggering of aftershocks, *Geophysical Research Letters*, *33*(15), L15318 Artn l15318.

Prejean, S. G., D. P. Hill, E. E. Brodsky, S. E. Hough, M. J. S. Johnston, S. D. Malone, D. H. Oppenheimer, A. M. Pitt, and K. B. Richards-Dinger (2004), Remotely triggered seismicity on the United States west coast following the M-W 7.9 Denali fault earthquake, *Bulletin of the Seismological Society of America*, *94*(6), S348-S359.

Reasenberg, P. A., and L. M. Jones (1989), Earthquake hazard after a mainshock in California, *Science*, *243*(4895), 1173-1176.

Rezapour, M., and R. G. Pearce (1998), Bias in surface-wave magnitude M-s due to inadequate distance corrections, *Bulletin of the Seismological Society of America*, *88*(1), 43-61.

Richter, C. F. (1935), An instrumental earthquake magnitude scale, *Bulletin of the Seismological Society of America*, *25*(1), 1-32.

Saichev, A., and D. Sornette (2006), "Universal" distribution of interearthquake times explained, *Physical Review Letters*, *97*(7), Doi 10.1103/Physrevlett.1197.078501.

Savage, H. M., and C. Marone (2008), Potential for earthquake triggering from transient deformations, *Journal of Geophysical Research-Solid Earth*, *113*(B5), B05302, doi 05310.01029/02007jb005277.

Scholz, C. H. (2003), Earthquakes - Good tidings, *Nature*, *425*(6959), 670-671.

Sornette, D., and M. J. Werner (2005a), Apparent clustering and apparent background earthquakes biased by undetected seismicity, *Journal of Geophysical Research-Solid Earth*, *110*(B9), Doi 10.1029/2005jb003621.

Sornette, D., and M. J. Werner (2005b), Constraints on the size of the smallest triggering earthquake from the epidemic-type aftershock sequence model, Bath's law, and observed aftershock sequences, *Journal of Geophysical Research-Solid Earth*, *110*(B8), B08304, doi:08310.01029/02004jb003535.

Spudich, P., L. K. Steck, M. Hellweg, J. B. Fletcher, and L. M. Baker (1995), Transient Stresses at Parkfield, California, Produced by the M-7.4 Landers Earthquake of June 28, 1992 - Observations from the Upsar Dense Seismograph Array, *Journal of Geophysical Research-Solid Earth*, *100*(B1), 675-690.

Stark, M. A., and S. D. Davis (1996), Remotely triggered microearthquakes at The Geysers geothermal field, California, *Geophysical Research Letters*, *23*(9), 945-948.

Stein, R. S., G. C. P. King, and J. Lin (1994), Stress triggering of the 1994 M=6.7 Northridge, California, earthquake by Its predecessors, *Science*, *265*(5177), 1432-1435.

Taira, T., P. G. Silver, F. L. Niu, and R. M. Nadeau (2009), Remote triggering of fault-strength changes on the San Andreas fault at Parkfield, *Nature*, *461*(7264), 636-U677.

Velasco, A. A., S. Hernandez, T. Parsons, and K. Pankow (2008), Global ubiquity of dynamic earthquake triggering, *Nature Geoscience*, *1*(6), 375-379.

Wald, D. J., V. Quitoriano, T. H. Heaton, H. Kanamori, C. W. Scrivner, and C. B. Worden (1999), TriNet "ShakeMaps": rapid generation of peak ground motion and intensity maps in California, *Earthquake Spectra*, *15*, 537-556.

Wald, D. J., B. C. Worden, V. Quitoriano, and K. L. Pankow (2006), Shakemap manual: technical manual, user's guide, and software guide, Version 1.0, http://pubs.usgs.gov/tm/2005/12A01/

Walpole, R. E., and R. H. Myers (1989), *Probability and Statistics for Engineers and Scientists*, 4th ed., Macmillan Publishing Compant, New York.

West, M., J. J. Sanchez, and S. R. McNutt (2005), Periodically triggered seismicity at Mount Wrangell, Alaska, after the Sumatra earthquake, *Science*, *308*(5725), 1144-1146.

Wiemer, S. (2000), Introducing probabilistic aftershock hazard mapping, *Geophysical Research Letters*, *27*(20), 3405-3408.

Yamanaka, Y., and K. Shimazaki (1990), Scaling relationship between the number of aftershocks and the size of the main shock, *J. Phys. Earth*, *38*, 305-324.

Ziv, A. (2003), Foreshocks, aftershocks, and remote triggering in quasi-static fault models, *Journal of Geophysical Research-Solid Earth*, *108*(B10), Doi 10.1029/2002jb002318.

Chapter 2. Precursory remote triggering is absent near the epicenters of impending great earthquakes

Nicholas J. van der Elst, Emily E. Brodsky, and Thorne Lay

Dept. of Earth and Planet. Sci., University of California, Santa Cruz

Abstract: Recently, there have been numerous great ($M_W \geq 8$), devastating earthquakes, with a rate in the last 7 years that is 260% of the average rate over the 111-year seismological history. Each great earthquake presents an opportunity to study a major fault at the very end and very beginning of the inferred seismic cycle. In this work, we use these events as both targets and sources to probe susceptibility to dynamic triggering in the epicentral region before and after a large earthquake. This study also carefully addresses the possibility that large earthquakes interact in a cascade of remotely triggered sequences that culminate in further large earthquakes. We seek evidence of triggering associated with the 16 great $M_W \geq 8$ events that occurred between 1998 and 2011, using regional and global earthquake catalogs, to measure changes in inter-event time statistics. Statistical significance is calculated with respect to a non-stationary reference model that includes mainshock-aftershock clustering. In only a few cases do we detect triggering near the epicenters of $M \geq 8$ earthquakes separated by more than 10º. The number of detections is not significant, given the number of detection attempts. Systematic triggered rate changes are less than 15% at 95% confidence, and thus cannot account for the large increase in $M_W \geq 8$ earthquake rate. The catalogs are insufficiently complete to resolve more moderate

triggering expected from previous studies. We calculate that an improvement in completeness magnitude from 3.7 to 3.5 could resolve the expected triggering signal in the ISC catalog taken as a whole, but an improvement to M 2.0 would be needed to consistently resolve triggering on a regional basis.

2-1. Introduction

The last seven years have experienced a surge in great ($M \geq 8$) earthquakes relative to the preceding 4 decades [*Ammon et al*., 2010]. Between the M_W 9 Sumatra earthquake of December 2004 and the M_W 9 Tohoku-Oki earthquake of March 2011, Earth has averaged 1.7 great earthquakes per year, which is 260% of the rate of 0.66 per year over the entire seismological record extending back to 1900 (i.e. a rate increase of 160%). This interval of heightened great earthquake occurrence has prompted many to consider whether the global increase could represent long-range interactions between great earthquakes [*Brodsky*, 2009; *Michael*, 2011; *Shearer and Stark*, 2011]; can the occurrence of one great earthquake increase the likelihood of a subsequent quake in a self-exciting process? This certainly seems to be the case for some of the nearby $M \geq 8$ earthquakes. Examples include the 2005 and 2007 Sumatra earthquakes that followed the 2004 Sumatra earthquake, rupturing portions of the plate boundary to the southeast immediately adjacent to and 700 km away from the first event [*Nalbant et al*., 2005; *Wiseman and Burgmann*, 2011], as well as the 2006 - 2007 Kuril doublet. However, even after these instances are removed, there remains a surfeit of global great earthquakes – 1.14 per year, almost double the century-long

average rate. Could very large magnitude earthquakes have an extended reach, beyond that for conventionally accepted aftershocks, such that they can trigger earthquake cascades at great distance on 1-10 year timescales?

The peak dynamic strains associated with the surface waves of great M ≥ 8 earthquakes exceed 10^{-6} at global distances, and such strains are commonly observed to triggered small earthquakes [*Gomberg and Johnson*, 2005; *Hill and Prejean*, 2007; *Lei et al*., 2011; *van der Elst and Brodsky*, 2010; *Velasco et al*., 2008]. Indeed, there are reports of triggering of remote activity for many of the recent great events. Examples include triggering in China by the 2003 Tokachi-Oki and 2004 Sumatra earthquakes [*Lei et al*., 2011; *Wu et al*., 2011], triggering in Alaska and the continental US by the 2004 Sumatra earthquake [*Rubinstein et al*., 2011; *West et al*., 2005], triggering in California by the 2010 Maule-Chile earthquake [*Peng et al*., 2010], and triggering throughout the United States by the 2011 Tohoku-Oki earthquake [*Rubinstein et al*., 2011]). Dynamic triggering of remote events is no longer controversial. However, earthquakes larger than about M 5 have not yet been observed to be dynamically triggered during passage of great event surface waves [*Parsons and Velasco*, 2011]. Nevertheless, statistical aftershock models predict that sequences of smaller events may occasionally culminate in delayed events that are larger than the initial events [*Felzer et al*., 2002; *Felzer et al*., 2004]. A good example of this process is the M 5.6 Little Skull Mountain earthquake, which occurred 280 km distant and 22.3 hours after the 1992 Landers earthquake, but was preceded by a

sequence of small events initiated within the coda of the Landers main shock [*Anderson et al*., 1994].

This motivates considering the possibility of a global earthquake cascade, which we test in this study. The model is as follows: large earthquakes radiate powerful surface waves that dynamically trigger small events at global distances. These remotely triggered aftershocks trigger their own aftershocks, and so on. Occasionally, secondary aftershocks are larger than their main shock, ramping up the local seismicity rate. This process continues, and may eventually culminate in another great earthquake, at which point the global cycle is renewed. Any particular remotely triggered aftershock sequence is very unlikely to produce an aftershock larger than the initially triggered events, let alone a $M \geq 8$ quake, but if enough small remotely triggered aftershock sequences are initiated globally, the cumulative probability of a few sequences producing big events over several years may be large.

A remotely triggered rate increase of 160% may be considered extreme even for the largest of the recent great earthquakes, except if located in highly susceptible regions. At the core of the cascade hypothesis is therefore a fundamental physical question about whether the dynamic triggerability of a fault zone reflects the accumulation of stress on the fault. Since transient stresses generated by seismic waves are much smaller than the total strength of a fault or the stress drop in an earthquake [*Gomberg et al*., 2004], seismic waves must act as the "straw that breaks the camel's back,"

pushing an already critically stressed fault over the edge to failure. This expectation is guided by laboratory experiments designed to simulate dynamic triggering on stick-slip faults [*Beeler and Lockner*, 2003; *Savage and Marone*, 2008] and by numerical studies of theoretical earthquake nucleation models [*Gomberg*, 2001]. These results imply that when and where triggered earthquakes are observed, we may be able to infer the presence of critically stressed faults. It is not known, however, whether the rupture zone as a whole is critically stressed before a great earthquake, that is, whether an earthquake knows in advance how big it is going to get. Susceptibility to dynamic triggering may therefore serve as a probe of the state of stress before (and after) a great earthquake.

Here we consider the seismic catalog of the last 13 years, using the cascade model to guide the search for distant triggering. If the recent great earthquakes are part of a global self-exciting cascade, the rate of small earthquakes at the site of some or all impending great earthquakes should have increased at the time of some previous large earthquake(s). We therefore search systematically for triggered rate changes localized near the epicenters of subsequent great earthquakes at the time of earlier great earthquakes in the sequence. We look for triggering by all of the $M \geq 8$ earthquakes identified in the PAGER catalog since 1998, using two global earthquake location catalogs (PDE and ISC), and one regional catalog (JMA (see Data and Resources). We measure rate changes using the inter-event time ratio method [*Felzer and*

Brodsky, 2005; *van der Elst and Brodsky*, 2010], and evaluate the significance of any detected rate changes with respect to a Poisson process on a region-by-region basis.

2-1.1 Previous statistical studies on global earthquake rate change

Some studies have looked at whether recent earthquake rates on a global scale are consistent with a stationary, uniform Poisson process [*Michael*, 2011; *Shearer and Stark*, 2011]. These two studies examined the statistical distribution of $M \geq 7$ earthquake inter-event times over the past century using a global seismicity catalog, and found that the observed clustering of great earthquakes is not significantly non-Poissonian, aside from regional clustering (as expected for proximate aftershocks).

Here we briefly illustrate this approach and summarize the conclusions. In the PAGER catalog, which is a compilation of large historical earthquakes that emphasizes consistent magnitude determination, 77 $M_W \geq 8$ earthquakes have been recorded in the 111 years since 1900. Twelve of these earthquakes occurred between December 2004 and the present. Three of these twelve are considered regional aftershocks of other great earthquakes (the 2005 and 2007 Sumatra quakes, and the 2007 Kuril quake), leaving 9 independent events in 7 years since December 2004. The binomial probability of finding 9 of 74 uniformly distributed events in such a 7-year time window is 4.3%. This number would likely decrease further if we also declustered the long-term catalog. However, when we consider the probability of finding some unusual clustering in a long duration catalog, the clustering is not

particularly unusual. That is, although the recent cluster of earthquakes has low probability of occurrence for any single 7 year period, finding clustering in one such period out of 111 years is not unexpected [*Shearer and Stark*, 2011].

On the other hand, inability to falsify the uniform Poisson hypothesis is not proof of constant uniform rate. By convention, scientific hypothesis testing is conservative, and we are usually more concerned with minimizing the probability that the null hypothesis is falsely rejected (Type I error), than falsely accepted (Type II error), and it is preferable to use the simplest model possible as the null hypothesis. However, in considerations that have major societal implications, as in the case of global earthquake clustering, it is important to quantitatively address both types of error, that is, to quantitatively assess our confidence that the rate has *not* increased.

Addressing the potential for type II error is equivalent to asking: what is the maximum rate change that could still pass the Poissonian hypothesis test at 95% confidence? That is, what are the confidence bounds on the rate change given the limitations of the catalog? Given N observed earthquakes, the 95% confidence bound on the Poissonian rate parameter λ is just the highest value of λ that would produce N or fewer events at least 5% of the time.

To briefly illustrate this concept, we break down the earthquake record into periods between 1900 and Dec. 2004, and after Dec. 2004 (a prominent change point). This is

only an illustration of the concept, and does not constitute a test of the uniform Poissonian hypothesis. We do not consider here the appropriateness of the change point, nor do we decluster the pre-2004 catalog. The (undeclustered) intensity in the first period is λ_0 = 0.62 events/yr. With 9 (declustered) events in the subsequent 7 years, we can be 95% confidence that the rate in the second period is greater than 0.67 and less than 2.24 events/yr. The corresponding rate change $\delta\lambda \equiv \Delta\lambda/\lambda_0$ is 8% – 261%, which covers the naïve observation of an apparent rate increase of 160%. These large confidence bounds indicate that the test has very little power to reject the Poisson hypothesis in such a small time window. We cannot statistically rule out a large rate increase, any more than we can rule out uniformity in rate. Thus, purely statistical treatments of the overall earthquake history are not likely to resolve the question of long-range interactions. More direct examination in the context of a physically motivated framework may provide firmer conclusions.

This paper is organized as follows: First, we introduce the inter-event time statistic and define the quantities to be measured. We then describe the spatial and temporal windowing of the catalogs. Before applying the statistic to the real catalog, we calculate the expected rate change at each site, given previously established scaling laws for remote triggering, so that we can interpret the incidence of non-detections. We then proceed to measure actual triggered rate changes near the epicenters of great earthquakes, both before and after they occur, calculating significance with respect to a homogeneous Poisson process. We find no precursory triggering before impending

great earthquakes that could explain the global increase in rate. We do find an apparent triggering signal in the wake of great earthquakes, but we show that this apparent post-seismic triggering signal is a consequence of the over-simplified uniform Poisson reference model. We then develop a non-stationary reference model that accounts for mainshock-aftershock clustering, and show that this removes the apparent triggering signal in the post-seismic target regions. Finally, we use the information gathered at each target site to assess how much improvement would need to be made to the global seismic network in order to detect remote triggering at the sites of major subduction zone earthquakes on a consistent basis.

2-2. Method

2-2.1 Inter-event time ratios

To capture rate changes in the impending rupture zones of great earthquakes, we take the sample mean of the inter-event time ratio r, calculated in regional spatial bins, defined by

$$r = \frac{t_2}{t_1 + t_2}, \qquad (2\text{-}1)$$

where t_1 and t_2 are the intervals to the first local earthquake before (t_1) and after (t_2) some reference time – in this case, the time of a distant great earthquake. If the regional earthquake times are uncorrelated with the time of the distant great earthquake, r is uniformly distributed between [0,1]. If the timing of regional earthquakes is advanced by the occurrence of the distant great earthquake (i.e., if

there is a remotely triggered earthquake or one of its aftershocks in the local bin), t_2 will be on average smaller than t_1, and the distribution of r will be shifted toward smaller values.

Each great earthquake target zone is divided into a uniform grid, and r-values are calculated from pairs of earthquakes within each grid square. The target zones are defined by the first 10 days of aftershocks of each great earthquake, extending no further than 1° from the main shock epicenter. The spatial constraint focuses attention on the plausible nucleation regions for the great events. The grid spacing within this region is optimized to give the maximum number of unique pairs of earthquakes in a region. (Only one value of r can be calculated for each grid square, so the number of unique pairs increases with the grid fineness, up to the point where bins begin to lack earthquake pairs straddling the trigger events.) This optimization is done for each trigger-region pair.

The population of r-values for each target zone is averaged, giving a mean r (denoted $\bar{r}$), and this mean is compared to the expected mean for a reference model (e.g. uniform Poisson process, Appendix 2-A). The triggering detection confidence is defined as $c = 1 - p_r$, where p_r is the significance, i.e. the probability that a random process would produce a mean as small or smaller than the observed $\bar{r}$, by chance. Note that using this one-sided definition, the triggering confidence equals 50% for zero rate change, and a triggering confidence near zero means that an apparent rate

decrease is present. However, this definition keeps us from assigning negative confidence to values of $\bar{r} < 0.5$.

We also calculate a fractional rate change $\delta\lambda$ consistent with the observed $\bar{r}$, assuming that the earthquake rate is constant and Poissonian, but with a step-change in rate at the time of the trigger (Appendix 2-A). The fractional rate change $\delta\lambda$ is defined as the difference in rates, normalized by the initial rate. We also compute the upper and lower 95% confidence bounds on $\delta\lambda$, which depend on both $\bar{r}$ and the sample size (Appendix 2-A). The upper and lower bounds can be thought of as the highest and lowest rate changes that could still pass a Poissonian hypothesis test. These three values: lower bound, best estimate, and upper bound, are denoted $\delta\lambda_{05}$, $\delta\lambda_{50}$, and $\delta\lambda_{95}$, respectively.

2-2.2 Triggers and target regions and time windows

The trigger and target regions consist of all M ≥8 earthquakes since the M_W 8.1 Balleny Islands earthquake of 1998 (Table 2-1 and Figure 2-1). Earthquake magnitudes are taken from the PAGER catalog, and all correspond to M_W values from centroid moment tensor inversions.

Table 2-1: List of great earthquakes

	Date	Name	M_W	T (days) [a]
1	25-03-1998	Balleny Is.	8.1	83
2	16-11-2000	New Ireland	8.0	220
3	23-06-2001	Peru	8.4	220
4	25-09-2003	Tokachi-Oki	8.3	455
5	23-12-2004	Macquarie Is.	8.1	95
6	26-12-2004	Sumatra-Andaman	9.0	93
7	28-03-2005	Sumatra-Nias	8.6	93
8	03-05-2006	Tonga	8.0	196
9	15-11-2006	Kuril Is.	8.3	59
10	13-01-2007	Kuril Is.	8.1	59
11	01-04-2007	Solomon Is.	8.1	78
12	15-07-2007	Central Peru	8.0	27
13	12-09-2007	So. Sumatra	8.5	27
14	29-09-2009	Samoa	8.0	151
15	27-02-2010	Chile	8.8	151
16	11-03-2011	Tohoku-Oki	9.0	92

[a] Maximum allowed t_1 or t_2 in Eq. 2-1 based on the timing of other $M_W \geq 8$ earthquakes. The total trigger time window is $2T$, centered on each great event.

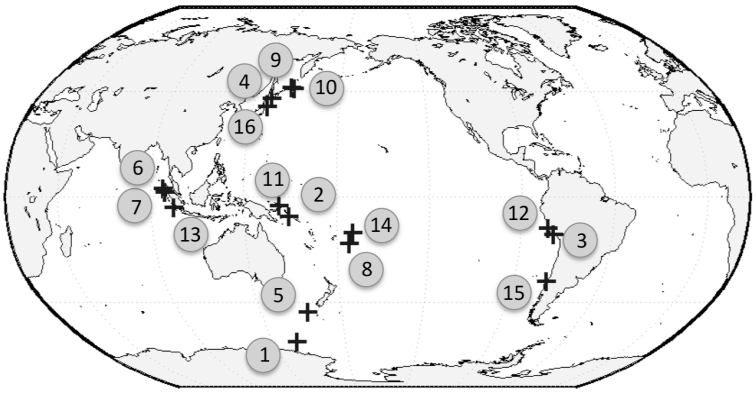

Figure 2-1. Locations of $M_W \geq 8$ great earthquakes used in this study. Crosses mark locations; numbers give the order of occurrence (Table 2-1).

The window for measuring triggering relative to each great event is limited so that triggering windows do not overlap with other trigger times (windows themselves may overlap, but cannot contain more than a single $M_W \geq 8$ trigger event). Allowing more than one trigger in each window could lead to double counting and would allow the impending regional quake itself or its aftershocks to be considered a remotely triggered event. Double counting, or counting the $M_W \geq 8$ earthquakes themselves (which were used to formulate the hypothesis), would invalidate the statistical significance calculations. Each time window is also constrained to be symmetrical around the great event trigger time, as the inter-event time ratio r would be biased if the waiting times t_1 and t_2 were limited to different ranges.

The choice of target time window and target region do not strongly influence the conclusions of this paper. Using smaller time windows has the effect of diminishing the sample size and reducing statistical robustness, but larger time windows have the effect of averaging out any triggered rate increase over the duration of the window. Using a constant, smaller maximum time window of ±59 days, for example, changes the joint statistics by 1-2%, but does not alter any of the conclusions of this study. We choose to use variable-length windows because it maximizes the number of samples overall.

The requirement of non-overlapping windows is a problem for the 2004 Macquarie Islands and 2004 Sumatra-Andaman earthquakes, which are separated by only 2.4 days. This could be taken as a perfect example of one great earthquake being triggered on the heels of a 77° distant earthquake. However, no significant precursory triggering of smaller events due to the Macquarie earthquake is observed in the rupture region of the impending Sumatra quake (there is only one earthquake near Sumatra in the interval between them reported in the ISC catalog). Rather than impose a 2.4-day time limit on both earthquakes, we choose to expand the triggering window to the limits imposed by the previous and next events in the sequence (~95 days rather than 2.4). This means that any triggering by the Sumatra-Andaman quake may be attributed to the Macquarie quake and vice versa. These two triggers are considered as a single event when calculating the joint statistical significance of measured rate changes.

Triggering susceptibility is measured using three target catalogs. We first examine the PDE and ISC global earthquake catalogs. The PDE is a rapidly published compilation of many reporting networks worldwide. It has an overall completeness level of roughly $M_C = 4.1$ and is complete up to the present. (We determine the completeness magnitude as the magnitude above which a linear fit can explain at least 90% of the variance in log-cumulative-number vs. magnitude.) The ISC catalog is the authoritative final catalog combining the best data worldwide. It has a somewhat lower completeness threshold ($M_C = 3.7$), but extends only through 11/2009 at this

time. The PDE catalog is therefore the only source of regional target data for the 2010 Chile, and 2011 Tohoku trigger earthquakes. Where the PDE catalog does overlap with the ISC catalog, it provides a qualitative check on the effect of catalog uncertainties on the measured triggering significance, though we consider the ISC catalog to be authoritative. The ISC includes un-reviewed hypocenter data below magnitude 3.5, and the quality of this data is very non-uniform in time. We therefore restrict the ISC catalog to 'prime' quality events above M 3.5. Finally, the regional JMA catalog is used for target regions near Japan. This catalog has a much lower completeness threshold (M_C = 1.3) in the Tokachi-Oki and Tohoku-Oki target regions.

2-2.3 Binomial and joint significance tests

We compute the significance of $\bar{r}$ for each of the 256 individual trigger-target pairs (16 triggers at 16 target regions), with respect to the reference model (e.g. uniform Poisson process) and report triggered rate change detection successes as instances with greater than 90% triggering confidence. This represents a relatively low significance threshold, designed to capture relatively low rate changes in small samples, and it requires that we always consider the number of detection thresholds expected by chance when interpreting the results for any subgroup of the data. We therefore also compute the joint significance for several subgroups of the data: 1) All 120 trigger-target pairs that come any time before the regional earthquakes, reflecting long-term precursory triggering; 2) The 15 pairs from Group 1 that come immediately

before the regional earthquakes, reflecting short-term precursory triggering; 3) All 120 pairs that come any time after the regional earthquakes; and 4) the 15 pairs from Group 3 that fall immediately after the regional earthquakes. Groups 1 and 2 tell us about any potential earthquake cascade or precursory triggering, and Groups 3 and 4 tell us about changes in triggerability in response to damage induced by a large regional quake.

We compute the combined significance in these subgroups, using the same method as in the case-by-case basis, i.e. as the probability of obtaining a smaller $\bar{r}$ by chance for the entire population (the *p*-value), denoted p_r. However, computing p_r in this way weights the calculation toward the sites with the most earthquakes, and this may dampen the triggering signal from more sparsely covered regions. For this reason, we also compute the significance of the number of detection success within each group, treating each measurement as a Bernoulli trial with probability of success 1 - c_{th}, where c_{th} is the detection confidence threshold. The triggering signal could take several forms: occasional high confidence triggering at a few regions, or a systematic small bias toward slightly positive rate changes. To capture both of these cases, the binomial test is computed for thresholds of 90% and 50%, with *p*-vaues denoted p_{90} and p_{50}. The results of these tests are considered statistically significant if the *p*-values fall below 0.05.

In this paper, we follow the convention that case-by-case triggering measurements will be reported in terms of triggering confidence, and all joint statistics derived from multiple confidence measurements will be reported in terms of significance level p.

2-2.4 Expected rate changes from surface wave strain amplitudes

In order to interpret the incidence of non-detections, we also calculate an expected rate change based on previous regional observations. Van der Elst and Brodsky [2010] calibrated a relationship between the amplitude of triggering waves and the triggered rate change using the interevent time ratio r in California. Fitting a power law to the triggered rate change versus peak surface wave strain ε in that study gives an expected rate change of

$$\delta\lambda_{exp} = 82 \times \varepsilon^{0.43} . \qquad (2\text{-}2)$$

An identical analysis of Japan seismicity found that Japan is ~3 times less triggerable than California. This gives an indication of the variability we should expect in triggering susceptibility worldwide. The triggering sites in this study are also potentially much deeper in this study than in the one used to calibrate Eq. 2-2. We therefore treat Eq. 2-2 only as a rough estimate of expected rate change, and likely an upper bound.

Van der Elst and Brodsky [2010] estimated peak surface wave strain using the empirical surface wave magnitude equation, which relates wave amplitude to earthquake magnitude and distance. For the large magnitude earthquakes we are

considering here, the surface wave magnitude is saturated and the empirical scaling is inadequate. Instead, we measure peak velocities directly at nearby seismic stations (see Data and Resources). Dynamic strain amplitude is estimated as

$$\varepsilon = \frac{v_{\max}}{c_S}, \qquad (2\text{-}3)$$

where c_S = 3.5 km/s is the surface wave phase velocity, and v_{max} is the peak vertical velocity measured on a broadband sensor. Seismic stations are selected within 6 - 10º of the target earthquake epicenter, depending on the density of stations, and the instrument response is removed over a passband of 1 - 50 s. Amplitude at the target earthquake epicenter is extrapolated from the measured values using the distance decay exponent from the surface wave magnitude equation $M_S = \log A + 1.66 \log \Delta + 2$ [*Lay and Wallace*, 1995]. Where multiple records exist, the amplitudes are distance-corrected and averaged. In the 14 out of 256 cases where no amplitude measurements exist within 10º of the epicenter, the trigger amplitude is estimated as the mean of the distance-corrected amplitudes measured at all the other target sites.

The measured peak ground velocities agree well with the empirical surface wave amplitude equation multiplied by $2\pi/T$ (period T = 20 sec) to get velocity, but with somewhat reduced dependence on magnitude, as expected for this magnitude range (Figure 2-2). There is also antipodal focusing of the surface waves beyond 150º distance that is not captured by the empirical surface wave equation.

Using Eqs. 2-2 and 2-3 to transform measured peak velocity into expected rate change, we find a mean expected rate change $\delta\lambda_{exp}$ over all trigger-target pairs on the order of 11% (Figure 2-2). This expectation is for rate change averaged over a large area, and triggered rate change may be much higher locally. Indeed, it must be higher locally if triggering is to account for the observed increase in the rate of large earthquakes.

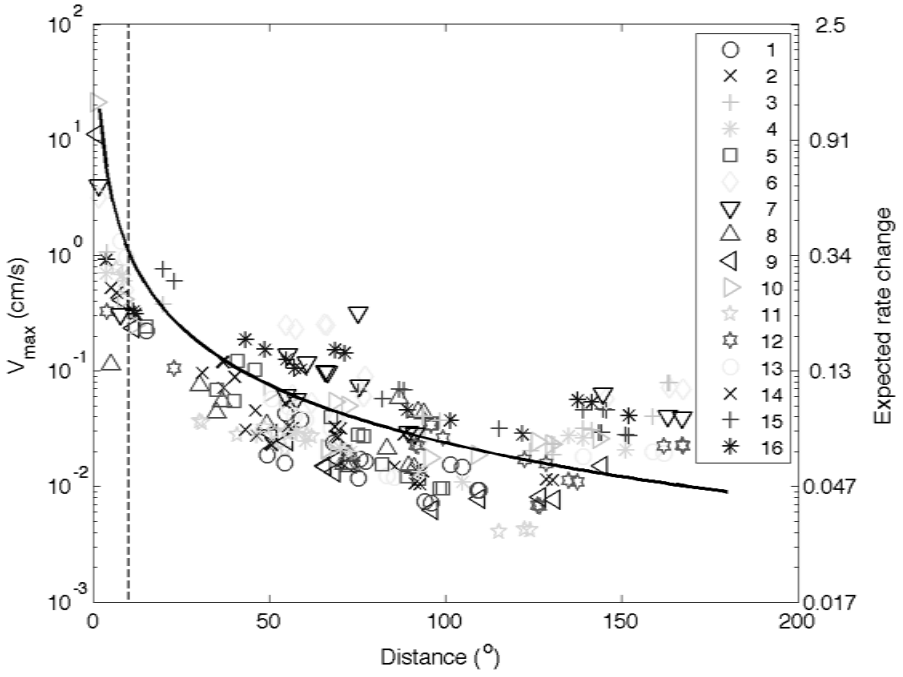

Figure 2-2. Peak surface wave velocity and expected rate change $\delta\lambda_{exp}$ (Eq. 2-2) for each M ≥ 8 earthquake, at each target site. The legend gives the earthquake number from Table 2-1 (e.g. 1: 1998 Balleny Islands, 6: 2004 Sumatra-Andaman, 16: 2011 Tohoku-Oki). The black curve shows the empirical surface wave magnitude equation, multiplied by $2\pi/T$ (period T = 20 sec) to obtain velocity, for a M_S 8.2 earthquake (the median trigger magnitude in this study). The dashed line shows the 10° limit used to define the farfield. The increase in amplitude beyond 150° is due to antipodal focusing

Such small rate changes require large sample sizes to establish high significance (Table 2-2, Appendix 2-A). For example, a sample size of m = 11 is required to establish a 100% rate change (doubling) at 90% confidence. A sample size m = 543 would be required to establish a rate increase of 10%. To establish a 1% rate change at 90% confidence would require m = 49,765. Given the limited completeness of the global seismicity catalog, it may be possible to resolve rate changes of 10-100% on a regional basis, but smaller rate changes (< 10%) will likely go unnoticed.

Table 2-2: Sample size required to detect a triggered rate change

Rate change $\delta\lambda$ [%]	Expected $\bar{r}$	Required sample size m for 90% (95%) confidence
1	0.498	49,765 (81,980)
5	0.492	2,071 (3,411)
10	0.484	543 (895)
67	0.415	20 (32)
100	0.386	11 (18)
160	0.345	6 (10)

2-3. Results

2-3.1 Example target location

As an example, the target region for the Tohoku-Oki earthquake is shown in Figure 2-3, using the JMA catalog, for all 16 of the potential trigger earthquakes (Table 2-1), with triggers 5 and 6 combined. This is the best-instrumented target region out of all 16 targets (M_C = 1.3), and therefore the density of earthquake pairs is very high. Most other sites, using the global earthquake catalogs, are much more poorly sampled.

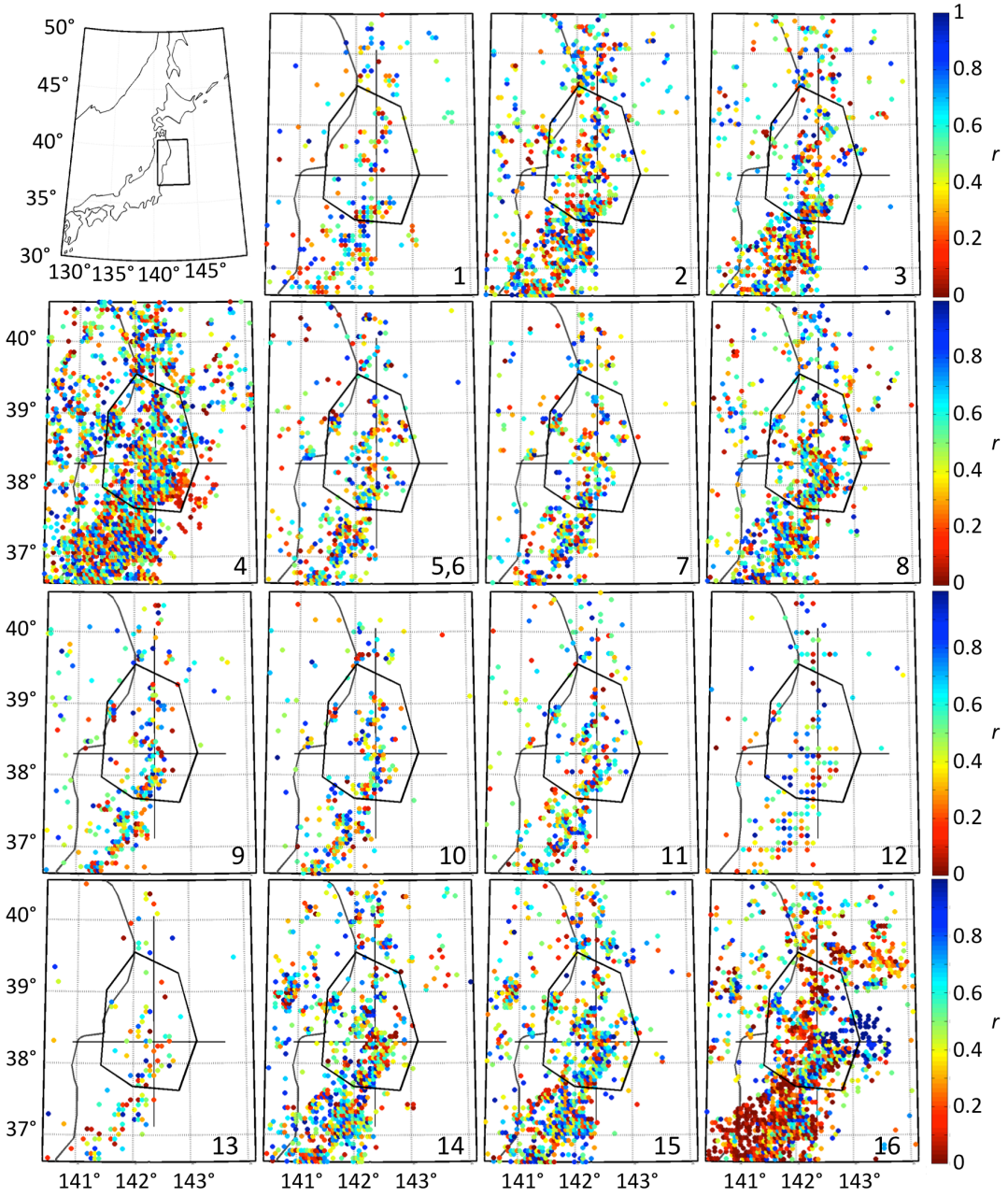

Figure 2-3. The Tohoku-Oki target region for all 16 triggers (numbered in the bottom right of each panel). The top left panel is the context map. The crosshairs mark the epicenter of the future Tohoku-Oki quake, and the polygon outlines the first 10 days of Tohoku-Oki aftershock activity within ~1° of the epicenter. The region is gridded on a fine scale (optimized for each trigger), and each colored dot represents one pair of earthquakes within that grid – one before and one after the trigger time. The color corresponds to the *r* value (Eq. 2-1); warmer colors indicate larger triggered rate change.

One trigger beyond 10º distance produces a mildly significant triggering signal (93% confidence) within the target region: the 2003 Peru earthquake (Figure 2-3, trigger 3). The nearby (3.7º) 2004 Tokachi-Oki earthquake (Figure 2-3, trigger 4) also clearly triggered earthquakes within the epicentral region of the 2011 Tohoku-Oki quake, with p-value $p_r < 10^{-16}$. Examining the effect of the Tohoku-Oki mainshock on its own epicentral region, we see that the M 7 foreshock sequence, initiated two days prior, shows up as a small patch of apparent triggered rate decrease (blue dots, Figure 2-3, trigger 16), within a robust conventional aftershock sequence that fills in the frame to the northeast and southwest.

2-3.2 Global ISC catalog – uniform Poisson reference model

We now apply the inter-event time statistic to the global ISC catalog. We measure triggering significance with respect to a stationary, uniform Poisson reference model. As mentioned in the introduction, this is an imperfect model, and it may spuriously map any non-Poissonian clustering into the triggering signal. This is problematic because we know that a Poisson process is a very poor approximation of the aftershock sequences of great earthquakes. We will correct for this in Section 2-4 by introducing a non-stationary reference model that accounts for aftershocks. However, we first present the data using the over-simplified stationary reference model in order to clearly demonstrate which of our conclusions are model-dependent. The equivalent analyses for the PDE and JMA catalogs, with respect to the uniform Poisson reference model, are included in Appendix 2-B.

Applying the inter-event time test to all sets of triggers and target regions gives a matrix of triggering detections (Figure 2-4). The triggers are sorted by time of occurrence along the y-axis, and sorted as target regions along the x-axis, such that boxes above the diagonal represent periods after the time of the great earthquake in that region, and boxes below the diagonal represent periods before the occurrence of the regional great earthquake. Trigger-target pairs that are less than 10º distant are marked with red squares, and are not included in the joint remote triggering statistics. We will delay detailed discussion of the triggering matrix for Section 2-5, after we introduce the improved reference model, and consider only the major features here.

The diagonal of the triggering matrix shows the effect of a trigger earthquake upon its own rupture area (Figure 2-4). Triggering of conventional aftershocks along this diagonal is detected with very high confidence ($p_r < 10^{-16}$). Beyond 10º distance, however, systematic triggering is not robustly evident, with $p_r = 0.17$ (Table 2-3).

The lower right triangle of the triggering matrix (Figure 2-4) is the region to examine for possible triggering precursory to great earthquakes. We do not detect systematic triggering for separations greater than 10º, with a joint triggering significance over the whole precursory population of $p_r = 0.50$ (Table 2-3). This is the expected value for exactly zero triggered rate change.

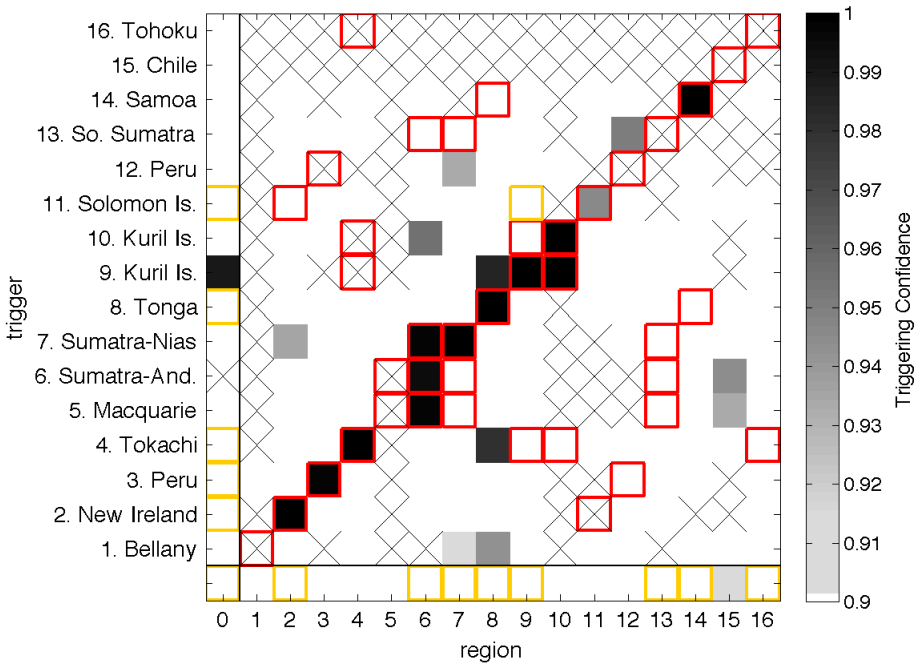

Figure 2-4. Triggering matrix for the ISC catalog, with significance measured with respect to a stationary, uniform Poisson process. The triggering matrix shows regions with rate increases above 90% confidence (grayscale). Triggers are sorted by date along the y-axis, and sorted as target regions on the x-axis. Yellow squares show where a rate increase of 67% could theoretically be detected/excluded. Red squares mark events within 10° of each other. The left-most column gives the combined triggering confidence for each trigger over all target regions (excluding those in red squares), and the bottom row shows the combined confidence for each region over all triggers (excluding red squares). The bottom left square gives the triggering confidence for the entire catalog. Crosses indicate no data for that trigger-target pair.

Table 2-3. Statistical significance: ISC catalog – Poisson reference

	r	m^a	p_r	p_{50}	p_{90}	$\delta\lambda_{50}(\delta\lambda_{05,95})$ [%]
All	0.379	621	**$<10^{-16}$**	0.10	**0.04**	**110** (87, 136)
All >10	0.486	371	0.17	0.23	0.85	9 (-6, 26)
Pre	0.500	206	0.50	0.55	0.92	0 (-18, 22)
Post	0.467	165	0.07	0.13	0.59	22 (-3, 52)

[a]sample size m is the combined total number of local earthquake pairs (t_1, t_2) in each subgroup, which can be greater than the number of great earthquake trigger-target pairs in the subgroup.

The upper left triangle of the matrix (Figure 2-4) is the region to examine for possible triggering in regions after a great earthquake. This subgroup does appear to show strong triggering, with a joint triggering significance of $p_r = 0.07$ (Table 2-3). We will now show that this apparent post-seismic triggering is due to the failure of the uniform Poisson reference model, and is not a robust feature of the dataset. The precursory triggering measurements, on the other hand, are not affected by the choice of reference model.

2-4 Methods revisited

2-4.1 Limitations of the uniform Poisson reference model.

In Section 2-3.2, the significance p_r was calculated with respect to a uniform Poisson process (Appendix 2-A). However, the regional catalogs are very non-Poissonian due to local mainshock-aftershock clustering. This is a particularly serious problem for this study, because the selection of time windows (Section 2-2.2) is conditioned on

the recent occurrence of large earthquakes – and hence their aftershocks – at the beginning of the time window.

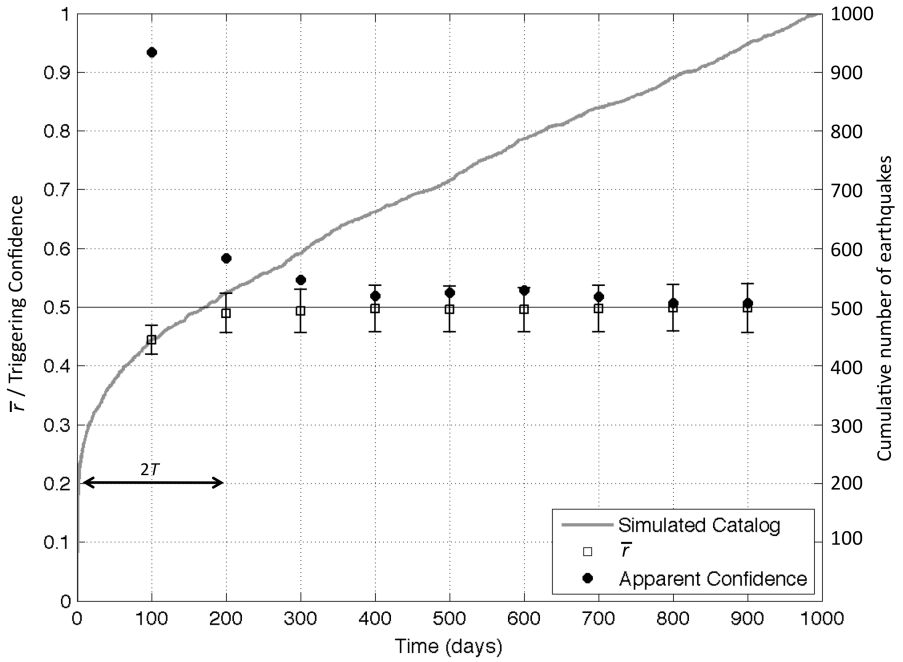

Figure 2-5. Illustration of the effect of early aftershocks on apparent triggering as measured by the inter-event time statistic r. The grey line is the cumulative number of earthquakes in a simulated catalog containing 50% background events and 50% aftershocks decaying according to Omori's law. The squares show measurements of $\bar{r}$ for hypothetical distant earthquakes occurring at 100 day intervals. The simulated target window is $2T$ = 200 days long. The simulation contains no long-range triggering effects, therefore the skew downward of $\bar{r}$ near the beginning of the aftershock sequence, and associated skew upwards of the apparent triggering confidence (circles), are effects of the aftershock sequence itself on the statistic.

Figure 2-5 shows the effect of taking a random sample of inter-event time ratios from within an ongoing aftershock sequence, and calculating significance with respect to a uniform Poisson reference model. Even though aftershock rates are decaying – which

intuition suggests might produce a spurious rate decrease in the apparent triggering metric – the r statistic actually indicates a spurious rate increase. This is because aftershocks tend to cluster toward the beginning of each target window, preferentially giving large t_1's and small t_2's (Eq. 2-1).

In order to accurately measure the effect of remote triggering at the time of the trigger, we must compute the significance of the measured $\bar{r}$ with respect to a modeled distribution that accounts for local clustering at the beginning of the time window.

2-4.2 Significance with respect to a non-stationary reference model.

The appropriate distribution of the expected value of $\bar{r}$ is modeled using a simulated catalog that reproduces the heterogeneities in rate due to local mainshock-aftershock sequences. We call this model the non-stationary or "Omori" reference model. The model catalog contains two seismicity components: 1) spontaneous background earthquakes with a statistically constant rate μ, and 2) aftershocks of large (M ≥ 8) regional and moderate local earthquakes that follow the modified Omori's law, resulting in a combined model rate $\lambda(t)$ defined by

$$\lambda(t) = \mu + \sum_{i=1}^{n} k_i (t - t_i + c)^{-p} u(t - t_i). \qquad (2\text{-}4)$$

Here k_i are the productivity terms for each of the n aftershock sequences, c and p are constants governing the time decay of aftershocks, and the unit step function $u(t - t_i)$

is zero if $t < t_i$ and one otherwise. The rate λ at some time t is hence the sum of the constant background rate and all the aftershock rates from mainshocks with times $t_i < t$.

Aftershock rates k_i are calculated for local mainshocks with a significant effect on the time series. Significant local mainshocks are identified as the minimum population of large local events sufficient to capture the observed cumulative time series within the range of the modeled time series (e.g., Figure 2-6). Local mainshocks are modeled only if their inclusion is required to achieve overlap between the modeled and observed cumulative time series, and not if they merely improve the fit by some statistical measure. This captures large non-uniformities in rate without over-fitting the time series, which could mask the signal of remote triggering. The number of significant local mainshocks ranges from $n = 0$ to 5 over the various target regions (Appendix 2-C). The smallest local mainshock magnitude is 5, and the mean magnitude is 6.4. The model rate also includes aftershocks of the local target $M_W \geq 8$ earthquake, as well as any other regional $M_W \geq 8$ earthquakes within 10°.

To verify that we are not fitting out the signal we are hoping to measure, we also have run tests in which we 1) model only the major $M \geq 8$ quakes with no local mainshocks, 2) model only the subset of local mainshocks that precedes each potential trigger, and 3) model several more or several fewer local mainshocks. None of these alternative tests results in a qualitative change in the joint statistics for any

region, trigger, or subset of the triggering matrix, and we do not include these tests in detail here.

The optimal μ, c, p, and k_i (Eq. 2-4) are found using the maximum likelihood objective function of [*Ogata*, 1992] and the Matlab constrained optimization routine *fmincon*, to enforce positivity of the parameters. The productivity terms k_i are not assumed to depend on magnitude through a productivity law as in traditional ETAS models [*Ogata*, 1992]. Instead, each k_i is treated as a free parameter. This is superior to an *a priori* productivity law because the relatively small epicentral target windows tend to crop aftershock sequences in space, disrupting the usual magnitude-productivity scaling. Our method simply attributes the triggered rate increase within the target region to the first event of the sequence (mainshock or aftershock) that happens to fall within the target region. This method produces robust inversions as long as the number of k_i remains small. The optimal parameters for each earthquake catalog, as well as the proportion of aftershocks in each target region, are reported in Appendix 2-C.

As an example, Figure 2-6 shows the observed and simulated catalogs for the epicentral region of the 2004 Sumatra earthquake, which includes the effects of three regional $M_W \geq 8$ trigger earthquakes as well as three moderate local mainshocks.

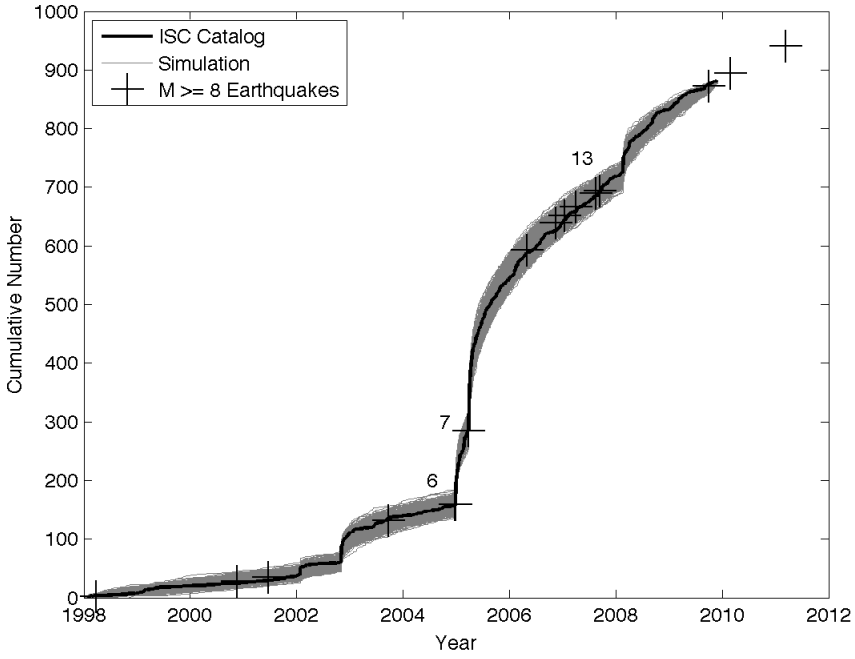

Figure 2-6. Cumulative observed seismicity (ISC catalog) in the 2004 Sumatra target region (black line) along with 1000 simulated time series (gray lines) generated from the non-stationary Omori model (Eq. 2-4). The times of all the $M_W \geq 8$ potential triggers are shown as large crosses. The ISC catalog extends only to 11/2009. The local 2004 M_W 9 Sumatra earthquake and the nearby 2005 Sumatra-Nias and 2007 Southern Sumatra earthquakes are labeled by trigger number (Table 2-1). Aftershocks from these three great triggers, as well as three significant local earthquakes, evident as small jumps in seismicity rate, are included in the modeled local seismicity rate.

To compute significance of the observed $\bar{r}$, we generate 100,000 random catalogs based on the model rate, and then draw simulated samples of inter-event time ratios r using the same time windows and sample sizes as present in the real catalog. This leads to a model distribution of values for the expected mean, denoted $\bar{r}_{sim}$. Significance of the real $\bar{r}$ is determined as the proportion of modeled $\bar{r}_{sim}$ that are

smaller than or equal to $\bar{r}$, i.e. $p_r = F_{sim}(\bar{r})$ (Figure 2-7). When computing the significance of local triggering for the regional $M_W \geq 8$ event itself, or for other nearby great earthquakes that contribute to the model rate, we remove these particular k_i from the modeled seismicity rate.

As discussed in section 2-2.1, we also estimate a triggered rate change $\delta\lambda$ based on the measured $\bar{r}$. However, we want to avoid mapping the contribution from catalog non-uniformity into the rate change. We therefore use a corrected value $\bar{r}_{corr}$, defined as the value of $\bar{r}$ that has the same significance with respect to a uniform Poisson process that the measured $\bar{r}$ has with respect to the empirical distribution.

$$F_{Poiss}(\bar{r}_{corr}) = F_{sim}(\bar{r}), \qquad (2\text{-}5)$$

where F_{Poiss} is the cumulative distribution function of $\bar{r}$ for a uniform Poisson process, and F_{sim} is the model cumulative distribution function from the simulations (Figure 2-7). Average rate change $\delta\lambda_{50}$ and confidence bounds $\delta\lambda_{05}$ and $\delta\lambda_{95}$ can be calculated from $\bar{r}_{corr}$ using the simple Poissonian step-change model (Appendix 2-A). Note that the model distribution in Figure 2-7 is only applicable for this particular subgroup of the data. The model distribution of $\bar{r}_{sim}$ must be recalculated for each particular subgroup.

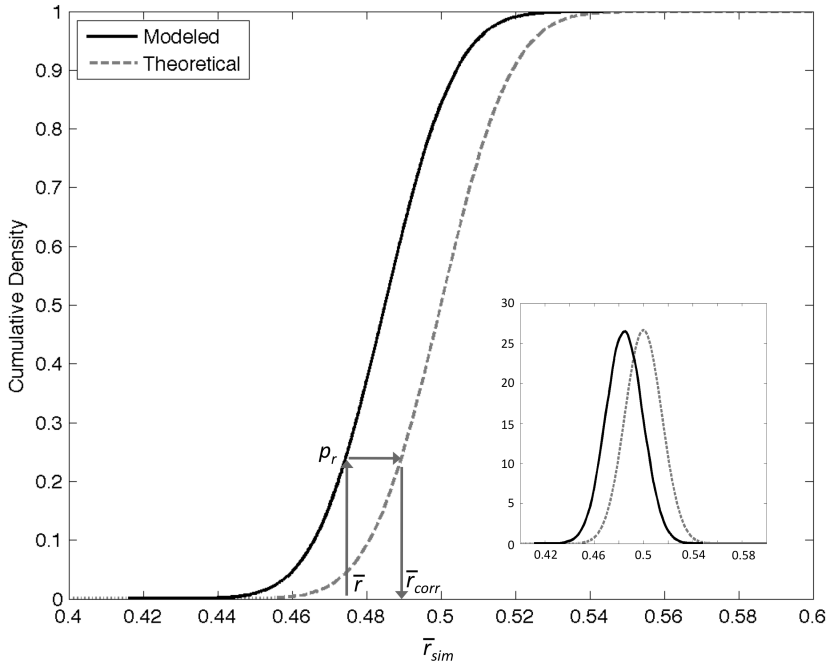

Figure 2-7. Modeled cumulative density function (cdf) of $\overline{r}_{sim}$ based on a non-stationary Omori model rate (Eq. 2-4) that includes aftershocks of major regional and local events (solid black line). The dashed line shows the theoretical distribution for a stationary Poisson model (Appendix 2-A). Inset: probability density functions. This particular example is for all trigger-target pairs greater than 10º distant (ISC catalog). The arrows show the transformation from the observed statistic $\overline{r}$ to the corrected statistic $\overline{r}_{corr}$ (Eq. 2-5).

2-5 Results: non-stationary Omori reference

2-5.1 Global ISC catalog

We again apply the inter-event time statistic to the global ISC catalog, but this time compute significance with respect to the non-stationary Omori reference model that accounts for aftershocks of major events. The post-seismic triggering signal reflected

by the statistic ($p_r = 0.07$, Table 2-3) is essentially eliminated using the more accurate reference model ($p_r = 0.40$, Table 2-4). The change in reference model does not significantly alter the other triggering statistics, however, and the triggering matrix appears qualitatively similar (Figure 2-8).

We now discuss the information presented by the ISC triggering matrix in more detail (Figure 2-8). The sensitivity of the triggering tests at individual sites is very low, due to the small target regions and poor catalog completeness at most sites. Using Eq. 2-2 to estimate the expected rate change for each trigger-target pair beyond 10º distance (mean $\delta\lambda_{\text{exp}} = 9\%$), we find that in only a single case do we have sufficient data to exclude the small rate changes anticipated by Eq. 2-2 in the approximately one-degree radius around the regional epicenter. Even a rate increase of 67% (chosen as a representative "large" rate increase) cannot be excluded in any individual case. The sensitivity of the statistic is improved however, by looking at the combined statistics for all triggers at a particular region, or the combined statistics of a particular trigger at all regions. Trigger-target pairs separated by less than 10º are excluded from this combined analysis. We also exclude the 2004 Sumatra earthquake when calculating joint triggering significance, because triggering by the Sumatra earthquake is already reflected in the data for the 2004 Macquarie earthquake, due to the overlapping target time windows (Section 2-2.2).

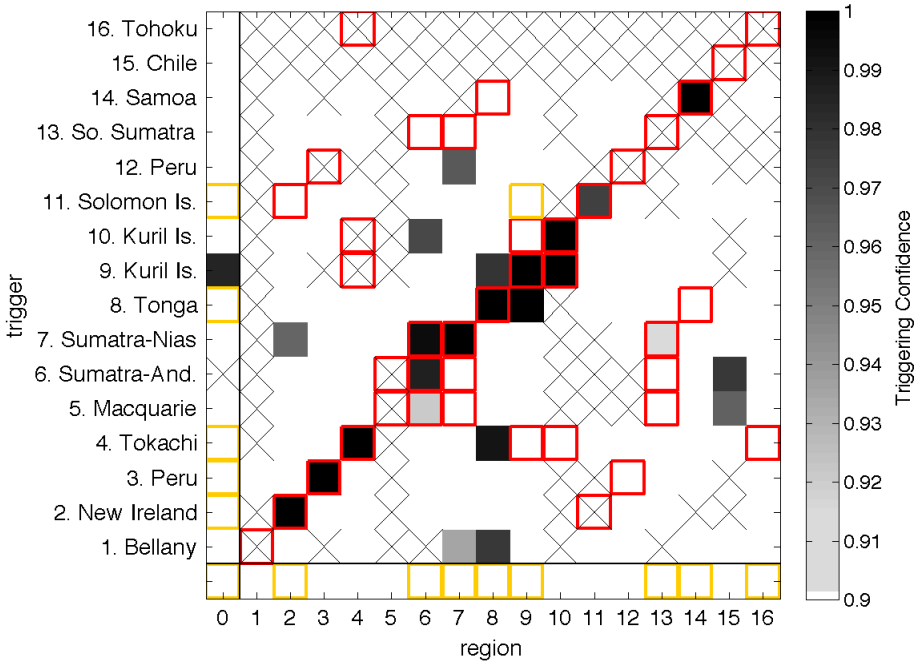

Figure 2-8. Triggering matrix for the ISC catalog, using the non-stationary Omori reference model. (Compare with Figure 2-4, using the uniform Poisson reference model.) The triggering matrix shows regions with rate increases above 90% confidence (grayscale). Triggers are sorted by date along the y-axis, and sorted as target regions on the x-axis. Yellow squares show where a rate increase of 67% could theoretically be detected/excluded. Red squares mark events within 10 degrees of each other. The left-most column gives the combined triggering confidence for each trigger over all target regions (excluding those in red squares), and the bottom row shows the combined confidence for each region over all triggers (excluding red squares). The bottom left square gives the triggering confidence for the entire catalog. Crosses indicate no data for that trigger-target pair.

Table 2-4. Statistical significance: ISC catalog – Omori reference

	$\bar{r}$	$\bar{r}_{corr}$	m^a	p_r	p_{50}	p_{90}	$\delta\lambda_{50}(\delta\lambda_{05,95})$ [%]
All	0.379	0.423	621	**$<10^{-16}$**	0.13	**0.02**	**59** (42, 79)
All >10	0.486	0.501	371	0.53	0.36	0.85	-1 (-14, 15)
Pre	0.500	0.506	206	0.62	0.64	0.82	-4 (-21, 17)
Post	0.467	0.494	165	0.40	0.20	0.76	4 (-17, 29)
1st pre	0.483	0.417	16	0.12	0.77	0.52	66 (-19, 233)
1st post	0.425	0.464	33	0.24	0.34	0.47	24 (-24, 103)

[a]sample size m is the combined total number of local earthquake pairs (t_1, t_2) in each subset, which can be greater than the number of great earthquake trigger-target pairs in the subset.

The joint triggering confidence for each trigger is depicted in the first column of the triggering matrix (Figure 2-8). We should be able to resolve joint rate changes of 67% for about 1/2 of the triggers included in the ISC catalog (yellow boxes). The 2006 Kuril Is. quake is identified as a likely trigger with confidence 97.9% at the site of the preceding 2006 Tonga quake, and joint significance p_r = 0.016 over all regions. However, this detection success is not significant when we consider the number of detection attempts, with a 21% chance of finding such an extreme significance level by chance, for at least 1 trigger out of 15. We also detect triggering in the converse direction, i.e. by the 2006 Tonga at the site of the 2006 Kuril earthquake, with confidence 99.9%. This is the highest single significance level for any distant trigger-target pair in this study, with only a 12% probability of occurring by chance, given the number of detection attempts.

The joint triggering confidence for each region as a whole is depicted in the bottom row (Figure 2-8). We do not detect significant triggering for any region and can rule out a 67% rate increase for half of the regions.

We now break the triggering matrix down into precursory and post-regional earthquake subgroup. The bottom right triangle of the triggering matrix is the place to look for precursory triggering. Triggering is detected above 90% confidence at 5 sites beyond 10º distance (Figure 2-8). (Recall that the Macquarie 2004 and Sumatra 2004 detection successes at the site of the 2010 Chile quake count as a single case (Section 2-2.2)). These 5 cases of distant triggering cannot be considered significant in the context of multiple detection attempts, however, with $p_{90} = 0.82$ (Table 2-4).

In the post-seismic, upper left triangle of the triggering matrix, we identify 4 instances of remote triggering. These 4 cases are not significant given the number of detection attempts ($p_{90} = 0.76$).

The estimated rate change (and 95% confidence bounds) for the greater than 10º distant group as a whole (pre and post-seismic) is $\delta\lambda$ = -1% (-14, 15) (Table 2-4). In the precursory group, the best estimate for triggered rate change is $\delta\lambda$ = -4% (-21, 17). In the post-regional earthquake group, the best estimate for triggered rate change is $\delta\lambda$ = 4% (-17, 29). We therefore conclude that the ISC catalog contains no

evidence of systematic earthquake triggering by distant great earthquakes at the site of other great earthquakes.

2-5.2 Global PDE catalog

The triggering calculations are carried out again for the global PDE catalog (Figure 2-9). This catalog is less complete than the ISC, with less robust statistics, but it does capture the two most recent triggers. We consider the results of the ISC catalog to be definitive where they replace PDE data. The PDE catalog reveals a pattern similar to the ISC catalog. The statistics are summarized in Figure 2-9 and Table 2-5.

The PDE data also do not show significant triggering for quakes > 10º as a whole, with $p_r = 0.83$, nor for any of the precursory or post-regional earthquake subgroups. In fact, there are fewer detection successes in the precursory subgroup (lower right triangle, Figure 2-9) than expected purely by chance ($p_{90} = 0.9$). In the post-seismic subgroup (upper right triangle), the Tohoku-Oki earthquake appears to have triggered in 3 locations at above 90% confidence (Fig, 2-9), but the joint statistics for this event are again not significant ($p_{90} = 0.09, p_r = 0.24$)

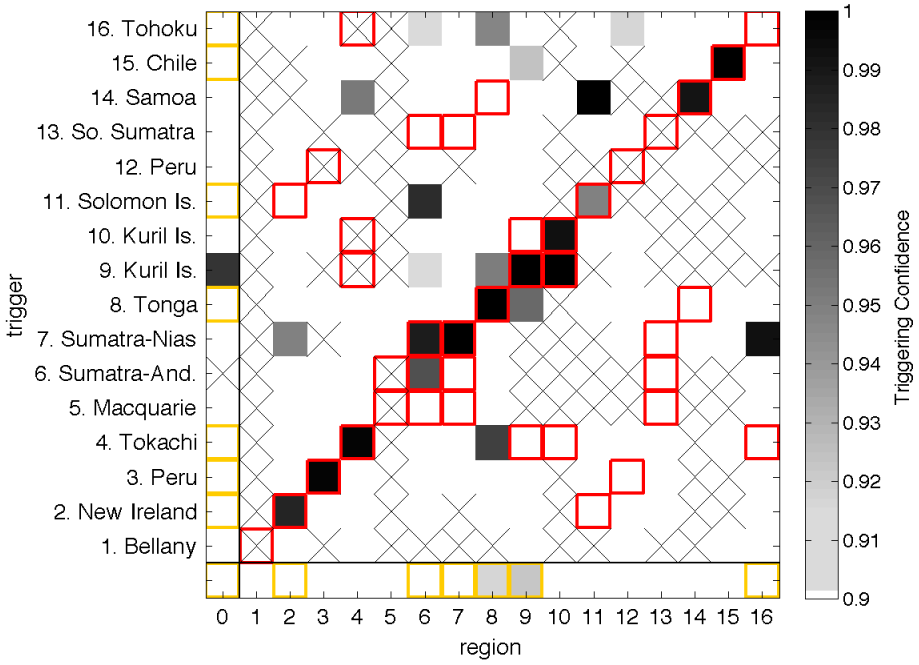

Figure 2-9. Triggering matrix for the PDE catalog, using a non-stationary Omori reference model. See Figure caption 2-8 for details.

Table 2-5. Statistical significance: PDE catalog – Omori reference

	$\bar{r}$	$\bar{r}_{corr}$	m	p_r	p_{50}	p_{90}	$\delta\lambda_{50}\,(\delta\lambda_{05,95})$ [%]
All	0.399	0.432	467	**$<10^{-16}$**	0.71	**0.01**	**50** (32, 72)
All >10	0.502	0.517	286	0.83	0.97	0.40	-9 (-23, 7)
Pre	0.564	0.572	113	1.00	1.00	0.90	-35 (-50, -15)
Post	0.461	0.483	173	0.21	0.50	0.13	11 (-11, 38)
1st pre	0.518	0.478	15	0.38	0.86	0.57	14 (-45, 135)
1st post	0.474	0.506	31	0.54	0.86	0.57	-3 (-42, 61)

Computing the joint significance region-by-region, we detect apparent triggering in both the 2006 Tonga and 2006 Kuril epicentral regions, but the significance of this number of detections is low when we consider the number of detection attempts (p_{90} = 0.45). We can rule out a 67% rate increase for one-third of the target regions.

The estimated rate change (and 95% confidence bounds) for the greater than 10º distant group as a whole is $\delta\lambda$ = -9% (-23, 7). In the precursory group, the best estimate for triggered rate change is $\delta\lambda$ = -35% (-50, -15). The statistics therefore indicate systematic triggered rate decreases in this subgroup. This is probably a catalog artifact, as this observation is not reproduced in the ISC or JMA catalogs. In the post-regional earthquake group, the best estimate for triggered rate change is $\delta\lambda$ = 11% (-11, 38). We therefore conclude that the PDE catalog also contains no evidence for systematic earthquake triggering by distant great earthquakes at the site of other impending great earthquakes.

2-5.3 JMA catalog

Finally, we examine the JMA catalog, which is the most complete in its region of coverage. The JMA catalog covers only the regions of the 2004 Tokachi-Oki and 2011 Tohoku-Oki epicenters, where it is complete to magnitude M_C = 1.3.

Triggering at sites greater than 10º distant is only observed above 90% confidence for a single trigger: 2001 Peru, but at both target sites in Japan (Figure 2-10). However, this detection success is not significant given the number of detection attempts (p_{90} = 0.79). Neither the precursory nor post-regional earthquake subgroups show significant triggering, with an estimated rate change very near zero for each (Table 2-

6). For the precursory group we get an estimated rate change (with 95% confidence bounds) $\delta\lambda = 0\%$ (-6, 7).

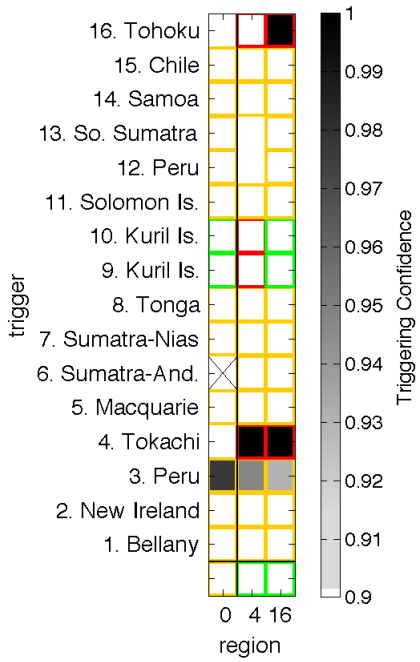

Figure 2-10. Triggering matrix for JMA catalog, using a non-stationary Omori reference model, showing the Tokachi-Oki and Tohoku-Oki regions only. Green squares show where the expected rate change (Eq. 2-2) should be resolvable, and yellow squares show where a 67% rate change should be resolvable. See caption of Figure 2-8 for other features.

Table 2-6. Statistical significance: JMA catalog – Omori reference

	$\bar{r}$	$\bar{r}_{corr}$	m	p_r	p_{50}	p_{90}	$\delta\lambda_{50}\,(\delta\lambda_{05,95})$ [%]
All	0.473	0.466	3958	**<10^{-16}**	0.70	0.21	**23** (18, 29)
All >10	0.496	0.499	2534	0.42	0.80	0.41	1 (-5, 7)
Pre	0.497	0.499	2090	0.46	0.25	0.23	0 (-6, 7)
Post	0.494	0.494	444	0.33	0.97	0.77	4 (-9, 19)

Thanks to the higher completeness of the JMA catalog, we can say with 95% confidence that the triggered rate change in both target regions in Japan is smaller than that expected from Eq. 2-2, based on triggering in California. This confirms

previous studies that have found Japan to be less triggerable than California [*Harrington and Brodsky*, 2006; *van der Elst and Brodsky*, 2010].

2-6. Discussion

2-6.1 Triggering at sites of impending large earthquakes.

The rate of recent great $M_W \geq 8$ earthquakes has increased with respect to the preceding century by 50 - 160%, depending on the time window and the method used to remove conventional aftershocks. Using the ISC catalog down to M 3.7, the best estimate for the systematic rate increase at the site of impending great earthquakes due to preceding great earthquakes is $\delta\lambda$ = -4% with lower and upper 95% confidence bounds of -21% and 17%. We can confidently conclude that there is no evidence for large or systematic triggered rate increases at the sites of impending great $M_W \geq 8$ earthquakes. If a long-range triggering process is to explain the occurrence of some great earthquakes, it must do so only rarely, or without systematically affecting the rates of earlier, smaller earthquakes at the time of the trigger.

It is more difficult to rule out triggering on a less systematic, case-by-case basis, as even doublings of rate near the epicenters of most impending earthquakes cannot be excluded with high confidence due to the scarcity of data in most places. Only the JMA catalog has adequate coverage to detect systematic triggering at the level expected from the California productivity scaling for a few cases (Figure 2-10), and where this coverage exists, triggering is not detected.

2-6.2 Magnitude of completeness required to detect small rate changes

We are reasonably confident that the earthquake catalogs do not show systematic large triggered rate changes capable of explaining recent large earthquake rates. What about smaller sequences, like those expected from other continental triggering studies, that might tell us something about earthquake processes? We now use the framework developed in this paper to estimate the magnitude of completeness needed to routinely identify small triggered sequences in subduction zones, where most great earthquakes occur. In most cases, the current network coverage is insufficient to detect the small rate changes expected from established scaling laws (Eq. 2-2). Figure 2-11 shows the corrected inter-event time statistic $\bar{r}_{corr}$ (Eq. 2-5), along with the expected value of $\bar{r}$ (Eq. 2-A8) corresponding to the rate change $\delta\lambda$ expected from Eq. 2-2, as well as the value of $\bar{r}$ required to exceed the 90% confidence threshold given the available number of observations in the ISC catalog. In no case is the number of observations (catalog completeness level) adequate to establish the expected rate change at 90% confidence.

We now estimate the number of observations that would be required to consistently detect rate changes expected from the California scaling (Eq. 2-2). If we assume that earthquakes follow the Gutenberg-Richter magnitude frequency scaling with $b = 1$, this required sample size can be expressed in terms of the required completeness magnitude. We estimate the required catalog completeness level for 1) the catalog as

a whole, 2) each target region as a whole, and 3) for each individual trigger-target pair.

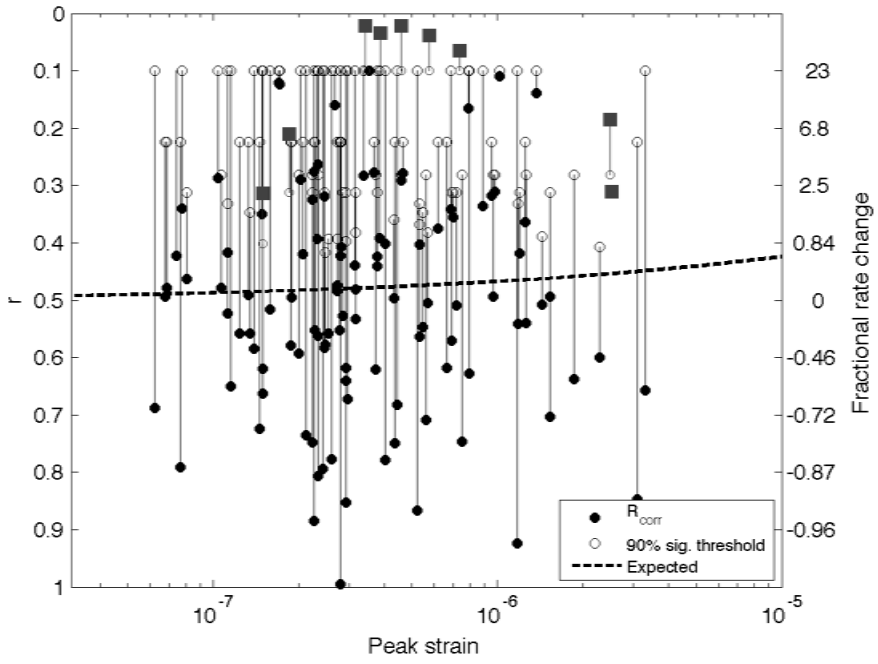

Figure 2-11. Observed $\overline{r}_{corr}$ (filled circles) compared with the $\overline{r}$ needed to exceed the 90% confidence threshold given the number of samples (open circles), for trigger-target pairs greater than 10º distance, as a function of trigger strain. Filled squares are cases where the observed rate change exceeds 90% confidence. The dashed line shows the expected $\overline{r}$ and associated rate change from Eq. 2-2. In no case is the expected rate change (dashed line) above the threshold for significance (open circles) for isolated trigger-target pairs.

The mean expected rate change, averaged over all distant trigger-target pairs, is $\delta\lambda_{\text{exp}}$ = 9%. To have 95% confidence that this rate change would produce a positive signal

in the ISC catalog (i.e. an interevent time statistic $\bar{r} < 0.5$), we would need only a relatively marginal improvement in the magnitude of completeness from 3.7 to 3.5.

On a regional basis, the required magnitude of completeness is dependent on the average seismicity rate, with less active regions requiring a proportionally lower magnitude of completeness to produce the same sample size (Table 2-7). The required magnitude of completeness for detecting the median expected rate change on a joint regional basis is 2.0. This completeness level is obtained only by the JMA catalog.

On a case-by-case basis (Figure 2-11), the magnitude of completeness would have to be considerably lower. The median required magnitude of completeness, i.e. the level required to detect distant triggering at half of all sites (median rate change $\delta\lambda_{exp} = 7\%$) is $M_C = 0.6$. This level of completeness is likely impossible without dense offshore networks of seismic stations.

Table 2-7: Required magnitude of completeness to detect expected triggering

Region	Median expected rate change $\delta\lambda_{exp}(\%)$	Number of earthquake pairs in catalog	Number of pairs required to resolve rate change $\delta\lambda_{exp}$	ISC completeness magnitude M_C	M_C required to resolve rate change $\delta\lambda_{exp}$
Balleny Is.	6	1	1596	3.7	0.5
New Ireland	7	33	959	3.7	2.2
Peru	8	14	842	3.7	1.9
Tokachi-Oki	7	22	1134	3.5	1.8
Macquarie	8	2	831	3.7	1.1
Sum.-Andaman	11	57	468	3.5	2.6
Sumatra-Nias	10	31	519	3.5	2.3
Tonga	7	47	1020	3.6	2.3
Kuril	6	43	1689	3.7	2.1
Kuril	7	1	1123	3.7	0.6
Solomon Is.	7	13	995	3.7	1.8
Peru	7	18	1204	3.7	1.9
So. Sumatra	8	21	920	3.6	2.0
Samoa	7	28	1011	3.6	2.0
Chile	9	13	663	3.7	2.0
Tohoku-Oki	14	41	293	3.5	2.6
Combined	**9**	**371**	**664**	**3.7**	**3.5**

2-6.3 Limitations

Great earthquake interactions are only considered here in terms of local cascade dynamics. Other possibilities for linking great earthquakes might be: 1) triggering a deep slow slip event [*Shelly et al*., 2011] that then initiates a great earthquake at the down dip extent of locking; or 2) viscous stress transfer in the lower crust and upper mantle, operating on a much longer timescale than the passage of seismic waves [*Freed and Lin*, 1998; *Pollitz et al*., 1998]. A careful search for remotely triggered

tectonic tremor down-dip of impending earthquakes could evaluate whether great earthquakes are linked through triggered deep slip.

We have looked only at the largest magnitude potential triggers. The largest triggers are the most likely places to look for a response, but smaller magnitude triggers may be cumulatively just as important in triggering distant rate changes, due to their proportionally greater number [*Helmstetter et al*., 2005]. Triggering may also be influenced by precise stress orientations of dynamic waves, which vary with fault geometry and relative location of trigger events and target nucleation zones [*Hill*, 2008]. In some cases, a smaller nearby event may be more efficient for triggering at a particular target.

2-7. Conclusion

We have systematically measured triggered rate changes at the sites of 16 $M_W \geq 8$ earthquakes, at the times of other $M_W \geq 8$ earthquakes, during the high-great earthquake rate period between 1998 and 2011. We find no evidence that $M_W \geq 8$ earthquakes trigger precursory activity at the site of other impending $M_W \geq 8$ earthquakes, and systematic triggering on a scale capable of explaining a 50-160% increase in the rate of $M_W \geq 8$ earthquakes can be ruled out with 95% confidence.

The data are, however, consistent with expected rate changes given the amplitude of seismic shaking at the target sites, although an improvement in completeness

magnitude from 3.7 to 3.5 would be required to definitively establish small rate changes.

There is no apparent increase in regional triggering susceptibility that might serve as a precursory signal of impending earthquakes, at least using current catalogs. However, regional networks with a magnitude of completeness down to 2.0 would be required to adequately resolve expected triggered rate changes on a region-by-region basis.

2-8 Data and Resources

Several earthquake catalogs were used in this study. ISC data through 2007 were obtained on CDs from the International Seismological Centre, and supplemented with data through 11/2009 via ftp from www.isc.ac.uk (last accessed December 15, 2011). The PDE catalog was downloaded via ftp from the United States Geological Survey website, http://earthquake.usgs.gov/research/data/pde.php (last accessed November 14, 2011). The JMA catalog was manually copied-and-pasted in 7-day increments from the Japan Meteorological Agency website at www.hinet.bosai.go.jp (last accessed November 22, 2011, account required). The USGS PAGER catalog, used to define the list of $M_W \geq 8$ earthquakes, is available from earthquake.usgs.gov/research/data. Seismograms were obtained from the IRIS Data Management Center at www.iris.edu and processed in SAC. Many seismographic networks contributed data through IRIS.

Acknowledgements. This work was supported by NSF grant EAR-0838598.

Appendix 2-A: Distribution of the sample mean of *r*

We use the sampling distribution of the mean inter-event time ratio $\bar{r}$ to calculate the significance of $\bar{r}$ with respect to a Poisson process, as well as to find the minimum rate increase at which the Poisson process could be rejected. The distribution of $\bar{r}$ in the case of zero rate change is known, as r is uniform on [0,1]. The distribution of the sum $s = m\bar{r}$ of a sample of uniform distributed random variables is [*Uspensky*, 1937]

$$f_S(s|m) = \sum_{k=0}^{m} (-1)^k \frac{m}{k!(m-k)!} (s-k)^{m-1} u(s-k). \qquad \text{(2-A1)}$$

Here u is the unit step function. In this Appendix, we use the convention that distributions are subscripted by their applicable variable in uppercase. The distribution of the mean is the distribution (2-A1) rescaled over the range [0,1], i.e.

$$f_{\bar{R}}(\bar{r}) = m f_S(m\bar{r}). \qquad \text{(2-A2)}$$

$$f_{\bar{R}}(\bar{r}|m) = \sum_{k=0}^{m} (-1)^k \frac{m^2}{k!(m-k)!} (m\bar{r}-k)^{m-1} u(m\bar{r}-k). \qquad \text{(2-A3)}$$

This distribution very rapidly approaches the normal distribution as m increases (Figure 2-A1).

The distribution of $\bar{r}$ for an arbitrary rate change $\delta\lambda$ is required to compute confidence bounds, i.e. the minimum and maximum rate changes that could pass the Poisson hypothesis test. Van der Elst and Brodsky [*2010, Appendix A*] derived the

expectation of r for a step change in a Poisson process (Section 1-A). Here we give the full distribution function.

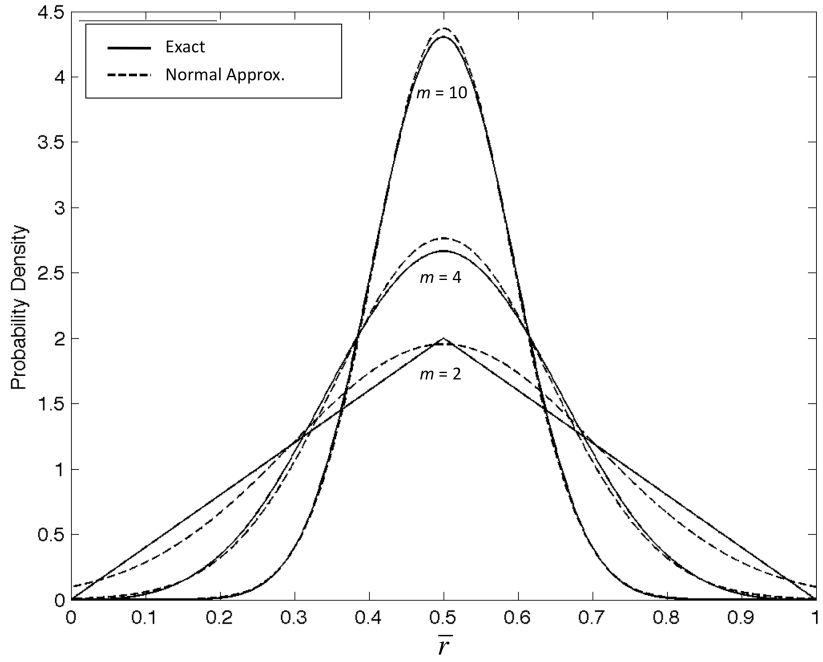

Figure 2-A1 Distribution of the sample mean $\bar{r}$ for a stationary Poisson process (Eq. 2-A3), for various sample sizes m. Solid lines are the exact solution given by Eq. 2-A3, and the dashed lines show the approximation using a normal distribution.

The distribution of r (defined in Eq. 2-1, main text) with t_1 and t_2 drawn from distinct Poisson processes with intensities λ_1 and λ_2, respectively, is

$$f_R\left(r\middle|\lambda_1,\lambda_2\right)=\frac{\lambda_1\lambda_2}{\left[\left(1-r\right)\lambda_1+r\lambda_2\right]^2}\cdot \tag{2-A4}$$

This equation follows from transforming the joint probability distribution of two independent, exponentially distributed times t_1 and t_2, with means λ_1^{-1} and λ_2^{-1}, into a function of the random variable r [*van der Elst and Brodsky, 2010*].

Defining fractional rate change as

$$\delta\lambda \equiv \frac{\lambda_2 - \lambda_1}{\lambda_1}, \tag{2-A5}$$

and substituting (2-A5) into (2-A4) gives

$$f_R\left(r|\delta\lambda\right) = \frac{\delta\lambda + 1}{\left(1 + \delta\lambda \cdot r\right)^2}. \tag{2-A6}$$

The distribution of the sample mean $\bar{r}$ (i.e., the first moment) as a function of fractional rate change $\delta\lambda$ and sample size m cannot be obtained analytically, as the moment generating function for (2-A6) is expressible only with special functions. For small samples ($m < 10$), we use numerical convolution to obtain the distribution and cumulative distribution of the sum s [*Grinstead and Snell*, 1997], and then rescale this distribution (Eq. 2-A2) to obtain the distribution of the mean $\bar{r}$.

For larger samples ($m > 10$), we take advantage of the central limit theorem to obtain an analytical approximation of the distribution of the mean. The central limit theorem guarantees that the distribution of the mean of any random variable with mean μ and finite variance σ^2 approaches a normal distribution with mean μ and variance σ^2/m as

sample size m increases [*Casella and Berger*, 2002]. The mean of r as a function of $\delta\lambda$ can be found by computing the expectation from (A6):

$$\mu_r(\delta\lambda) = \int_0^1 r f_R(r|\delta\lambda)\, dr\ . \tag{2-A7}$$

$$\mu_r(\delta\lambda) = \frac{1}{\delta\lambda^2}\left[(\delta\lambda+1)\ln(\delta\lambda+1) - \delta\lambda\right], \tag{2-A8}$$

and the variance (expressed as a function of the mean for simplicity) is

$$\sigma_r^2(\delta\lambda) = \frac{1}{\delta\lambda}\left[1 - 2\mu_r\right] - \mu_r^2\ . \tag{2-A9}$$

In the limit of $\delta\lambda = 0$, the mean μ_r and variance σ_r^2 can be shown to be 1/2 and 1/12, respectively, consistent with a uniform distribution on [0,1]. We find that the normal approximation using (2-A8) and (2-A9) is very good for $m > 10$ and $\delta\lambda < 1$.

The significance of $\bar{r}$ is defined as the probability p_r that a uniform random process would produce a smaller mean than that observed, by chance:

$$p_r \equiv F_{\bar{R}}(\bar{r}), \tag{2-A10}$$

where $F_{\bar{R}}$ is the cumulative distribution function. Using the normal approximation with (2-A8) and (2-A9),

$$F_{\bar{R}}(\bar{r}) \cong \Phi\left[\bar{r}\,|\mu_r(0), \sigma_r^2(0)/m\right], \tag{2-A11}$$

Where Φ is the cumulative normal distribution.

Inverting the statistic (2-A10) gives the confidence bounds on the rate change parameter $\delta\lambda$ [*Casella and Berger*, 2002]. The maximum bound on the rate change $\delta\lambda$, at significance level α (e.g. 0.05), is the value of $\delta\lambda$ for which

$$\alpha = F_{\bar{R}}\left(\delta\lambda|\bar{r}\right) \cong \Phi\left[\bar{r}\,\middle|\,\mu_r(\delta\lambda), \sigma_r^2(\delta\lambda)/m\right]. \qquad \text{(2-A12)}$$

Given $\bar{r}$, m, and α, we solve iteratively for $\delta\lambda$. To obtain the minimum bound on $\delta\lambda$, we solve (2-A12) for $\alpha' = 1 - \alpha$.

Appendix 2-B: Analysis of PDE and JMA catalogs – uniform Poisson reference

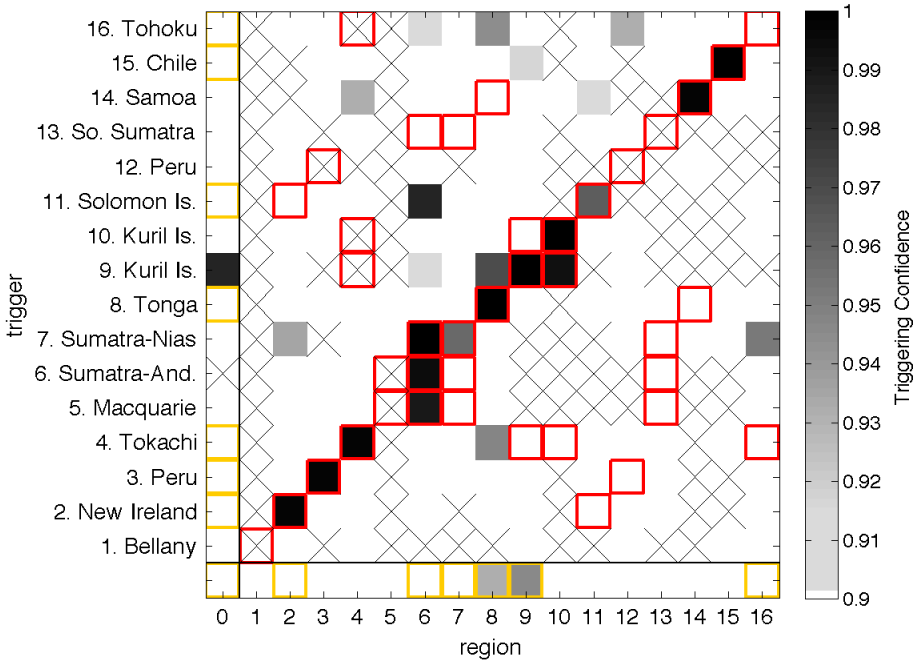

Figure 2-B1. Triggering matrix for the PDE catalog, with significance measured with respect to a stationary, uniform Poisson process. The triggering matrix shows regions with rate increases above 90% confidence (grayscale). Triggers are sorted by date along the y-axis, and sorted as target regions on the x-axis. Yellow squares show where a rate increase of 67% could theoretically be detected/excluded. Red squares mark events within 10º of each other. The left-most column gives the combined triggering confidence for each trigger over all target regions (excluding those in red squares), and the bottom row shows the combined confidence for each region over all triggers (excluding red squares). The bottom left square gives the triggering confidence for the entire catalog. Crosses indicate no data for that trigger-target pair.

Table 2-B1. Statistical significance: PDE catalog – Poisson reference

	r	m	p_r	p_{50}	p_{90}	$\delta\lambda_{50}(\delta\lambda_{05,95})$ [%]
All	0.399	467	**2×10^{-14}**	0.53	**0.01**	**85** (62, 111)
All >10	0.502	286	0.54	0.88	0.52	-1 (-16, 17)
Pre	0.564	113	0.99	1.00	0.97	-32 (-48, -11)
Post	0.461	173	**0.04**	0.23	0.13	**26** (2, 57)
1st pre	0.518	15	0.59	0.86	1.00	-10 (-56, 85)
1st post	0.474	31	0.31	0.36	0.57	17 (-30, 94)

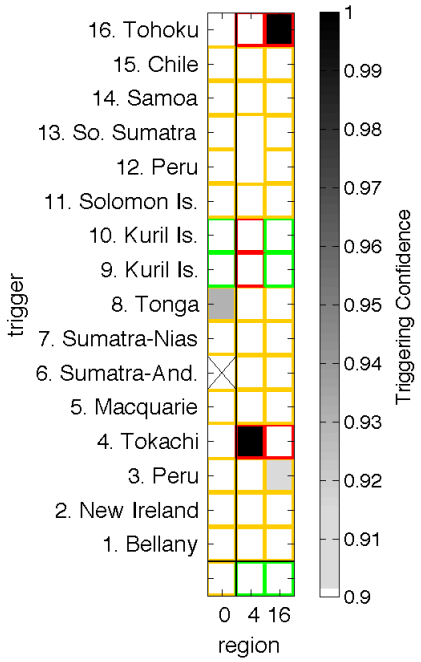

Figure 2-B2. Triggering matrix for JMA catalog, using a stationary, uniform Poisson reference model, showing the Tokachi-Oki and Tohoku-Oki regions only. Green squares show where the expected rate change (Eq. 2-2) should be resolvable, and yellow squares show where a 67% rate change should be resolvable. See caption of Figure 2-B1 for other features.

Table 2-B2. Statistical significance: JMA catalog – Poisson reference

	r	M	p_r	p_{50}	p_{90}	$\delta\lambda_{50}(\delta\lambda_{05,95})$ [%]
All	0.473	3958	**2×10^{-9}**	0.50	0.05	**18** (12, 23)
All >10	0.496	2534	0.27	0.69	0.49	2 (-3, 8)
Pre	0.497	2090	0.32	0.93	0.90	2 (-4, 8)
Post	0.494	444	0.33	0.21	0.16	4 (-9, 18)

Appendix 2-C. Omori model parameters

This appendix contains the parameters used in the non-stationary Omori reference models (Eq. 2-4). It also lists the total fraction of the simulated catalog made up of aftershocks (local, regional, and target events), the fraction that is aftershocks of the target M ≥ 8 earthquake itself, and the number of local significant mainshocks used to fit the time series.

Table 2-C1. ISC catalog

Region	μ [yr^{-1}]	c [days]	p	Fraction aftershocks	Frac. direct aftershocks	Num. local mainshocks[a]
Balleny Is.	1.2	0.25	1.18	0.74	0.74	0
New Ireland	14.5	0.07	1.00	0.39	0.34	1
Peru	5.8	0.56	1.66	0.69	0.69	0
Tokachi-Oki	6.8	0.03	1.01	0.64	0.55	2
Macquarie Is.	0.1	0.03	1.13	0.97	0.97	0
Sumatra-Andaman	9.9	0.03	0.80	0.87	0.28	3
Sumatra-Nias	4.2	0.13	0.89	0.87	0.83	1
Tonga	20.7	0.73	1.26	0.51	0.43	4
Kuril Is.	11.9	0.09	1.00	0.81	0.45	3
Kuril Is.	1.1	0.48	1.50	0.96	0.27	0
Solomon Is.	4.9	0.47	1.23	0.78	0.60	4
Central Peru	5.5	0.14	1.21	0.73	0.70	1
So. Sumatra	1.6	0.04	0.89	0.93	0.60	2
Samoa	14.3	0.10	1.08	0.35	0.35	0
Chile[b]	7.2	0.05	1.01	0.00	0.00	0
Tohoku-Oki[b]	13.6	0.01	0.86	0.49	0.00	4

[a]local mainshocks with M < 8, only

[b]Does not include the local M ≥ 8 earthquake itself due to catalog time limit

Table 2-C2. PDE Catalog

Region	μ [yr^{-1}]	c [days]	p	Fraction aftershocks	Frac. direct aftershocks	Num. local mainshocks[a]
Balleny Is.	0.7	0.19	1.38	0.49	0.49	0
New Ireland	8.4	0.04	0.95	0.42	0.35	1
Peru	3.8	0.44	1.38	0.69	0.69	0
Tokachi-Oki	5.3	0.04	0.95	0.70	0.55	4
Macquarie Is.	0.1	0.06	1.21	0.96	0.96	0
Sumatra-Andaman	3.4	0.07	0.82	0.92	0.26	4
Sumatra-Nias	3.3	0.09	0.89	0.87	0.73	2
Tonga	12.4	0.92	1.26	0.57	0.47	5
Kuril Is.	8.1	0.10	1.01	0.77	0.42	3
Kuril Is.	1.0	0.58	1.56	0.94	0.20	0
Solomon Is.	4.4	0.46	1.40	0.78	0.36	5
Central Peru	4.8	0.13	1.18	0.71	0.69	1
So. Sumatra	1.5	0.04	0.85	0.90	0.64	2
Samoa	2.4	0.08	1.17	0.51	0.51	0
Chile	11.8	0.56	1.21	0.75	0.68	1
Tohoku-Oki	12.8	0.62	1.02	0.77	0.65	4

[a]local mainshocks with M < 8, only

Table 2-C3. JMA Catalog

Region	μ [yr^{-1}]	c [days]	p	Fraction aftershocks	Frac. direct aftershocks	Num. local mainshocks[a]
Tokachi-Oki	175	0.07	0.86	0.59	0.45	4
Tohoku-Oki[b]	2037	0.05	0.94	0.20	0.00	2

[a]local mainshocks with M < 8, only

[b]Does not include the local M ≥ 8 earthquake itself because there are no subsequent triggers.

References

Ammon, C. J., T. Lay, and D. W. Simpson (2010), Great Earthquakes and Global Seismic Networks, *Seismological Research Letters*, *81*(6), 965-971.

Anderson, J. G., J. N. Brune, J. N. Louie, Y. H. Zeng, M. Savage, G. Yu, Q. B. Chen, and D. Depolo (1994), Seismicity in the Western Great Basin apparently triggered by the Landers, California, Earthquake, 28 June 1992, *Bulletin of the Seismological Society of America*, *84*(3), 863-891.

Beeler, N. M., and D. A. Lockner (2003), Why earthquakes correlate weakly with the solid Earth tides: Effects of periodic stress on the rate and probability of earthquake occurrence, *Journal of Geophysical Research*, *108*(B8), doi:10.1029/2001jb001518.

Brodsky, E. E. (2009), The 2004-2008 worldwide superswarm, *Eos Trans. AGU*, *90*(52), Fall Meet. Suppl., Abstract S53B-06.

Casella, G., and R. L. Berger (2002), *Statistical inference*, 2nd ed., xxviii, 660 pp., Thomson Learning, Australia ; Pacific Grove, CA.

Felzer, K. R., T. W. Becker, R. E. Abercrombie, G. Ekstrom, and J. R. Rice (2002), Triggering of the 1999 M-W 7.1 Hector Mine earthquake by aftershocks of the 1992 M-W 7.3 Landers earthquake, *Journal of Geophysical Research*, *107*(B9), doi:10.1029/2001jb000911.

Felzer, K. R., R. E. Abercrombie, and G. Ekstrom (2004), A common origin for aftershocks, foreshocks, and multiplets, *Bulletin of the Seismological Society of America*, *94*(1), 88-98.

Felzer, K. R., and E. E. Brodsky (2005), Testing the stress shadow hypothesis, *Journal of Geophysical Research*, *110*(B5), B05S09.

Freed, A. M., and J. Lin (1998), Time-dependent changes in failure stress following thrust earthquakes, *Journal of Geophysical Research*, *103*(B10), 24393-24409.

Gomberg, J. (2001), The failure of earthquake failure models, *Journal of Geophysical Research-Solid Earth*, *106*(B8), 16253-16263.

Gomberg, J., P. Bodin, K. Larson, and H. Dragert (2004), Earthquake nucleation by transient deformations caused by the M=7.9 Denali, Alaska, earthquake, *Nature*, *427*(6975), 621-624.

Gomberg, J., and P. Johnson (2005), Seismology - Dynamic triggering of earthquakes, *Nature*, *437*(7060), 830-830.

Grinstead, C. M., and J. L. Snell (1997), *Introduction to Probability*, American Mathematical Society.

Harrington, R. M., and E. E. Brodsky (2006), The absence of remotely triggered seismicity in Japan, *Bulletin of the Seismological Society of America*, *96*(3), 871-878.

Helmstetter, A., Y. Y. Kagan, and D. D. Jackson (2005), Importance of small earthquakes for stress transfers and earthquake triggering, *Journal of Geophysical Research*, *110*(B5), B05S08.

Hill, D. P., and S. G. Prejean (2007), *Dynamic Triggering*, Treatise on Geophysics, Ed. H. Kanamori, Elsevier.

Hill, D. P. (2008), Dynamic stresses, Coulomb failure, and remote triggering, *Bulletin of the Seismological Society of America*, *98*(1), 66-92.

Lay, T., and T. C. Wallace (1995), *Modern Global Seismology*, Academic Press, San Diego.

Lei, X. L., C. D. Xie, and B. H. Fu (2011), Remotely triggered seismicity in Yunnan, southwestern China, following the 2004 M(w)9.3 Sumatra earthquake, *Journal of Geophysical Research*, *116*

Michael, A. J. (2011), Random variability explains apparent global clustering of large earthquakes, *Geophysical Research Letters*, *38*

Nalbant, S. S., S. Steacy, K. Sieh, D. Natawidjaja, and J. McCloskey (2005), Earthquake risk on the Sunda trench, *Nature*, *435*(7043), 756-757.

Ogata, Y. (1992), Detection of precursory relative quiescence before great earthquakes through a statistical-model, *Journal of Geophysical Research*, *97*(B13), 19845-19871.

Parsons, T., and A. A. Velasco (2011), Absence of remotely triggered large earthquakes beyond the mainshock region, *Nature Geoscience*, *4*(5), 312-316.

Peng, Z. G., D. P. Hill, D. R. Shelly, and C. Aiken (2010), Remotely triggered microearthquakes and tremor in central California following the 2010 M(w) 8.8 Chile earthquake, *Geophysical Research Letters*, *37*

Pollitz, F. F., R. Burgmann, and B. Romanowicz (1998), Viscosity of oceanic asthenosphere inferred from remote triggering of earthquakes, *Science*, *280*(5367), 1245-1249.

Rubinstein, J. L., G. C. Beroza, J. Brown, M. Brudzinski, J. Gomberg, S. Malone, D. H. Oppenheimer, Z. G. Peng, S. G. Prejean, H. M. Savage, D. R. Shelly, A. Wech, and M. West (2011), Widespread triggering of earthquakes and tremor by the 2011 M9.0 off-Tohoku earthquake, *Seismological Research Letters*, *82*(2), 273-361.

Savage, H. M., and C. Marone (2008), Potential for earthquake triggering from transient deformations, *Journal of Geophysical Research*, *113*(B5), B05302, doi 05310.01029/02007jb005277.

Shearer, P. M., and P. B. Stark (2011), Global risk of big earthquakes has not recently increased, *Proc. Natl. Acad. Sci.*, *109*(3), 717-721.

Shelly, D. R., Z. G. Peng, D. P. Hill, and C. Aiken (2011), Triggered creep as a possible mechanism for delayed dynamic triggering of tremor and earthquakes, *Nature Geoscience*, *4*(6), 384-388.

Uspensky, J. B. (1937), *Introduction to Mathematical Probability*, McGraw-Hill, New York.

van der Elst, N. J., and E. E. Brodsky (2010), Connecting near-field and far-field earthquake triggering to dynamic strain, *J. Geophys. Res.*, *115*(B07311)

Velasco, A. A., S. Hernandez, T. Parsons, and K. Pankow (2008), Global ubiquity of dynamic earthquake triggering, *Nature Geoscience*, *1*(6), 375-379.

West, M., J. J. Sanchez, and S. R. McNutt (2005), Periodically triggered seismicity at Mount Wrangell, Alaska, after the Sumatra earthquake, *Science*, *308*(5725), 1144-1146.

Wiseman, K., and R. Burgmann (2011), Stress and Seismicity Changes on the Sunda Megathrust Preceding the 2007 M(w) 8.4 Earthquake, *Bulletin of the Seismological Society of America*, *101*(1), 313-326.

Wu, C. Q., Z. G. Peng, W. J. Wang, and Q. F. Chen (2011), Dynamic triggering of shallow earthquakes near Beijing, China, *Geophysical Journal International*, *185*(3), 1321-1334.

Chapter 3. Auto-acoustic compaction in steady shear flows: Experimental evidence for suppression of shear dilatancy by internal acoustic vibration

Nicholas J. van der Elst[1], Emily E. Brodsky[1],

Pierre-Yves Le Bas[2] and Paul A. Johnson[2]

[1]*Dept. of Earth and Planet. Science, 1156 High St., Univ. of California, Santa Cruz, California 95060*

[2]*Geophysics Group, Los Alamos National Laboratory, P.O. Box 1663, Los Alamos, New Mexico 87545*

Abstract: Granular shear flows are intrinsic to many geophysical processes, ranging from landslides and debris flows to earthquake rupture on gouge-filled faults. The rheology of a granular flow depends strongly on the boundary conditions and shear rate. Earthquake rupture involves a transition from quasi-static to rapid shear rates. Understanding the processes controlling the transitional rheology is potentially crucial for understanding the rupture process and the coseismic strength of faults. Here we explore the transition experimentally using a commercial torsional rheometer. We measure the thickness of a steady shear flow at velocities between 10^{-3} and 10^{2} cm/s, at very low normal stress (7 kPa), and observe that thickness is reduced at intermediate velocities (0.1 - 10 cm/s) for angular particles, but not for smooth glass beads. The maximum reduction in thickness is on the order of 10% of the active shear zone thickness, and scales with the amplitude of shear-generated acoustic vibration. By examining the response to externally applied vibration, we show that the thinning reflects a feedback between internally generated acoustic vibration and granular rheology. We link this phenomenon to acoustic compaction of a dilated granular medium, and formulate an empirical model for the steady-state thickness of

a shear-zone in which shear-induced dilatation is balanced by a newly identified mechanism we call auto-acoustic compaction. This mechanism is activated when the acoustic pressure is on the order of the confining pressure, and results in a velocity-weakening granular flow regime at shear rates four orders of magnitude below those previously associated with the transition out of quasi-static granular flow.

3-1. Introduction

Frictional sliding processes in geophysics often involve granular shear flows at the sliding interface. This is true for landslides and debris flows, as well as for earthquake ruptures within granulated damage zones or gouge-filled faults. The frictional strength in these contexts is controlled by the rheology of the granular flow, which has a strong dependence on shear rate and boundary conditions [*Campbell*, 2006; *Clement*, 1999; *Iverson*, 1997; *Savage*, 1984].

For different shear rates, confining stresses, and packing densities, the description of a granular flow can range from "solid-like" to "gas-like" [*Jaeger et al.*, 1996], albeit with complicated second-order behavior in each regime. The appropriate description for a particular flow is typically determined by the dimensionless inertial number, which compares the magnitude of the grain inertial stresses to the confining stress [*Bocquet et al.*, 2001; *Campbell*, 2006; *Clement*, 1999; *Iverson*, 1997; *Jop et al.*, 2006; *Lu et al.*, 2007; *Savage*, 1984].

$$I \equiv \frac{\rho d^2 \dot{\gamma}^2}{p}, \quad (3\text{-}1)$$

where ρ is density, d is grain diameter, $\dot{\gamma}$ is the strain rate, and p is the confining (normal) pressure. The shear rate profile in boundary driven flows is commonly observed to decay approximately exponentially [*Bocquet et al.*, 2001; *Veje et al.*, 1999] (Appendix 3-A), such that $\dot{\gamma} \sim v/d$ where v is the boundary velocity, and Eq. 3-1 simplifies to

$$I = \frac{\rho v^2}{p}. \quad (3\text{-}2)$$

In the solid-like or quasi-static regime ($I << 1$), forces are transmitted elastically through a network of grain contacts, called force chains, and the shear and normal stresses at the boundaries are related to the stiffness and orientations of these chains (Fig. 3-1a) [*Majmudar and Behringer*, 2005]. In this regime, force chains are continually created and destroyed through shearing, but the rate of buckling and destruction of old force chains is equal to the rate of creation of new ones, and the shear resistance is, to first order, independent of the shear rate (Fig 3-1c). This results in a solid-like frictional rheology. In the gas-like, inertial flow regime ($I >> 1$), stresses are supported through grain-grain or grain-boundary collisions, analogous to a kinetic gas model (Fig. 3-1b). The shear and normal stresses are then related to the particle momentum transfer rate, resulting in a power-law viscous-like rheology (Fig. 3-1c) [*Bagnold*, 1954; *Campbell*, 2005].

Earthquake rupture and debris flows likely involve a transition between quasi-static and rapid inertial shear, in which vibration and momentum become important for the rheology of the flow. A description of granular rheology in this transitional regime is therefore required for a full understanding of the process of rupture nucleation and propagation. However, our understanding of the rheology of dense, rapid granular flows ($I \sim 1$) is far from complete.

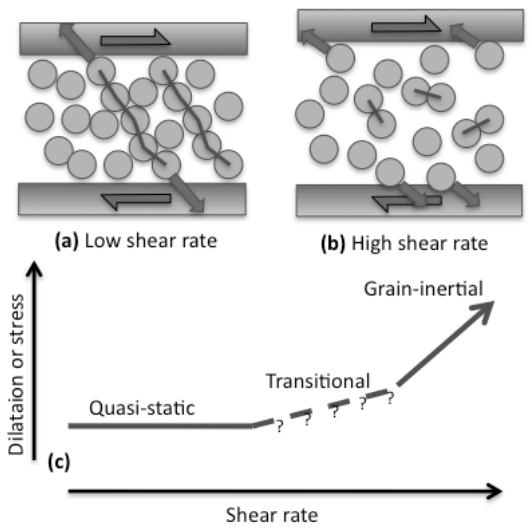

Figure 3-1. Cartoon depiction of end-member granular flow regimes. **(a)** In the low shear rate quasi-static regime, boundary stresses are supported elastically through force chains. Thin lines represent grain-grain contacts and arrows represent forces acting on the boundaries. **(b)** In the high shear-rate grain-inertial regime, stresses are supported through momentum transfer in collisions. **(c)** Cartoon of experimental behavior in end member regimes. The y-axis represents stress under constant volume conditions or shear zone thickness under constant stress conditions. In the quasi-static regime, shear dilatation and stress are independent of shear rate, resulting in a friction-like rheology. In the grain inertial regime, dilatation and stress are proportional to the momentum transfer rate, resulting in a power-law viscous-like rheology. This study focuses on the intermediate shear rate transitional regime, where stresses are supported elastically, but vibration becomes important for force chain stability.

Some of the difficulty in describing the rheology of a dense, rapid granular flow arises from the athermal nature of the granular medium. Unlike a traditional gas or liquid, a granular material does not explore particle configurations and approach an

equilibrium state in the absence of an external energy source [*Jaeger et al*., 1996]. Consequently, the rheology of a granular medium depends strongly on the detailed configuration of grains. Under the same pressure or volume conditions, some grain (packing) configurations can be very stiff, while others may be soft or 'fluidized.' A striking example of this dependency on grain configuration is the phenomenon of jamming/unjamming [*Liu and Nagel*, 2010] where a granular medium transitions dramatically from a solid-like to a fluid-like phase, or vice-versa, under small perturbations to particle configuration or loading direction [*Aharonov and Sparks*, 1999; *Cates et al*., 1998; *Liu and Nagel*, 1998].

A good way to un-jam a granular material is to add vibration. This provides an external energy source that allows a granular system to explore packing configurations. Vibration usually leads to a more compact configuration, depending on the initial packing density and the amplitude of the vibration [*Knight et al*., 1995; *Nowak et al*., 1997]. Another source of external energy is imposed shear. Under shear, a granular medium may dilate or compact, depending on its starting configuration. Starting from a dense state, such as random (or ordered) close packing, it must dilate in order to allow geometrically frustrated grains to move past each other (i.e. un-jam) [*Lu et al*., 2007; *Marone*, 1991; *Reynolds*, 1885]. Acoustic vibration and imposed shear are thus two sources of external energy that tend to drive the packing density of a granular system in opposite directions.

For gouge-filled faults, both acoustic and shear energy sources are present, with acoustic energy generated during rupture, or arriving in seismic waves from nearby earthquakes. In granular shear experiments, bursts of acoustic vibration can trigger compaction and stick-slip events and generate lasting changes in rheology [*Johnson et al*., 2008; *Johnson et al*., *in press* 2012]. In other experiments, vibration has caused a transition from a disordered to a crystallized (perfectly ordered) state when the kinetic energy of vibration balances that of shearing [*Daniels and Behringer*, 2005]. Acoustic fluidization, in which scattered wave energy produces transient reductions in fault normal stress, has been proposed as a mechanism for reducing shear resistance during earthquake slip [*Melosh*, 1996].

Here we experimentally explore the behavior of a sheared granular medium when the shearing itself generates acoustic vibration. Our starting point is a recent experiment that showed that the thickness of a steady, shear-driven flow is non-monotonic with respect to shear velocity [*Lu et al*., 2007]. At velocities intermediate between quasi-static and grain-inertial flow (the transitional regime, Fig 3-1c), steady-state thickness of the shear zone is markedly reduced. Under constant volume conditions, this thinning manifests as a drop in shear strength and normal pressure. This behavior is not anticipated by theoretical treatments of granular flow, which predict monotonic dilation with shear rate [*Bagnold*, 1954; *Campbell*, 1990; 2006; *Clement*, 1999] nor by experiments carried out at lower shear rates and higher pressures [*Marone et al*., 1990; *Marone*, 1991]. Numerical experiments using idealized particles also fail to

anticipate this transitional compaction [*da Cruz et al*., 2005; GDR MiDi, 2004]. The non-monotonic behavior at intermediate shear rates has recently been confirmed in several independent experiments [*Dijksman et al*., 2011; *Kuwano and Takahiro*, 2011]. This phenomenon is much more pronounced for highly angular particles than for smooth particles.

We propose in this paper that the intermediate shear-rate thinning observed in prior experiments can be explained as auto-acoustic compaction; at moderate shear rates, grain interactions generate acoustic vibration that causes compaction and suppression of shear-induced dilatation. The tradeoff between shear dilatation and shear-induced acoustic compaction results in a shear-rate dependent steady-state thickness of the shear zone. The competition between vibrational compaction and shear dilation we propose is reminiscent of the crystallization/melting transition described by Daniels and Behringer [2005], in which vibration is interpreted to weaken force chains and reduce the internal granular pressure.

To resolve this problem, we first reproduce the observations of Lu et al., [2007], measuring the steady-state thickness of a sheared granular medium over a range of shear rates. We record the amplitude of acoustic emissions produced during shear, and then apply similar amplitudes of acoustic vibration using an external vibration transducer and observe the effect on steady-state shear zone thickness. We also perform experiments in which we subject the shear zone to either transient acoustic

pulses or transient shear-rate steps. We find that external acoustic vibration reduces the steady-state thickness of the shear zone in the same way as shear-generated vibration. Using the time-dependent evolution of shear dilatation and acoustic compaction, we then formulate a quantitative model for steady-state layer thickness. The experiments are performed at low normal stress (7 kPa), so as a last step we develop a scaling law for predicting behavior at higher stresses.

3-2. Methods

In this section we introduce the experimental apparatus, discuss the boundary conditions and normal force control, and describe the acoustic monitoring and external vibration setup. We also describe the granular media, and introduce the basic types of experiment to be performed. The experimental procedures will be described in more detail in Section 3-3 as we go through the results.

3-2.1 Experimental apparatus

The experimental apparatus is a TA Instruments AR2000ex commercial torsional rheometer with rotating parallel plate geometry (Fig. 3-2). This instrument is capable of sensitive measurement and control of torque, angular velocity, and layer thickness, and covers a large range of velocities ($\sim 10^{-5}$ to 300 rad/s), but is limited in the magnitude of the applied forces (50 N normal force, 0.2 N-m torque). This is nearly identical to the instrument used in Lu et al. [2007] and Kuwano and Takahiro [2011].

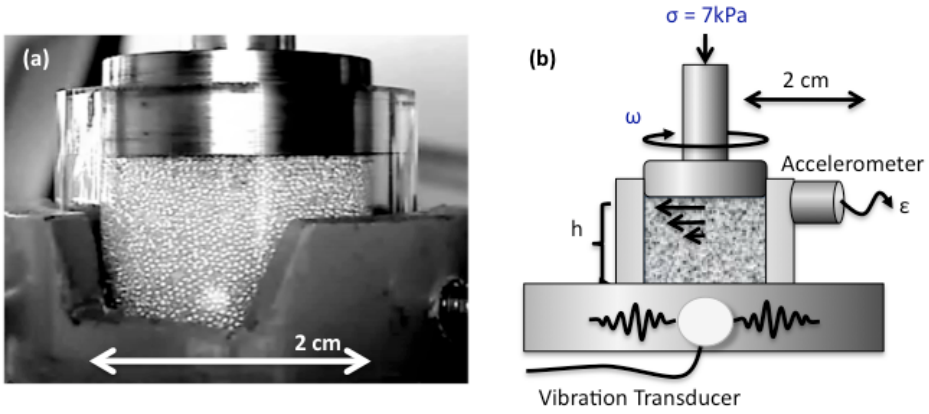

Figure 3-2. Experimental apparatus: TA Instruments AR2000ex torsional rheometer, with parallel plate geometry. **(a)** Photograph of test chamber in mounting bracket. The 2 cm quartz jacket is here filled with glass beads. **(b)** Schematic of the experimental geometry. Shear rate ω and normal stress σ are controlled through the upper rotor. The normal stress σ is held constant at 7kPa by adjusting the rotor height h. We also measure, but do not report on, the torque τ (i.e. shear stress) required to shear at a given velocity.

Torque, sample thickness, normal force, shear rate, and displacement are all measured by the rheometer electronics. Torque is measured to within 1 nN-m through the current required to drive the rheometer magnetic drag cup. Angular displacement is measured to within 40 nRad by an optical encoder on the rheometer spindle. Rotor height (sample thickness) is controlled by a ball slide screw and measured to within 0.1 μm by an optical encoder on the screw motor. Normal force is measured to 1 mN by a force transducer in the base of the sample mount. The maximum sampling rate permitted by the AR Instrument Control data logger is 1 Hz. The experiments are conducted at room temperature and humidity.

The granular sample is housed in a quartz glass cylindrical jacket with dimensions 19 mm diameter by 15 mm height (Fig. 3-2). A layer of particles is epoxied to the base of the chamber and to the upper rotor, to force internal shear rather than slip at the boundaries. The quartz cylinder is filled only to 10 - 14 mm depth, so that the rotor plate is jacketed as well. Friction between the rotor and the quartz jacket is minimized by carefully centering the sample. The residual torque is typically 50 – 300 μNm, or 0.6 – 3% of the average total torque during sample deformation. While a study of the normal and shear stresses would require a correction for jacket friction, we are primarily interested in the steady-state sample thickness, and the residual friction between the rotor and jacket is relatively unimportant.

3-2.2 Controlled stress boundary conditions and relation to controlled volume

All experiments are carried out under controlled normal stress conditions (7 kPa). This low normal stress minimizes grain fracture and emphasizes the effect of grain interlocking, rolling, and sliding in shear deformation. The possible limitations of using such a low normal stress are taken up in the discussion at the end of the paper.

Normal stress is maintained by the rheometer controller software through adjustment of the sample thickness. The normal stress control has a somewhat slow feedback timescale, however, resulting in normal stress fluctuations in response to sudden dilation or compaction (Appendix 3-B). Furthermore, the controller software only adjusts sample thickness in response to normal force fluctuations exceeding 10% of

the target value. These two features tend to damp out small, rapid fluctuations, which is desirable in some applications, but introduces two difficulties for this study. 1) The finite time response makes it difficult to interpret the intrinsic time scale for sample compaction in response to a sudden acoustic or shear-rate pulse (Appendix 3-B). 2) The 10% minimum fluctuation results in an apparent hysteresis in thickness between ascending and descending velocity ramps that actually reflects a hysteresis in the average imposed normal stress. These two caveats must be kept in mind when interpreting the second-order features of the data presented in this study.

We employ constant normal stress rather than constant volume boundary conditions because the large variations in shear zone thickness would otherwise result in either decoupling of the sample during compaction phases, or locking up of the mechanical drive during dilatation. However, qualitatively similar results are obtained when measuring the evolution of normal stress under constant volume conditions [*Lu et al*., 2007; 2008].

Following the argument of Lu et al, [2007], the correspondence between normal stress and layer thickness for alternate boundary conditions is a consequence of the cyclic rule, which states the relationship between the partial derivatives of a three-variable constitutive law

$$\left(\frac{\partial V}{\partial \dot{\gamma}}\right)_{\sigma} = -\left(\frac{\partial V}{\partial \sigma}\right)_{\dot{\gamma}}\left(\frac{\partial \sigma}{\partial \dot{\gamma}}\right)_{V}. \quad (3\text{-}3)$$

The change in volume V (or layer thickness) with shear rate $\dot{\gamma}$ at constant load is related to the change in stress σ with shear rate at constant volume through the compressibility term $(\partial V/\partial\sigma)_{\dot{\gamma}}$. The compressibility term may be quite complicated for a granular flow [*Daniels and Behringer*, 2005], but assuming it exists and is negative, layer compaction under constant load implies normal stress reduction under constant volume.

3-2.3 Acoustic Vibration

External acoustic vibration is produced by a ceramic transducer (PZT-5) affixed to the base plate of the rheometer adjacent to the sample chamber. An accelerometer (Bruel and Kjaer 4373 charge accelerometer), attached directly to the cylindrical jacket outside the active shear zone, measures the acoustic vibration intensity. In order to achieve high acoustic strain amplitude with a small source transducer, we vibrate at the resonant frequency of the mechanical system, i.e., the frequency that produces the largest measured peak amplitudes in the accelerometer, which is found to be 40.2 kHz. Note that this is the natural frequency of the entire apparatus, not necessarily the sample chamber itself, which has a fundamental frequency between 28 and 34 kHz based on the acoustic wave speed found below.

We measure peak acceleration, but express acoustic intensity in terms of peak strain. Peak acceleration is measured over 1-second intervals, and then averaged over the duration of each 20-second velocity step. Peak acoustic strain ε is then estimated by

dividing the peak acceleration a by the dominant frequency of the vibration (f = 40.2 kHz) to get particle velocity, and then dividing by the acoustic wave speed c

$$\varepsilon \approx \frac{a}{2\pi fc} \approx \frac{v}{c}. \qquad (3\text{-}4)$$

The acoustic wave speed for a solid is given by

$$c = \sqrt{\frac{2G(1-\nu)}{\rho(1-2\nu)}}, \qquad (3\text{-}5)$$

where ρ is density, G is the shear modulus, and ν is Poisson's ratio. The shear modulus of our sample is 1.1×10^8 Pa, as measured by an oscillatory strain test with frequency 100 Hz. The sample density is 1500 kg/m^3. Assuming a Poisson's ratio between 0 and 0.25, this gives an acoustic wave speed c between 390 and 480 m/s. This agrees well with other experiments on acoustic travel time in granular media, extrapolated to slightly lower pressures [*Coghill and Giang*, 2011; *Jia et al*., 1999], as well as with theoretical predictions using effective medium theory [*Makse et al*., 2004; *Walton*, 1987].

The acoustic vibration frequency (40.2 Hz) is therefore slightly higher than the natural frequency of the sample (~30 kHz), but much lower than the natural frequency of a single grain (~MHz). The accelerometer has a flat response up to 35 kHz and detailed analysis of the shear-generated acoustic spectrum and the frequency dependence of the rheological response are beyond the scope of this study. We note, however, that recent preliminary tests using a more powerful amplifier to generate

equivalent strains with lower frequencies (down to 1kHz) show qualitatively similar results.

3-2.4 Granular Media

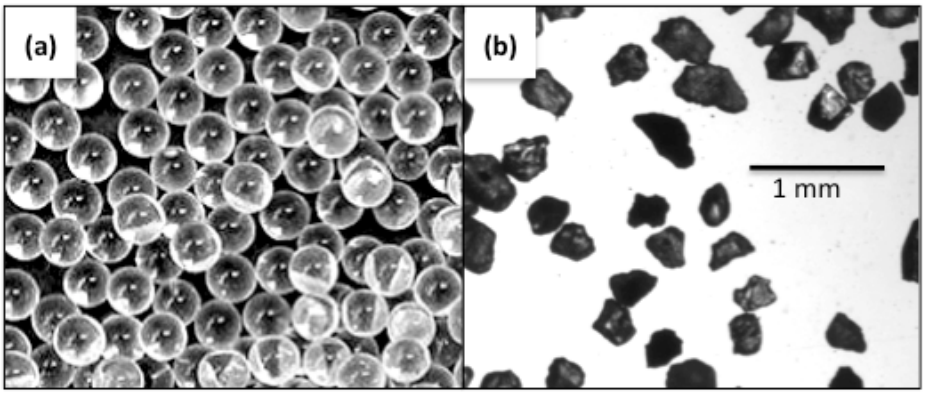

Figure 3-3. Granular media used in shear experiments: **a)** smooth soda-lime glass beads, **b)** angular Santa Cruz beach sand.

We test two different granular materials with different grain shapes (Fig. 3-3), but equivalent sizes and densities: spherical glass beads (soda-lime glass sandblasting beads, (mono-disperse, mean diameter: 350 μm) and angular beach sand (from Cowell's Beach in Santa Cruz) (range: 250-500 μm, uniformly distributed; mean: 350 μm). The beach sand is chosen for its high angularity and high fracture resistance. The composition of the sand is roughly 44% quartz, 37% lithics, and 19% feldspars [*Paull et al*., 2005]. The composition of the heavy minerals and lithic fragments is detailed by Hutton [1959].

3-2.5 Experimental Procedures

3-2.5.1: Velocity ramps

The primary experiment consists of a suite of angular velocity ramps between 10^{-3} to 100 rad/s (9.5×10^{-4} to 95 cm/s at the outer rim of the rotor) under controlled normal stress, in which we report sample thickness (Section 3-3.1, 3-3.3). The velocity is incremented gradually from slow to fast and fast to slow, multiple times per sample. The repeated velocity ramps extend the work of Lu et al. [2007], who focused mostly on a single velocity ramp per sample. Each velocity step lasts 20 seconds, and the reported thickness is averaged over the last 10 seconds of each step. The duration of the steps is chosen to allow the shear zone to evolve to a new steady-state thickness value after each small step in velocity. We refer to these thickness observations as steady-state, in that they do not depend on the direction of the velocity ramp or the duration of the observation. Throughout this paper, we refer to this experimental procedure as a velocity ramp, although in reality it consists of small discrete velocity steps. The velocity ramp experiments are summarized in Table 3-1.

We first run the velocity ramps in the absence of acoustic vibration to establish the baseline, steady-state thickness of the shear zone as a function of shear rate. During these experiments, we record the shear-rate dependent amplitude of acoustic vibration produced internally by grain interactions. We then perform velocity ramps in the presence of constant amplitude external vibration and examine the effect on steady-state thickness.

Table 3-1. Velocity ramp experiments

Name	Material	runs w/o vibration[a]	runs w/ vibration[a]	correction[b]
VRS1	Sand	4 (2,2)	8 (4,4)	yes
VRS2	Sand	2 (1,1)	8 (4,4)	No
VRS3[c]	Sand	10 (5,5)	6 (3,3)	No
VRS4	Sand	0	8 (4,4)	No
VRG1	Glass beads	17 (9,8)	6 (3,3)	No

[a] (*N*,*M*) signifies *N* slow-to-fast and *M* fast-to-slow velocity ramps, respectively

[b] linear correction for run-in phase applied to runs without vibration

[c] shown in Figure 3-7

3-2.5.2 Acoustic pulses and shear-rate pulses

In the second type of experiment, we subject the sample either to acoustic pulses or transient shear-rate steps (Section 3-3.6, 3-3.7). In the acoustic pulse experiments, we shear the sample at a slow, constant rate of 0.01 rad/s to minimize internally generated vibration and shear dilatation, and then introduce 60-second pulses of acoustic vibration at various amplitudes. In the shear-rate pulse experiments, the sample is sheared at a constant rate of 0.1 rad/s, and then subjected to 60-second jumps in shear rate. The higher baseline shear rate is chosen to minimize the transient effects of the shear-rate jump. The pulse experiments are summarized in Table 3-2.

The amplitude of the shear-induced acoustic vibration is captured by the accelerometer, allowing us to compare the magnitude of compaction under equivalent-amplitude external and shear-induced vibration. We use the information gained from the pulse experiments to explain the steady-state thickness variations in the velocity ramp experiments in Section 3-4.

Table 3-2. Pulse experiments (sand)

Name	Pulse type	Starting shear rate	Pulse shear rate (rad/s)	Acoustic strain	b (μm)[a]	Runs
SPS1	Shear	0.1	1.0	1.3×10^{-5}	1.9 ± 1.9	10
		0.1	2.0	2.2×10^{-5}	5.6 ± 2.7	5
		0.1	3.16	2.9×10^{-5}	10.5 ± 0.6	5
		0.1	5.0	3.5×10^{-5}	14.2 ± 1.2	5
APS1	Acoustic	0.01	n/a	1.3×10^{-6}	0.9 ± 4.6	13
		0.01		3.8×10^{-6}	2.7 ± 3.0	10
		0.01		1.4×10^{-5}	0.1 ± 3.3	5
		0.01		2.4×10^{-5}	8.6 ± 3.6	5
		0.01		3.0×10^{-5}	9.1 ± 3.3	6

[a] Compaction magnitude (Eq. 3-6) with τ^- held constant at 10 s for all curves

3-3. Results

3-3.1. Velocity ramps – shear induced dilatation and compaction

The velocity ramp produces two effects: 1) long term compaction of the granular sample that goes with total displacement, and 2) reversible and repeatable shear-rate dependent fluctuations about this long-term compaction trend (Figure 3-4a). The long-term trend is irreversible and diminishes with the logarithm of displacement. This irreversible compaction is interpreted as compaction in the non-shearing bulk of the granular sample [*Chambon et al*., 2006a]. The reversible shear-rate dependent features, on the other hand, do not diminish in amplitude with displacement. In the following, we focus almost exclusively on describing the reversible and repeatable component of compaction, which we interpret as reflecting thickness changes in the

actively shearing layer (see Appendix 3-A for a definition of the actively shearing layer). We typically report the velocity ramp data only after the irreversible long-term compaction is complete, treating the first ~10^4 radians displacement as a prolonged 'run-in' phase, but in one case we resort to making a correction for the tail end of the run-in phase (noted in Table 3-1).

The reversible variation of sample thickness with shear rate is shown in Figure 3-4b. The velocity ramp curves in this figure are taken from several experiments using separately prepared samples, after ~10^4 radians run-in displacement (Table 3-1). Both angular sand and smooth glass beads deform with a thickness that is independent of shear-rate at very low shear rates (10^{-3} - 10^{-1} rad/s), and show strong dilation at very high shear rates (>10 rad/s). However, the behavior of the two granular media differs greatly at intermediate shear rates (0.1-7 rad/s), where the thickness of the angular sand decreases markedly. The glass beads show only a hint of this thinning at intermediate shear-rates. The sample thickness follows the same path with respect to shear rate, regardless of whether the shear rate is increasing or decreasing, although there is a slight hysteresis at high shear rates, which we attribute to the normal force control algorithm (see Section 3-2.2).

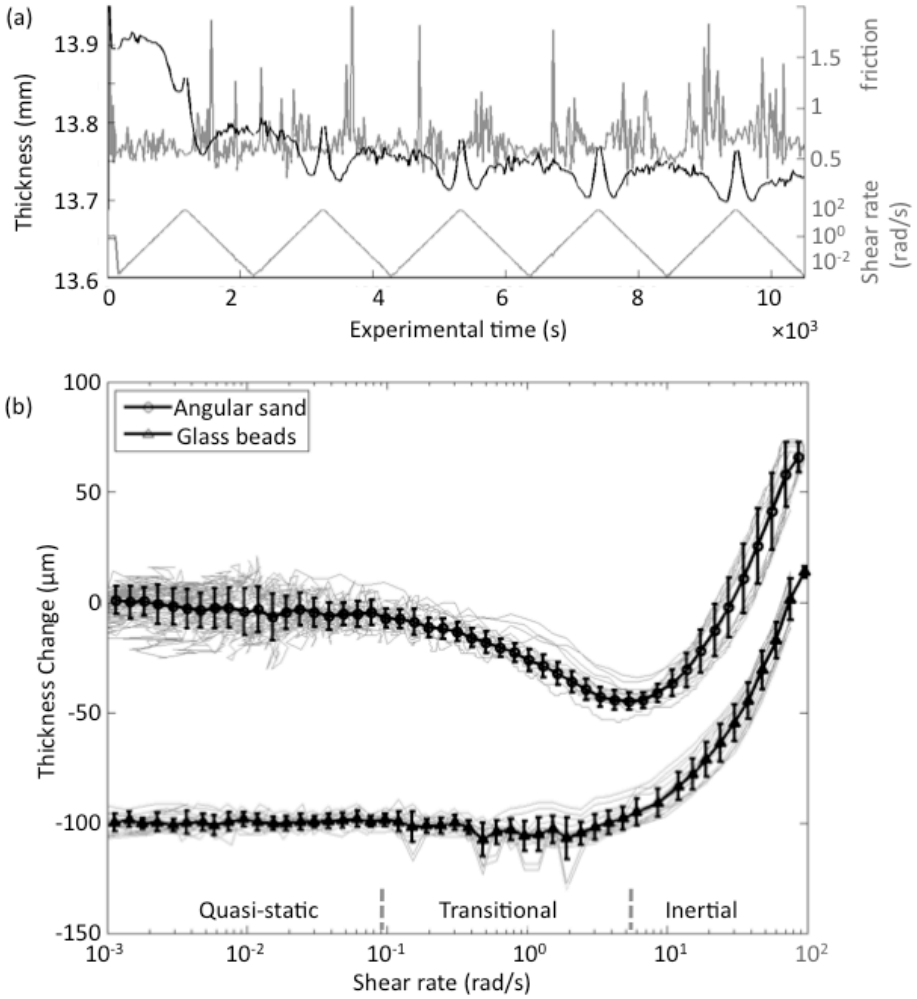

Figure 3-4. (a) Thickness vs. experimental time for the run-in phase of the experiment with angular sand. Sample thickness decreases logarithmically with displacement, with the shear-rate dependent reversible thickness component (b) superimposed. Friction shows strong fluctuations, particularly at intermediate shear rates. **(b)** Steady-state thickness vs. shear rate for angular sand and glass beads. Individual curves represent multiple up-going and down-going velocity ramps (Table 3-1), and thick error bars show means and standard deviations between runs. Thickness is independent of shear rate at low shear rates, and strongly dependent on shear rate for intermediate and high shear rates. Compaction is observed at intermediate shear rates for angular sand, but not for smooth glass beads. Thickness is reported relative to starting thickness, offset by 100 microns for the glass beads.

The behavior of the granular media at either end of the velocity range can be understood in terms of the end-members of granular flow (Equation 3-2, Fig. 3-1).

The glass beads show a relatively monotonic transition between the flow regimes, with constant thickness in the quasi-static regime and dilation in the grain inertial regime (Fig. 3-4). Dilation begins at shear rates above ~30 rad/s (cm/s), corresponding to a dispersive pressure ~200 Pa, which is about 3% of the normal pressure p = 7 kPa (Eq. 3-2). Consequently, we never fully reach the inertial regime where stress and thickness should scale as the square of shear rate [*Bagnold*, 1954]

The behavior of the angular sand at intermediate shear rates, however, is more complex than anticipated by either end-member granular flow regime. At intermediate shear rates there is a robust reversible reduction in steady-state layer thickness, reproducing the findings of Lu *et al*., [2007]. This transitional compaction, on the order of 50 μm at maximum, occurs regardless of the direction of the velocity ramp. The active shear zone thickness is on the order of a few grains, with a scale depth of ~600 μm (Appendix 3-A), putting the maximum compaction at ~10% of the shear zone thickness. This transitional behavior has recently been confirmed in independent experiments [*Dijksman et al*., 2011; *Kuwano and Takahiro*, 2011], but a physical understanding of the transitional regime has yet to be developed.

3-3.2 Probing reversible and irreversible compaction at alternating shear rates

To more clearly demonstrate the relationship between the reversible, shear-rate dependent component and the irreversible run-in phase (Fig. 3-4a), we run an additional experiment using alternating shear rates rather than a continuous velocity

ramp. (Note, that we have not yet arrived at the shear-rate pulse experiments described in Section 3-2.5.2). Starting from zero displacement we impose steady shear, alternating between 1 and 10 rad/s at intervals of 600 radians (Fig. 3-5). These shear rates are well within the transitional shear thinning regime. The difference in steady-state thickness between these two shear rates in the velocity ramp is 12.5 μm (Fig. 3-4).

Viewed over the long term, both shear rates produce logarithmic compaction at a rate that is proportional to shear rate, and hence scales with displacement (Fig. 3-5). Increases in shear rate produce decreases in thickness that are superimposed on the irreversible long-term trend. The reversible thickness difference is 12.5 μm, exactly consistent with the velocity ramp experiments (Fig. 3-4). This shear-rate dependent thickness change does not decrease in amplitude as the irreversible component diminishes, again consistent with the velocity ramps.

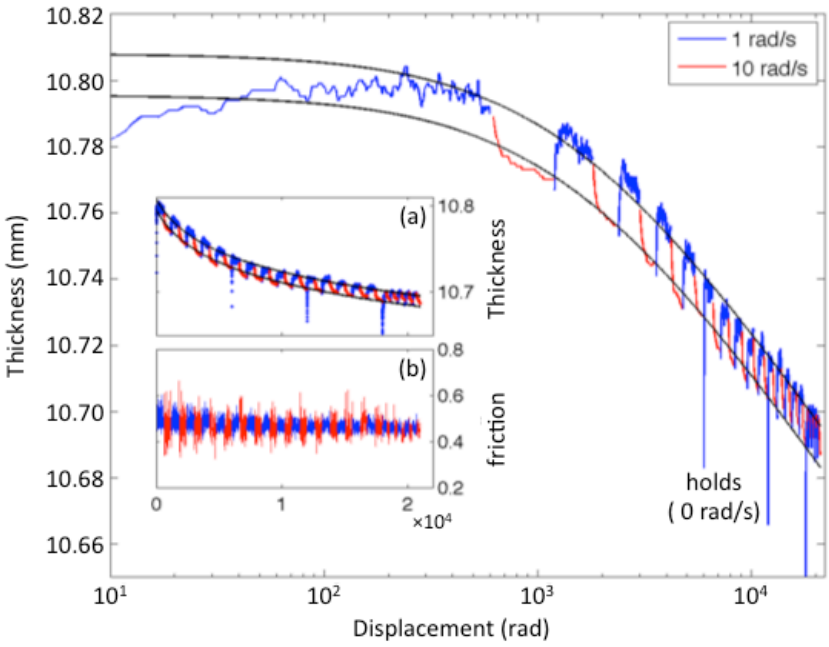

Figure 3-5. Long-displacement steady shear experiment with alternating shear rates (1 and 10 rad/s). Displacement starts from 10 radians to show both the irreversible and reversible components of compaction in the transitional regime. Solid lines are a logarithmic fit to the irreversible component. Three holds in which shear rate and shear stress are set to zero for 60 seconds produce pronounced drops in thickness that are then recovered during renewed shear. Inset **(a)** gives the same data on a linear scale, from 0 radians. Inset **(b)** gives the evolution of friction. Velocity weakening behavior disappears with increasing displacement.

Also shown in Figure 3-5 are three relaxation holds in which the shear rate and torque were set to zero for 60 seconds. These relaxation holds result in ~0.5 mm of immediate compaction that is rapidly recovered upon resumption of shear over a displacement scale of a fraction of a radian. The 1 – 10 rad/s shear-rate steps, on the other hand, evolve over 10's of radians. This highlights that a sheared medium must dilate relative to static packing, and shows that the subsequent evolution of shear-rate

dependent thickness likely involves a reorganization of grains over a displacement scale somewhat larger than for the initial formation and rotation of force chains.

Friction shows weak shear-rate dependence for small cumulative displacement, but this dependence disappears as displacement increases (Fig. 3-5, inset b). Shear-rate independence of friction and thickness may be considered unusual compared to high-stress, low shear rate experiments carried out on crushed granite, in which velocity strengthening and shear-rate dependent dilatation are typically observed [e.g., *Beeler et al*., 1996; *Biegel et al*., 1989; *Marone et al*., 1990]. The difference in thickness behavior may arise from the difference in micromechanics of granular deformation at low confining stress and high porosity, in which shear stresses are supported more through granular interlocking than inter-granular surface friction. On the other hand, we note that most studies show that the velocity dependence of friction in granular materials disappears after significant cumulative displacement (~100 mm) [*Beeler et al*., 1996; *Chambon et al*., 2006b; *Mair and Marone*, 1999]. Since we typically discard the first several velocity ramps to avoid the run-in phase of irreversible compaction (e.g. Figure 3-4a), this amounts to 10^4 radians (95 - 190 meters) of run-in displacement at the rotor rim, putting our experiments well into the range at which little or no velocity dependence of friction is observed in other studies.

The thickness evolution under alternating steady shear rates (Fig. 3-5) is entirely consistent with the behavior in the velocity ramp experiments, demonstrating that the

transitional “dip” in thickness as a function of shear rate (Fig. 3-4) reflects a change in the steady-state thickness of the shear zone, and is not an artifact of the velocity ramp itself.

3-3.3 Velocity ramps with acoustic vibration

In the introduction, we proposed a link between shear-induced vibration and the rheology in the transitional regime. To explore the effect of shear-induced vibration on the reversible compaction observed in section 3-3.1, we now repeat the velocity ramps in the presence of external vibration (Fig. 3-6). The introduction of acoustic vibration has two effects. First, it causes irreversible compaction that decays linearly with log time from the start of the vibration (Fig. 3-7), similar to the irreversible compaction during the run-in phase (Fig. 3-4a), which we discuss below. More importantly, it induces a strong shear-rate dependence in the reversible component at low shear rates that was not seen in the previous experiment (Fig 3-6). At low shear rates, the layer thickness is significantly reduced compared to the non-vibrated case. This effect is seen for the angular sand as well as for the glass beads. The reduced thickness is again a steady-state value, and is reproducible regardless of whether the velocity ramp is increasing or decreasing. The steady-state thickness has a positive slope with shear rate, up to the transitional regime for angular sand. At higher shear rates, there is negligible difference between the experiments with and without external acoustic vibration.

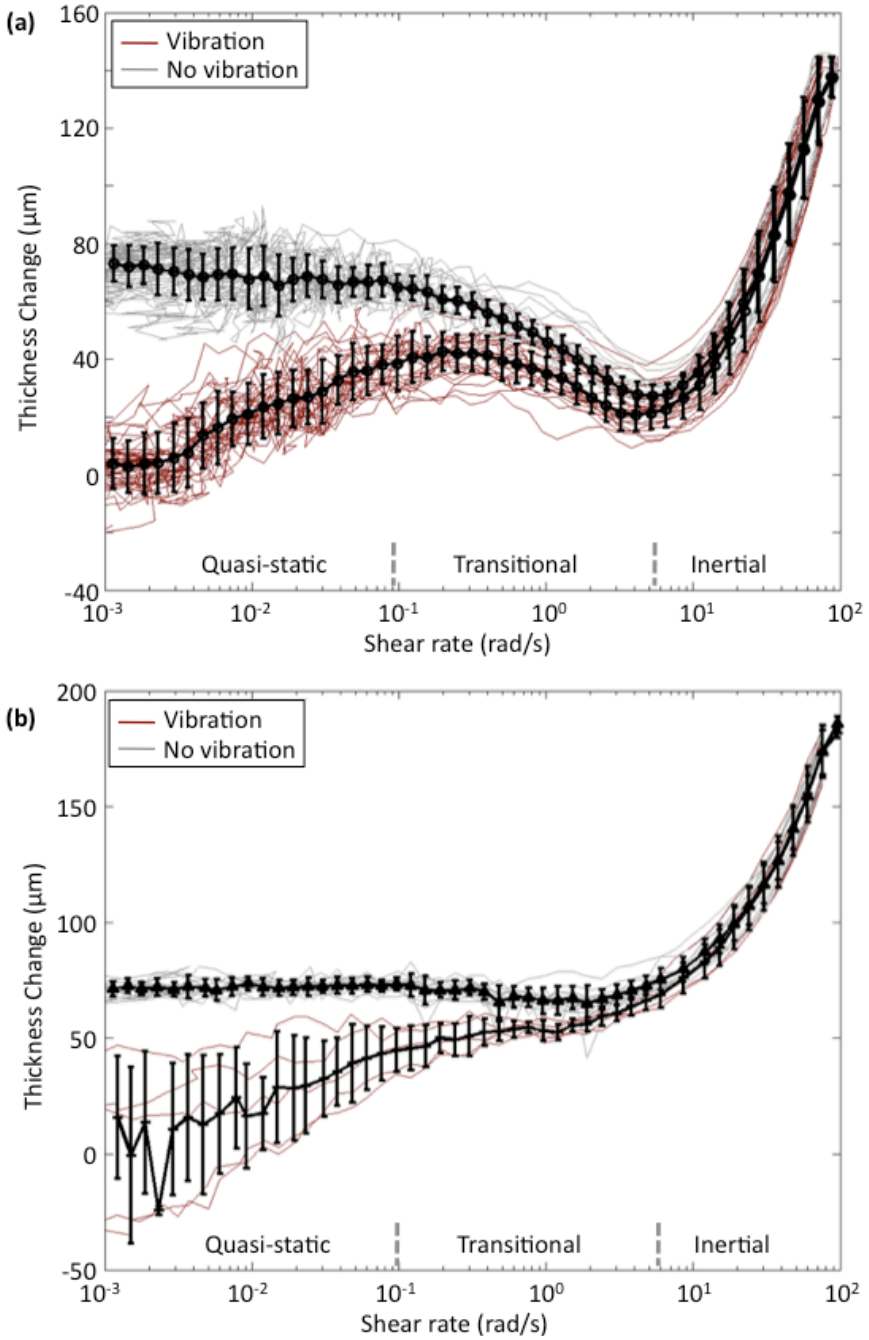

Figure 3-6. Steady state layer thickness as a function of shear rate for **(a)** angular sand and **(b)** smooth glass beads. Layer thickness is given relative to the minimum layer thickness under acoustic vibration. Thin lines are individual runs (Table 3-1); thick lines are averages over all runs. In the presence of acoustic vibration, the layer thickness is reduced and is dependent on shear rate over the entire range. The intermediate shear rate behavior is not strongly affected by the vibration.

A representative acoustic experiment (VRS3, Table 3-1) is shown as a function of experimental time in Figure 3-7, similar to Figure 3-4a. (Note, however, that the data in Figure 3-7 are post run-in, as opposed to in Figure 3-4a.) The angular sand sample is first sheared through several velocity ramps without vibration to establish the baseline shear-rate dependent behavior (Figure 3-7). The non-monotonic pattern of thickness vs. shear rate is traced and then retraced in reverse as velocity is varied over experimental time (c.f. Figure 3-6a). After two complete velocity ramp cycles, the external acoustic vibration is switched on and the sample is run through several more velocity ramp cycles. During the first few cycles with vibration, irreversible compaction occurs, decreasing logarithmically in time (modeled by the thick black line). The new shear-rate dependent thickness variation at low shear rates is superimposed on this irreversible compaction component, and does not change in amplitude from cycle to cycle as the irreversible compaction runs its course. Finally, vibration is switched off and the sample recovers back to its original thickness vs. shear-rate behavior, albeit at a reduced total sample thickness.

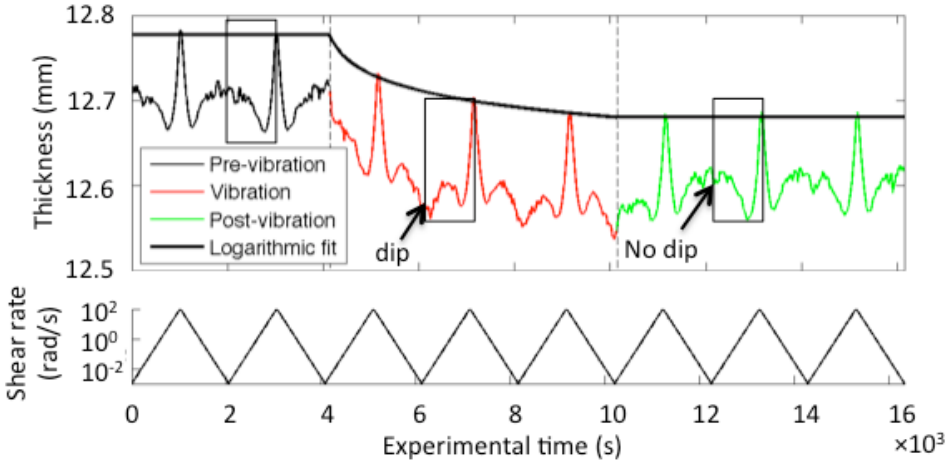

Figure 3-7. Sample thickness and shear rate as a function of experimental time, for angular sand, showing evolution of thickness during external vibration (Experiment VRS3, Table 3-1). Shear rate is ramped up and down **(b)**, producing repeatable and reversible changes in sample thickness **(a)**. Boxes highlight individual slow-to-fast velocity ramps (c.f. Fig. 3-6a). External acoustic vibration is applied at ~4000 seconds, resulting in logarithmic irreversible compaction, and a qualitative change in the reversible thickness at low velocity (labeled 'dip'). Vibration ceases at ~10,000 seconds, after which the low shear-rate compaction returns to the pre-vibration behavior ('no dip').

3-3.4 Linking compaction and acoustic vibration

Acoustic emissions are continuously produced during shear by sliding, jostling, and perhaps occasional fracturing at grain corners, although no visible quantity of fines is observed post-experiment. The accelerometer monitors these acoustic emissions, as well as the amplitude of the vibration produced by the external transducer. The observed vibration links the compaction of the angular sand in the transitional regime and the compaction achieved by external acoustic vibration (Fig. 3-8). First, the

beginning of the transitional regime for angular sand corresponds to the shear rate at which internally produced acoustic vibration becomes detectable. The vibration amplitude for glass beads is smaller at this shear rate, consistent with the much smaller transitional compaction (Fig. 3-6). Second, at high shear rates, the internally generated vibration overwhelms the external vibration such that there is no difference in the recorded vibration amplitude with or without external vibration (Fig. 3-8). This corresponds to the joining of the thickness vs. velocity curves from the two velocity ramp experiments at ~7 rad/s (Fig. 3-6). These observations suggest that acoustic vibration produces compaction in a similar way regardless of whether the vibration is externally or internally generated.

The rollover in acoustic amplitude observed at higher shear rates (Fig. 3-8) is due to the fact that the recorded peak amplitude begins to clip at higher shear rates. To get a more robust estimate of the scaling of vibration amplitude with shear rate, we also compute the signal power of the shear-induced vibration signal for angular sand (Fig. 3-8 inset). Power is computed by integrating periodograms over a pass band between 1 and 35 kHz, and normalized by the maximum value measured at 100 rad/s. This pass band avoids instrument and electronic noise at low frequencies and resonance peaks at higher frequencies (where the amplitude clips). Shear-induced acoustic power increases approximately linearly with shear rate. We will see in a subsequent section that the compaction magnitude also increases linearly with shear rate, indicating a correlation between acoustic power and compaction.

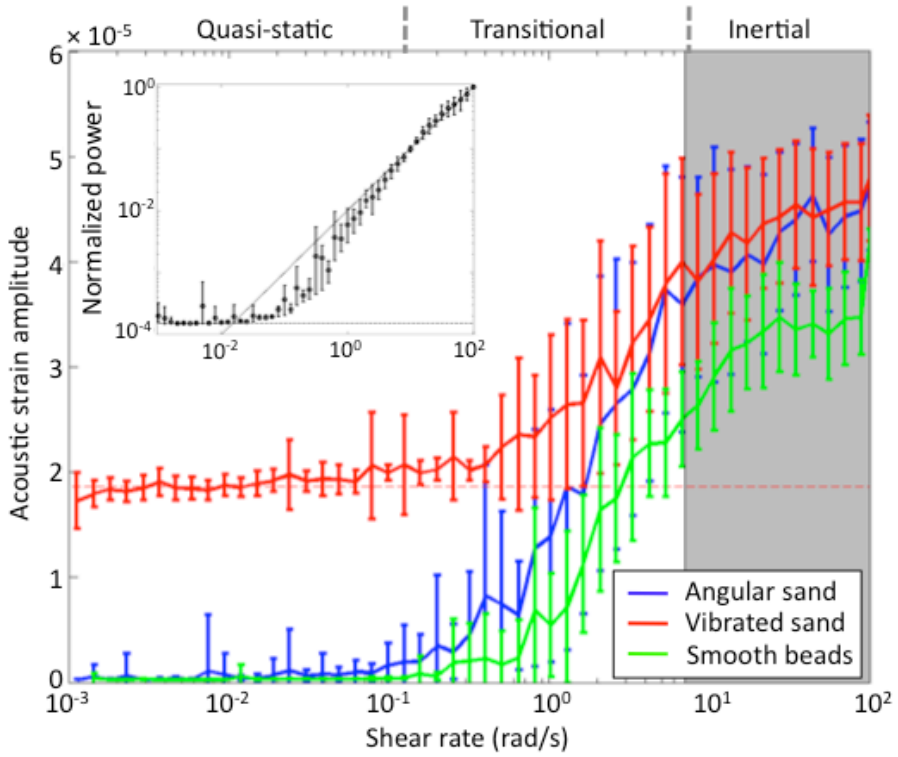

Figure 3-8. Acoustic vibration amplitude, recorded by an accelerometer attached to the sample jacket. Transitions in steady-state thickness (see Figure 3-6) correspond to transitions in the amplitude of shear-induced vibration. The blue curve is vibration produced by shearing angular sand; the green curve is the vibration produced by glass beads. The red curve shows the superposition of external acoustic vibration on shear-induced vibration produced by angular sand. The accelerometer begins to clip at a shear rate of ~7 rad/s (grey patch), so the rollover is not entirely physical. At 1 rad/s the shear-induced vibration is equivalent to the external vibration amplitude (dashed red line for reference). **Inset:** Power of the shear-induced acoustic vibration signal, normalized to the maximum power. Power increases linearly with shear rate (straight line for reference). Error bars show the standard deviation between experimental runs.

3-3.5 A qualitative model for shear zone thickness

These observations suggest a qualitative model for the steady state thickness of a sheared layer in the presence of acoustic vibration. Both acoustic vibration and shear

displacement provide external energy and drive the system to explore packing densities, but in opposite directions and with different timescales. Acoustic vibration produces compaction in the shear zone at a rate that scales with dilation beyond some preferred thickness (perhaps corresponding to random close packing), while shear deformation continually renews contacts and re-dilates the sample at a rate that scales with compaction below some critical state. At some thickness, these two mechanisms are balanced, and a steady state thickness is reached.

These ingredients qualitatively explain the shear-rate dependent behavior seen in the velocity ramps with external vibration (Fig. 3-6). At low shear rates, dilatation is slow, and acoustic compaction has a relatively long time period over which to operate. At somewhat higher shear rates, dilation becomes more rapid, and steady-state compaction is reduced, i.e. the thickness vs. shear rate curve has a positive slope. At even higher shear rates (i.e., the transitional regime), additional acoustic energy is produced by the shearing itself (Fig. 3-8), driving additional acoustic compaction and producing a negative slope in thickness vs. shear rate (Fig. 3-6). This is most pronounced for angular sand grains, which generate high amplitude acoustic vibrations during shear, but is also noticeable for the quieter smooth glass beads. Eventually, grain inertial effects dominate the dilatation, the slope of thickness vs. shear rate becomes strongly positive, and shear dilatancy and acoustic compaction become irrelevant.

This model also explains the existence of the irreversible component of compaction (e.g. Fig. 3-5). Compaction occurs both in the shear zone and in the slowly- or non-deforming bulk far from the shear zone. However, only the compaction that occurs within the shear zone itself can be reversed by shear dilatation.

To develop a more quantitative model of the steady-state shear zone thickness, we now investigate the time dependent evolution of thickness in the presence of pulses of externally applied acoustic vibration or internally generated shear-induced vibration. This will constrain the rate of acoustic compaction for a given amplitude vibration. Combined with a measurement of the rate of shear dilatation, a prediction can be made for the steady-state thickness as a function of shear rate.

3-3.6 Acoustic pulse experiments

In the externally applied vibration pulse experiments, the angular sand is sheared at a constant 0.01 rad/s and subjected to 60-second bursts of acoustic vibration, after which it is allowed to recover for 3 to 10 minutes. The bursts are repeated 5-10 times for each acoustic amplitude in order to establish repeatability. The acoustic pulse experiments are summarized in Table 3-2. The pulses of acoustic vibration produce compaction in the angular sand that increases with the amplitude of the pulse (Fig. 3-9). After cessation of the acoustic burst, the sample recovers a significant component of the thickness that was lost during the acoustic burst, although some of the compaction is irreversible for the highest amplitude pulses. The timescale for re-

dilation is greater than 100 seconds, but is difficult to measure given the natural fluctuations in sample thickness around steady state that occur on this timescale. We interpret the irreversible component of compaction as reflecting incomplete run-in (see Section 3-3.1).

The evolution of thickness h during the acoustic bursts is fit with a logarithmic function of time t

$$h(t) = h_0 - b\log\left(\frac{t}{\tau^-} + 1\right), \quad (3\text{-}6)$$

where h_0 is the starting thickness, and b and τ^- are empirical constants that describe the magnitude and timescale of compaction, respectively. This function is motivated by other work where the density (i.e. inverse of volume) of a vibrated granular medium is observed to evolve as ~1/log(t) [*Ben-Naim et al.*, 1998; *Caglioti et al.*, 1997; *Knight et al.*, 1995], however other functions (e.g. stretched exponential, double exponential) may fit the data just as well. In this study, we are primarily interested in whether some function that describes the evolution of thickness with time can also predict the steady-state observations as a function of shear rate, and a theoretical treatment of the micromechanics of acoustic compaction are beyond the scope of this experimental work.

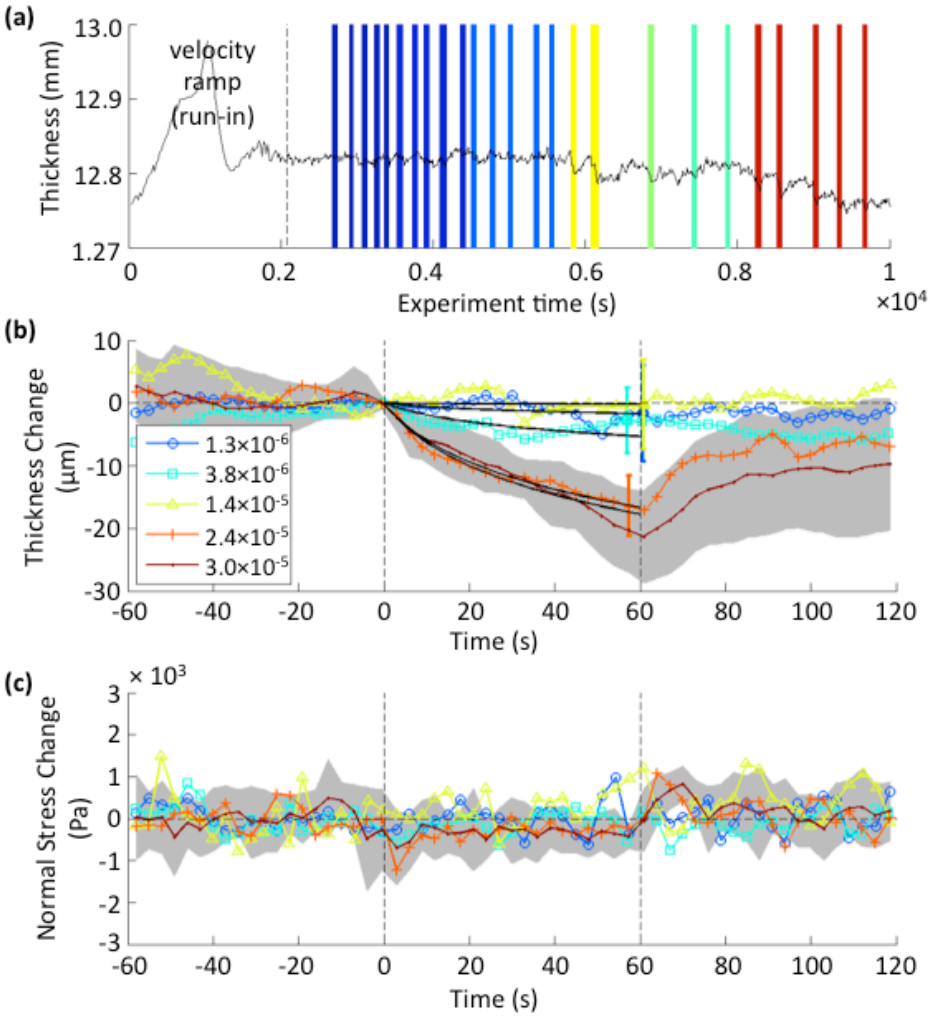

Figure 3-9. Thickness response of a steadily sheared granular medium subjected to transient acoustic pulses. **(a)** Thickness vs. time for the first 10^4 seconds of the experiment. A velocity ramp is performed to run the sample in over the first 2000 seconds. The sample is then sheared at 0.01 rad/s and subjected to 60-second acoustic pulses (colored bars, corresponding to amplitude (key in (b)). **(b)** Stacked thickness response relative to starting thickness for different amplitudes. Black lines are model fits (Eq. 3-6). Grey patch shows one standard deviation between curves in the highest amplitude stack, and are representative of variations in the other stacks. Final thickness variations for the other stacks are shown by error bars at 60 seconds. **(c)** stacked normal stress response.

We could attempt to fit the curves for each vibration amplitude individually, treating both b and τ^- as unknowns. However, there is considerable tradeoff between the two parameters. We choose instead to fix $\tau^- = 10$ s, which produces a good fit to all the curves (including the shear-rate pulse curves in the following section), and fit only the constant b (Table 3-2). This allows us to map all of the variation with amplitude into a single constant. We justify this choice by noting that while it is possible to fit the curves with a single value of τ^- and varying b, it is not possible to fit the curves with a single value of b and varying τ^-. This implies that the magnitude of compaction is strongly dependent on vibration amplitude, but the timescale is not.

For the highest amplitude vibration, the acoustic compaction produces a very small rapid drop in the normal stress, before the rheometer recovers by lowering the upper plate (Fig. 3-9c). This reflects the fundamental relationship between sample thickness and stress in these experiments (Eq. 3-3). It also shows that the rheometer is unable to keep up with the compaction rate (Appendix 3-B), and the time scale τ^- that we measure in the pulse experiment cannot be taken as a reliable estimate of the intrinsic compaction time scale. We note that the normal stress drop occurs on the timescale of about 1 second. We will eventually solve for the true compaction timescale by fitting a model to the steady-state velocity ramp experiments. This effect is relatively negligible for the small-amplitude external vibration experiments, but will be considerably larger for the shear-rate pulses examined in the next section.

The key observations to come out of the acoustic pulse experiments are the logarithmic (or at least, long-tailed) compaction, and the scaling of compaction magnitude parameter *b* with vibration amplitude.

3.7 Shear rate pulses

We now measure compaction during shear rate pulses (Fig. 3-10). We shear the sample at a starting rate of 0.1 rad/s – the maximum shear rate before the transitional weakening – to minimize the direct effect of the velocity jump [*Marone et al.,* 1990; *Marone*, 1991]. We then apply high shear-rate pulses of up to 5 rad/s – the maximum shear rate before inertial dilation effects become apparent in Figure 3-4. Each curve in Figure 3-10 represents an average over 5 - 10 runs (Table 3-2). The compaction magnitude is observed to increase with the magnitude of the shear rate pulse. When shear rate is stepped back down to 0.1 rad/s, the sample recovers a significant fraction of the shear-induced compaction over a timescale of a hundred seconds, just as it did after the acoustic pulses. We again interpret the additional irreversible component as reflecting incomplete run-in.

We fit the shear-induced compaction curves with the same function as for the acoustic pulses (Eq. 3-6), again with $\tau^- = 10$ seconds, and again with the caveat that the accuracy of this timescale is limited by the instrument response (Appendix 3-B).

The compaction magnitude parameter b is listed in Table 3-2, along with the amplitude of internal, shear-generated vibration as measured by the accelerometer.

We also fit the thickness evolution in the recovery phase with an exponential function,

$$h(t) = h_0 - \Delta h \exp\left(-\frac{t}{\tau^+}\right), \quad (3\text{-}7)$$

Where h_0 is the steady-state layer thickness after complete recovery (i.e. the critical thickness for shearing in the absence of vibration), Δh is the total drop during the compaction phase, and τ^+ is the timescale for re-dilation. We find an average recovery timescale τ^+ of 55 seconds, corresponding to a displacement scale of 5.5 rad, given the shear rate of 0.1 rad/s. We note that this displacement length scale is much longer than the length scale over which strength is recovered after a complete removal of the driving stress, which tends to be on the order of the grain diameter [*Chambon et al*., 2006a; *Toiya et al*., 2004].

There is strong rapid normal stress drop during the shear-rate jumps due to the slow response of the rheometer (Appendix 3-B), and for the largest amplitudes, the rheometer does not completely catch up to restore the normal force even after 60 seconds (Fig. 3-10). The underlying compaction timescale, as suggested by the rapid normal stress drop, is therefore likely to be much less than the 10 seconds estimated from the thickness curves, and may be as little as 1 second or less.

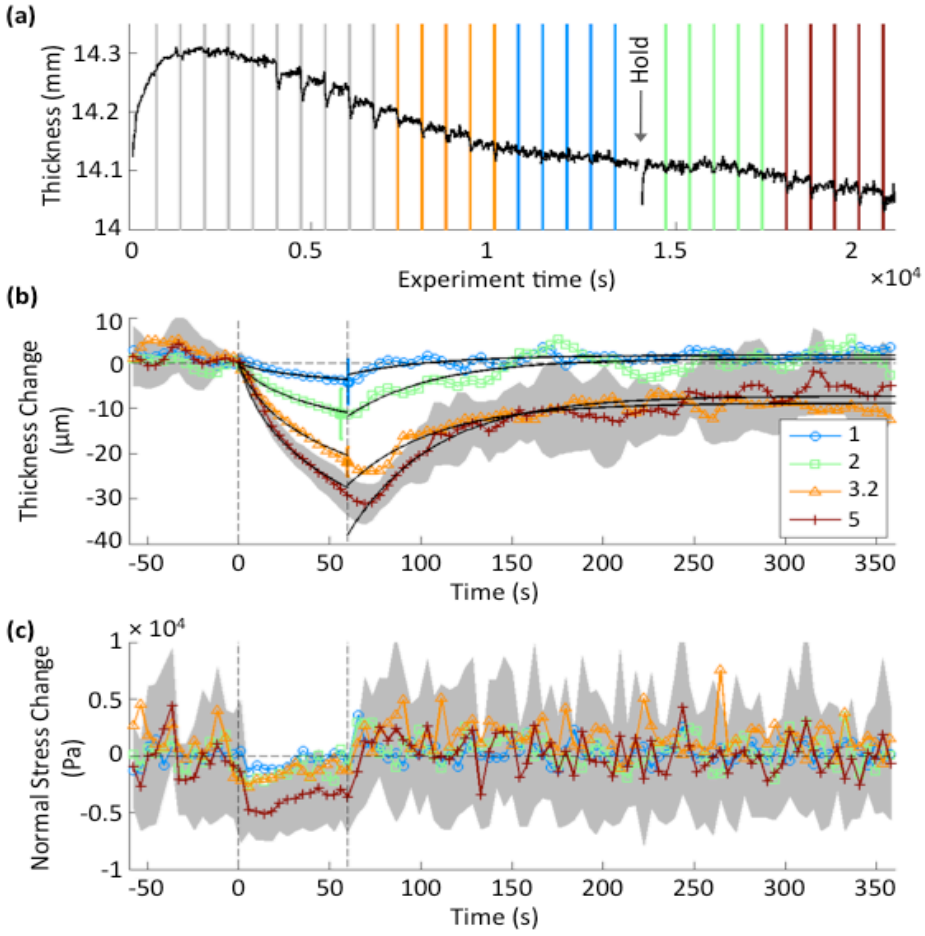

Figure 3-10. Thickness response of a steadily sheared granular medium subjected to transient shear rate pulses. **(a)** Thickness vs. experimental time. The sample is sheared at 0.1 rad/s, and subjected to 60-second acoustic pulses of higher shear rate (colored bars, corresponding to key in (b), units: rad/s). 'Hold' marks a point where shear rate and shear stress were transiently set to zero for a few seconds. **(b)** Stacked thickness response relative to starting thickness for different shear rates. Black lines are model fits (Eqs. 3-6, 3-7). Grey patch shows one standard deviation between curves for the 5 rad/s stack, and are representative of variations in the other stacks. Final thickness variations for the other stacks are shown by error bars at 60 seconds. **(c)** stacked normal stress response.

Comparing the values of compaction magnitude vs. acoustic strain amplitude for both shear and acoustic pulses (from Table 3-2), we find that for both pulse types the compaction magnitude is the same for the same amplitude vibration (Fig. 3-11). This indicates that the acoustic compaction mechanism is activated by vibration in the same way regardless of whether the acoustic energy is generated by grain interactions during shear, or injected from an external source. The recovery of dilatation after the cessation of the pulse shows that the acoustic vibration is causing compaction within the actively shearing layer, essentially suppressing shear dilatation and allowing the grains to shear in a more compact configuration at the same stress.

We infer that the compaction observed in the transitional regime during the velocity ramp experiments (Fig. 3-4) is also the result of internally-generated acoustic vibration that feeds back on the rheology of the medium. The empirical compaction and dilatation functions that we have measured (Eqs. 3-6 and 3-7) now allow us to formulate a quantitative model for the steady-state thickness of a sheared layer that reflects the competition between acoustic compaction and shear dilation.

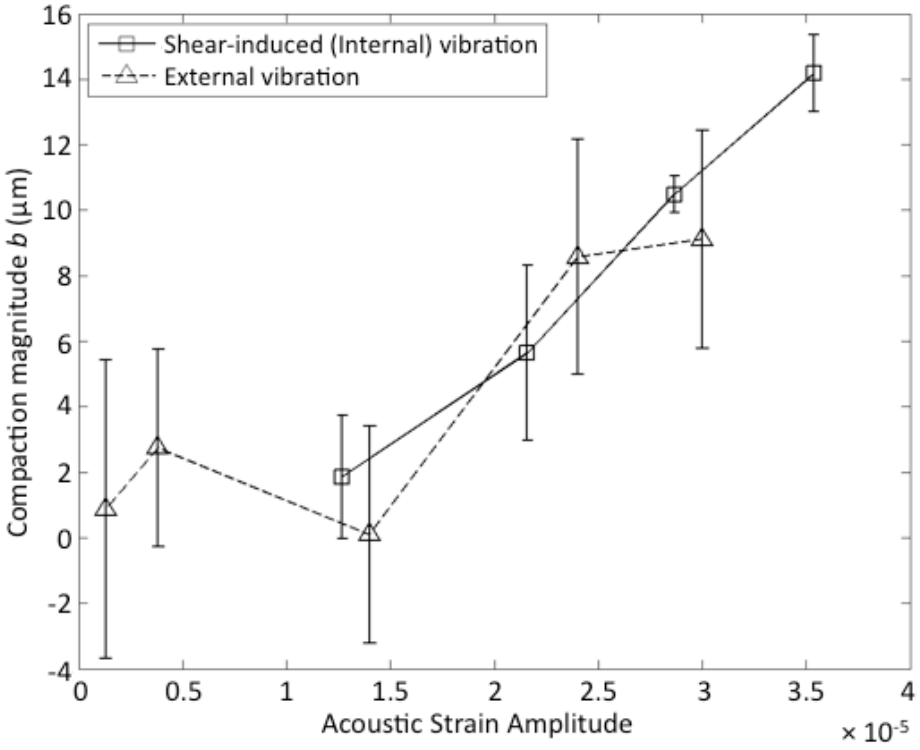

Figure 3-11. Compaction magnitude *b* (Eq. 3-6) is a consistent function of acoustic strain amplitude for external (Table 3-2: Aps1) and internally generated (Table 3-2: Sps1) acoustic vibration. Compaction magnitude increases linearly above a threshold strain amplitude of about 10^{-5}. Triangles show compaction for external vibration, squares correspond internal, shear-generated vibration, for shear rates of 1, 2, 3.2, and 5 rad/s, from left to right. Each point is an average of 5-10 runs (Table 3-2), and error bars show standard deviations between runs. The compaction timescale τ^- is fixed to 10 seconds.

3-4. Discussion

3-4.1 Key components of the steady-state thickness model

Any model that explains all the observations presented in Figure 3-6 must meet at least the following fundamental criteria: 1) At low shear rates, the dilation rate must increase with shear rate in order for external acoustic vibration to produce less steady-

state compaction at higher velocities. 2) In the transitional regime, the shear-induced acoustic compaction rate must increase faster with shear rate than the shear-induced dilation rate, in order to produce the transitional compaction. 3) The external and internally generated acoustic compaction should behave similarly for equivalent amplitude vibrations.

3-4.2 A model for the competition between dilatancy and auto-acoustic compaction

We propose a simple model for steady-state shear zone thickness that invokes a balance between shear-induced dilation and acoustic compaction. The model is based on the empirical curves observed in the vibration pulse experiments, paired with some assumptions to make it consistent with the key components in Section 3-4.1. The model does not address the physical micro-mechanics of shear dilation and acoustic compaction.

The evolution of shear dilation follows an exponential function of time (Eq. 3-7), as observed in the recovery stage of Figure 3-10 after the shear-rate pulse. The evolution of acoustic compaction follows a logarithmic function of time (Eq. 3-6). Taking the derivatives of these Equations (3-6 and 3-7) and adding them together gives a total rate of change

$$\frac{dh}{dt} = \frac{\left(h_0 - h\right)}{\tau^+} - \frac{b}{\tau^-}\exp\left(-\frac{h_0 - h}{b}\right). \quad (3\text{-}8)$$

The first term on the right hand side (RHS) is the dilation term, where τ^+ is the timescale for dilation and h_0 is the steady-state thickness in the absence of vibration or other perturbations. The second term on the RHS is the compaction term, where τ^- is the timescale for compaction and b is the compaction magnitude, which depends on acoustic vibration amplitude. Equation 3-8 is expressed in terms of deviations in thickness h. In reality, the dilation rate likely depends on the packing density, normalized to the minimum and maximum packing densities. Since we are unable to measure the packing density directly in the active shear zone of our sample chamber, we make the first-order approximation that changes in thickness dh are proportional to changes in normalized packing density for small deviations from h_0, and formulate the model as a function of thickness only.

We further assume that τ^+ is inversely proportional to the shear rate ω, to be consistent with key component (1) (Section 3-4.1).

$$\tau^+ = \frac{d}{\omega}, \qquad (3\text{-}9)$$

where d is a characteristic angular displacement length scale for renewal of force chains.

For $h < h_0$ the two terms in the RHS of Equations 3-8 drive thickness changes in opposite directions. The steady state thickness of the shear zone is the thickness h at which the dilation rate (Eq. 3-8) = 0, or

$$\frac{h-h_0}{d}\omega = \frac{b}{\tau^-}\exp\left(\frac{h-h_0}{b}\right), \quad (3\text{-}10)$$

where the parameter b depends on the internally and externally generated vibration amplitude. Note that the steady-state thickness h is defined only in terms of b and the ratio of the two timescales τ^+/τ^- .

3-4.3 Experimental fit

We now return to the steady-state thickness (velocity ramp) experiments (Fig. 3-6), and use Equation 3-10 to solve for b as a function of shear rate. We use the same equation to solve separately for b in the case with and without external vibration, and refer to the fit parameters as b_{acoustic} and b_{shear}, respectively. Table 3-3 summarizes the model parameters.

We fit the acoustic compaction magnitude parameter $b_{acoustic}$ (Eq. 3-10) over the low-velocity range, where shear-induced compaction is negligible (Fig. 3-12). Since the compaction timescale in the pulse experiments is unreliable (Appendix 3-B), we also fit τ^- setting the dilatation recovery length scale d to 5.5 radians, as estimated from the shear-rate pulse experiments. This gives a compaction timescale τ^- = 1 second, consistent with the timescale for the large drop in normal force in acoustic pulse experiments, and a value of b_{acoustic} = 10 μm, consistent with the compaction magnitude from the acoustic pulse experiment using the same amplitude external vibration (3×10^{-5}) (Table 3-2).

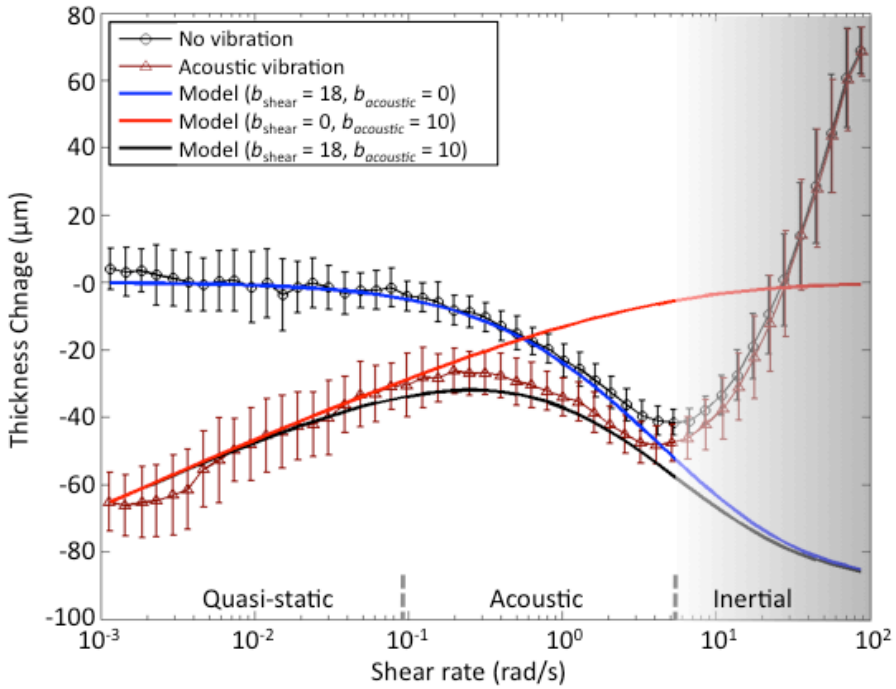

Figure 3-12. Observed and modeled steady-state thickness of the shear zone h as a function of shear rate ω (Eq. 3-10). Observations (with error bars) are the same as in Figure 6a for angular sand under shear-induced and external acoustic vibration. The red curve is the modeled contribution from external vibration only; the blue curve is the modeled contribution from shear-induced vibration; and the black curve shows the modeled sum of the two compaction components. Compaction magnitude parameters are given in the legend. Other parameters are τ^{-} = 1 sec, dilatation length scale d = 5.5 rad (Table 3-3), and starting thickness h_0 = 0. The increase in thickness for both curves at high shear rates is caused by inertial dilation and is not addressed by the model.

Table 3-3: Fit parameters for steady-state thickness model (Eq. 3-10)

$b_{acoustic}$ (µm)[a]	b_{shear} (µm/rad/s)[a]	d (rad)[b]	τ (s)[a]
10	18	5.5	1

[a] fit to combined velocity ramp experiments VRS1-4 (Fig. 12)

[b] fit to acoustic pulse experiment SPS1

The shear-rate dependent steady-state layer thickness at low shear rate is explained quite well by a constant compaction magnitude b_{acoustic} (Fig. 3-12). The systematic relationship between steady-state thickness and shear rate simply reflects the longer timescale for shear dilation at low shear rates (Eq. 3-9). At low shear rates, the acoustic compaction has a relatively long time to operate. As the shear rate increases, less and less compaction can occur within the timescale for dilation.

We fit the shear-induced compaction component b_{shear} with a linear function of shear rate (Fig. 3-12), motivated by the linear increase in shear-induced acoustic power (Fig. 3-7, inset). We fix τ^{-} to 1 second, as found for the external acoustic vibration component at low shear rates. A good fit is obtained with a shear-induced compaction magnitude b_{shear} = 18 μm/(rad/s). A possible interpretation of the linear increase with shear rate would be that each discrete acoustic emission (AE) has a statistically constant amplitude, independent of shear rate, and the rate of AE increases proportional to shear rate. This may imply that AE are produced by an elastic process, such as force chain buckling, as opposed to a collisional process, which should scale as shear rate squared.

The steady-state compaction in the presence of both shear-induced and external acoustic compaction is very nearly predicted by a linear sum between the acoustic and shear-induced compaction components (Fig. 3-12), i.e.

$$b_{total} = b_{acoustic} + \omega b_{shear} \,. \qquad (3\text{-}11)$$

We conclude that the mechanism for acoustic compaction of the actively shearing layer is identical, regardless of whether the vibration is generated internally or externally, and the compaction in the transitional regime is a result of internally generated vibration.

3-4.4 The quasi-static – acoustic transition: a new granular flow regime

In Section 1 we introduced the inertial transition in terms of a balance between inertial dispersive pressure and normal stress (Eqs. 3-1, 3-2). We now discuss the intermediate-rate flow behavior in terms of a new "acoustic" flow regime, where the acoustic pressure balances the normal stress.

The transition to the acoustic regime is observed at shear rates as low as 0.1 rad/s (0.95) mm/s. The inertial dispersive pressure at this velocity is $< 10^{-6}$ times the confining pressure, and the change in rheology cannot readily be attributed to the inertial transition. Instead, this low-velocity transition represents the transition to acoustic fluidization. The acoustic pressure p_a equals the bulk modulus ($K=\rho c^2$) times the acoustic strain ε, giving

$$p_a = \rho c^2 \varepsilon \,, \quad (3\text{-}12)$$

where ρ is the density of the medium, c is the acoustic wave speed [*Thompson*, 1971, chap. 4]. We experimentally identify acoustic compaction at a threshold strain ε on the order of 10^{-5} (Figs. 3-9, 3-11). Taking the acoustic velocity $c \sim 500$ m/s, and $\rho =$

2000 kg/m^3, the threshold acoustic pressure (Eq. 3-12) is 5 kPa, which is on the order of the confining stress (7 kPa). This suggests another non-dimensional number, similar to the inertial number (Eq. 3-2)

$$J \equiv \frac{\rho c^2 \varepsilon}{p}, \qquad (3\text{-}13)$$

The transition from the quasi-static to acoustic granular flow regime occurs when confining pressure p is balanced by acoustic pressure, i.e. $J = 1$. Note that the acoustic approximation becomes invalid as the acoustic pressure fluctuations approach the absolute pressure, i.e. $J \sim 1$, and the acoustic wave speed should decrease dramatically in the fluidized regime, limiting further increases in the acoustic pressure.

Melosh [1979; 1996] suggested that acoustic fluidization could allow granular materials to flow at shear stresses far below the frictional strength suggested by the overburden pressure. In this theory, acoustic pressure fluctuations produce transient reductions of the normal stress, allowing stress to locally exceed the Coulomb frictional threshold. The mechanism is activated when the peaks in acoustic pressure reach the order of the overburden. The energy density to "fluidize" a rock mass by acoustic vibration is orders of magnitude smaller than the energy density required to fluidize the same rock mass by kinetic particle motion [*Melosh*, 1979]. There is some experimental evidence for the importance of acoustic resonances in mobilizing a

granular medium at vibration amplitudes much smaller than required to balance gravitational acceleration [*Umbanhowar and van Hecke*, 2005].

The mechanism we propose here is very similar to the acoustic fluidization of Melosh, but differs in a fundamental way: instead of normal force being reduced directly by acoustic stress fluctuations, it is reduced indirectly through the phenomenon of acoustic compaction. The general conceptual model for acoustic compaction comes out of granular physics [*Mehta*, 2007]. In this framework, shear stress in a granular packing is supported by a framework of force chains, supported by a network of buttressing grains [*Majmudar and Behringer*, 2005]. Increased loading in the shear direction primarily compresses and rotates the strong force chains, which leads to bulk dilatation [*Tordesillas et al.*, 2011]. Particle reconfiguration (compaction) can only occur when strongly loaded force chains buckle catastrophically. When static equilibrium is restored by the formation of new force chains, the packing is again in a jammed state and unable to explore configurations. Acoustic vibration, on the other hand, accesses both strong force chain grains and buttressing grains directly, and may continuously disrupt grain contacts without catastrophic buckling of force chains. This promotes incremental compaction into a lower energy configuration.

Auto-acoustic fluidization, as observed in these experiments, is related to the amplitude of acoustic vibration produced through grain interactions during shear. As

such, it is strongly dependent on the characteristics of the grains. Angular grains generate sufficient acoustic energy to strongly affect the rheology of the flow, but smooth glass beads do not. This implies that the physical characteristics of gouge particles observed in fault zones can tell us something about the rheology of the flow during rupture.

For this mechanism to be active at seismogenic depths of ~10 km, with overburden pressure on the order of 3×10^8 Pa, assuming $c = 3\text{x}10^3$ m/s, and $\rho = 3\text{x}10^3$ kg/m^3, Equation 13 requires that the acoustic strain amplitude ε be on the order of 10^{-2}. It is not known how internally generated acoustic strain amplitude should scale with slip rate at these conditions, and this value is at the upper limit of plausible elastic strain in rock and well into the non-linear elastic regime, where other mechanisms may dominate the rheology [*Johnson and Jia*, 2005]. However, if the effective confining pressure is reduced by fluid pressure or some other mechanism, the required acoustic strain amplitude will be reduced accordingly. There is considerable evidence supporting the idea that effective pressures may indeed be low in many faults [*Hickman et al*., 1995; *Sleep and Blanpied*, 1992].

3-4.5 The acoustic – inertial transition

The acoustic transition described above defines the point at which the active shear zone begins to compact relative to the quasi-static thickness. This compaction grows larger with shear rate until the inertial regime is entered. Following the same recipe as

for Equations 3-1 and 3-13, we define the acoustic-inertial transition as the point at which the dispersive pressure of granular collisions exceeds the acoustic pressure, introducing a third non-dimensional number

$$K \equiv \frac{\rho v^2}{\rho c^2 \varepsilon} = \frac{I}{J}. \qquad (3\text{-}14)$$

The acoustic number J is limited to 1, however, because the acoustic pressure is bounded by the confining pressure. In the acoustic regime, therefore, the non-dimensional number K therefore reduces to the inertial number I. This means that the inertial transition occurs at the same shear rate regardless of whether the transition is from the acoustic or the quasi-static flow regimes. However, the transition from acoustic to dilatational inertial flow begins at a reduced shear zone thickness with respect to the quasi-static regime (i.e. out of the dip in Fig. 3-4).

3-4.6 Future directions

These experiments were carried out at very low confining stresses (7 kPa) and with relatively high porosity in order to isolate deformation by grain rolling, sliding, and force chain reorganization, rather than cataclasis. The low confining stress is also required in order to approach the inertial granular flow regime in our experimental apparatus. This means that elastic deformation of individual grains is relatively small, fragmentation is rare, and there is little contribution to the strength of the material from fine powder in the interstices between large grains. This may not constitute a perfect analogy with deformation in natural fault gouge and other geophysical flows,

however by isolating the mechanisms contributing to porosity creation and reduction at low confining stresses, we can improve our understanding of more complicated systems, including those involving cataclasis. The auto-acoustic compaction mechanism described here should operate in noisy granular flows as long as there is non-zero porosity during shear.

Future experiments must: 1) establish what range of grain characteristics (angularity, aspect ratio, etc.) are capable of generating sufficient acoustic vibration to feed back on the rheology of the shear flow; 2) quantify how the amplitude of acoustic vibration scales with shear rate at seismically relevant confining stresses, as well as under constant volume conditions; and 3) establish the relative importance of acoustic compaction when a range of micromechanical processes are active, including cataclasis, thermal pressurization, and dilatational hardening. On the acoustic compaction side, experiments should explore a range of acoustic pulse amplitudes, frequencies, and durations, with a variety of particle shape and size distributions.

The auto-acoustic compaction model we have proposed in Section 3-4.2 is semi-empirical, and therefore may not be the only possible description of the thickness changes under shear and vibration. A physical model that is tied to the micromechanical processes of dilation and compaction is called for.

3-5. Conclusion

We have experimentally measured the thickness of a granular shear flow over a range of geophysically relevant shear rates. We have quantified the physical conditions for a new granular flow regime at shear rates transitional between quasi-static and inertial granular flow, that we term the acoustic regime. In this regime, internally generated vibrations induce auto-acoustic compaction of the dilated shear zone. The steady-state thickness of the shear zone is described by a semi-empirical model that balances auto-acoustic compaction and shear dilatation.

Experiments using external acoustic vibration reveal the fundamental link between the intermediate shear-rate compaction and acoustic compaction, showing that the same magnitude of steady-state compaction is achieved for the same magnitude of acoustic vibration, regardless of whether it is applied externally or generated internally by shearing and grain collisions. The magnitude of internally generated acoustic vibration is dependent on the characteristics of the grains, and thus the phenomenon of auto-acoustic fludization occurs for angular grains, but not for quieter smooth grains.

The acoustic regime is activated when peak acoustic pressure from shear-induced vibration exceeds the confining stress. At 10 kPa confining stress, this transition occurs at a shear rate of only 1 mm/s in angular sand – four orders of magnitude below shear rates typical of the transition to inertial, dispersive granular flow.

Earthquake slip produces high frequency shaking both in the wake and in advance of a propagating rupture front. While the experimental conditions in this study are far from the conditions of fault zones, scaling the acoustic fluidization process up to seismogenic conditions suggests that this mechanism may be an important velocity weakening mechanism if confining stresses during earthquake rupture are sub-lithostatic.

Acknowledgements

N. van der Elst and E. E. Brodsky were supported by a grant from Institutional Support at Los Alamos National Lab via the Institute of Geophysics and Planetary Physics. P. Johnson and P.-Y. Le Bas were supported by Institutional Support via the LDRD Office at Los Alamos. We are indebted to our anonymous reviewers for very thorough and constructive reviews that have improved the clarity and organization of this article.

Appendix 3-A: Shear zone thickness

The shear zone in each experiment is restricted to a thin layer near the upper rotor, with displacement and shear rate decreasing rapidly with distance from the rotor. The exponential displacement profile is constant regardless of the shear rate, that is, the velocity profile changes only through a pre-factor proportional to the rotor velocity (Fig. 3-A1).

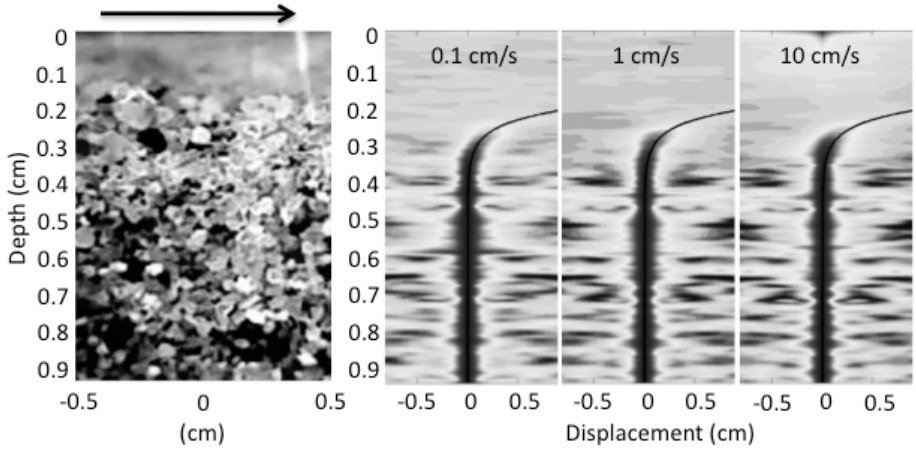

Figure 3-A1. Displacement profiles for different velocities. The left panel shows a snapshot of the angular sand, which is being sheared to the right. The following panels show horizontal cross-correlation of snapshots taken at a constant displacement (10 cm) but for different shear rates (0.1, 1, and rad/s from left to right). The darker colors reflect higher cross correlation coefficients. Grain rotation and non-horizontal particle motion prevent correlation beyond a few mm displacement. An exponential function (black curve) is fit to the first cross-correlation image (0.1 cm/s) and superposed on the adjacent panels. The shear-rate profile does not change except through a multiplicative pre-factor.

We image the active shear zone by cross-correlating video snapshots of the outer boundary using a high-definition webcam. Snapshots are taken at rim displacement

intervals of 10 cm for three representative velocities: 0.1, 1, and 10 cm/s. We then cross-correlate successive images to estimate horizontal lag as a function of depth. This involves taking a horizontal row of pixels from each pair of images and calculating the cross correlation function between the two. The lag corresponding to the maximum in the correlation function is taken as the horizontal displacement. We repeat this process for each row of pixels to get displacement as a function of depth away from the rotor. We then average the cross correlation function over 100 image pairs to produce the images in Figure 3-A1.

The shear rate profile with depth is well fit by an exponential function with a decay length scale of 0.63 mm, or approximately 2 grain diameters (Fig. 3-A1). We fit an exponential function to the peaks in the cross-correlation image for the shear rate of 0.1 cm/s, and then superpose this fit to the second two cross correlation images. No adjustment in the fit parameters is required to fit the profile at 1 cm/s and 10 cm/s. This is consistent with the results of Lu *et al*., [2007].

Appendix 3-B: Rheometer response to a sudden pressure drop.

The AR2000ex rheometer maintains normal pressure through a firmware feedback loop, adjusting the height of the rotor (gap) until the measured force falls within the bounds set by the controller software. The algorithm for adjusting the gap in response to a sudden drop in normal stress is not documented in the rheometer software, and thus the instrument response time after a sudden compaction event is unknown. We

perform a simple experiment in which we observe the rheometer response to a sudden compaction event (drop in pressure).

The experiment proceeds as follows: we place an air bladder (1 qt. Ziploc-style bag) on the rheometer platform (Figure 3-B1). A corner of the bag is pinched to reduce the internal volume and increase the pressure. The rotor is then lowered until it compresses the bag and a normal force of 1 N is registered by the rheometer. Finally, the constriction on the bag is then suddenly released, resulting in a rapid drop in pressure. We then observe the change in gap (rotor height) with time (Figure 3-B2, inset). The experiment is repeated for pressure drops of ~0.5 and ~1 N, as well as for continuous pressure fluctuations induced by intermittently squeezing and releasing the bag.

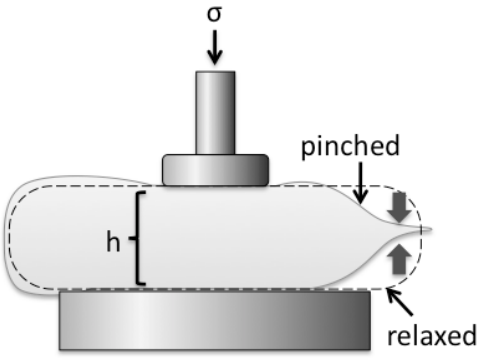

Figure 3-B1. Cartoon of experimental setup. The rheometer rotor is lowered into contact with an inflated plastic bag, which is pinched on the edge to increase the pressure. At the start of the experiment, the bag is released, resulting in a sudden relaxation in pressure (dashed outline).

We find that while the rheometer responds continuously to continuous pressure fluctuations, it has a significantly delayed response to a sudden pressure drop. The gap decreases gradually at first, before accelerating over ~10 seconds, up to a maximum adjustment rate that is dependent on the deviation of the normal force from

the nominal value (25 μm/s/N) (Figure 3-B2). This response explains the prolonged drop in normal force in experiment SPS1 (Fig. 3-10), and means that the measured timescale for compaction in Section 3-3.6 (Experiments SPS1 and APS1) must be treated as an upper bound on the intrinsic compaction timescale.

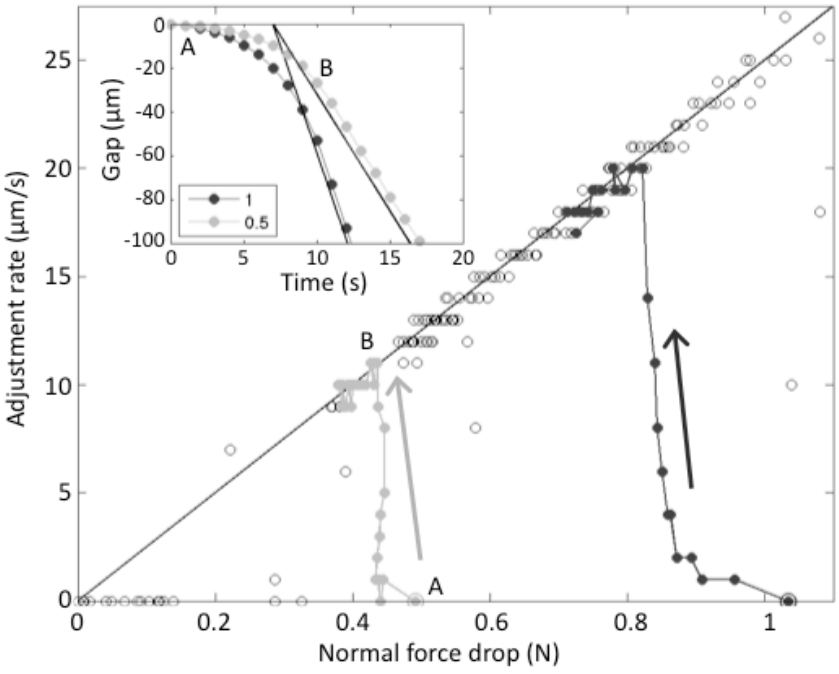

Figure 3-B2. Gap adjustment rate as a function of the reduction in normal force. Open circles show the response to continuous fluctuations in the resisting force. The maximum adjustment rate depends linearly on the deviation of normal force from the nominal value (25 μm/s/N), and the adjustment begins immediately. Filled circles show paths for the case of a sudden force drop, where the normal force is reduced from 1 N to 0.5 N (grey) or 0 N (black). For these sudden drops, there is a delayed rheometer response, during which the gap adjustment rate accelerates from zero (large circles at start of path) to the maximum rate over ~10 seconds. **Inset:** paths for sudden force drop experiments as a function of time, showing the ~10 second delay. The maximum rates are shown by straight lines for reference. Points A and B on the inset corresponds to points A and B along the path in the main figure.

References

Abrahamson, N., and W. Silva (2008), Summary of the Abrahamson and Silva NGA ground-motion relations, *Earthquake Spectra*, *24*(1), 67-97.

Aharonov, E., and D. Sparks (1999), Rigidity phase transition in granular packings, *Physical Review E*, *60*(6), 6890-6896.

Aki, K., and P. G. Richards (2002), *Quantitative seismology*, 2nd ed., xviii, 700 pp., University Science Books, Sausalito, Calif.

Ammon, C. J., T. Lay, and D. W. Simpson (2010), Great Earthquakes and Global Seismic Networks, *Seismological Research Letters*, *81*(6), 965-971.

Anderson, J. G., J. N. Brune, J. N. Louie, Y. H. Zeng, M. Savage, G. Yu, Q. B. Chen, and D. Depolo (1994), Seismicity in the Western Great Basin apparently triggered by the Landers, California, Earthquake, 28 June 1992, *Bulletin of the Seismological Society of America*, *84*(3), 863-891.

Atkinson, G. M., and D. M. Boore (1997), Some comparisons between recent ground motion relations, *Seismological Research Letters*, *68*(1), 24-40.

Bagnold, R. A. (1954), Experiments on a Gravity-Free Dispersion of Large Solid Spheres in a Newtonian Fluid under Shear, *Proceedings of the Royal Society of London Series a-Mathematical and Physical Sciences*, *225*(1160), 49-63.

Beeler, N. M., T. E. Tullis, M. L. Blanpied, and J. D. Weeks (1996), Frictional behavior of large displacement experimental faults, *Journal of Geophysical Research-Solid Earth*, *101*(B4), 8697-8715.

Beeler, N. M., and D. A. Lockner (2003), Why earthquakes correlate weakly with the solid Earth tides: Effects of periodic stress on the rate and probability of earthquake occurrence, *Journal of Geophysical Research*, *108*(B8), doi:10.1029/2001jb001518.

Ben-Naim, E., J. B. Knight, E. R. Nowak, H. M. Jaeger, and S. R. Nagel (1998), Slow relaxation in granular compaction, *Physica D*, *123*(1-4), 380-385.

Biegel, R. L., C. G. Sammis, and J. H. Dieterich (1989), The Frictional-Properties of a Simulated Gouge Having a Fractal Particle Distribution, *Journal of Structural Geology*, *11*(7), 827-&.

Boatwright, J., K. Thywissen, and L. C. Seekins (2001), Correlation of ground motion and intensity for the 17 January 1994 Northridge, California, Earthquake, *Bulletin of the Seismological Society of America*, *91*(4), 739-752.

Boatwright, J., H. Bundock, J. Luetgert, L. Seekins, L. Gee, and P. Lombard (2003), The dependence of PGA and PGV on distance and magnitude inferred from northern California ShakeMap data, *Bulletin of the Seismological Society of America*, *93*(5), 2043-2055.

Bocquet, L., W. Losert, D. Schalk, T. C. Lubensky, and J. P. Gollub (2001), Granular shear flow dynamics and forces: Experiment and continuum theory, *Physical Review E*, *65*(1)

Brodsky, E. E., V. Karakostas, and H. Kanamori (2000), A new observation of dynamically triggered regional seismicity: Earthquakes in Greece following the August, 1999 Izmit, Turkey earthquake, *Geophysical Research Letters*, *27*(17), 2741-2744.

Brodsky, E. E., E. Roeloffs, D. Woodcock, I. Gall, and M. Manga (2003), A mechanism for sustained groundwater pressure changes induced by distant earthquakes, *Journal of Geophysical Research-Solid Earth*, *108*(B8), doi:10.1029/2002jb002321.

Brodsky, E. E., and S. G. Prejean (2005), New constraints on mechanisms of remotely triggered seismicity at Long Valley Caldera, *Journal of Geophysical Research*, *110*(B4), doi:10.1029/2004jb003211.

Brodsky, E. E. (2006), Long-range triggered earthquakes that continue after the wave train passes, *Geophysical Research Letters*, *33*(15), L15313, Doi:15310.11029/12006gl026605.

Brodsky, E. E. (2009), The 2004-2008 worldwide superswarm, *Eos Trans. AGU*, *90*(52), Fall Meet. Suppl., Abstract S53B-06.

Caglioti, E., V. Loreto, H. J. Herrmann, and M. Nicodemi (1997), A "tetris-like" model for the compaction of dry granular media, *Physical Review Letters*, *79*(8), 1575-1578.

Campbell, C. S. (1990), Rapid Granular Flows, *Annual Review of Fluid Mechanics*, *22*, 57-92.

Campbell, C. S. (2005), Stress-controlled elastic granular shear flows, *Journal of Fluid Mechanics*, *539*, 273-297.

Campbell, C. S. (2006), Granular material flows - An overview, *Powder Technology*, *162*(3), 208-229.

Campbell, K. W., and Y. Bozorgnia (2007), Campbell-Bozorgnia NGA ground motion relations for the geometric mean horizontal component of peak and spectral ground motion parameters, Report 2007/02, Pac. Earthquake Eng. Res. Cent., Berkeley, Calif.

Casella, G., and R. L. Berger (2002), *Statistical inference*, 2nd ed., xxviii, 660 pp., Thomson Learning, Australia ; Pacific Grove, CA.

Cates, M. E., J. P. Wittmer, J. P. Bouchaud, and P. Claudin (1998), Jamming, force chains, and fragile matter, *Physical Review Letters*, *81*(9), 1841-1844.

Chambon, G., J. Schmittbuhl, and A. Corfdir (2006a), Frictional response of a thick gouge sample: 1. Mechanical measurements and microstructures, *Journal of Geophysical Research-Solid Earth*, *111*(B9), -.

Chambon, G., J. Schmittbuhl, and A. Corfdir (2006b), Frictional response of a thick gouge sample: 2. Friction law and implications for faults, *Journal of Geophysical Research-Solid Earth*, *111*(B9), -.

Clement, E. (1999), Rheology of granular media, *Current Opinion in Colloid & Interface Science*, *4*, 294-299.

Cochran, E. S., J. E. Vidale, and S. Tanaka (2004), Earth tides can trigger shallow thrust fault earthquakes, *Science*, *306*(5699), 1164-1166.

Coghill, P. C., P. J., and P. Giang (2011), Ultrasonic velocity measurements in powders and their relationship to strength in particles formed by agglomeration, *Powder Technology*, *208*(3), 694-701.

Corral, A. (2004), Long-term clustering, scaling, and universality in the temporal occurrence of earthquakes, *Physical Review Letters*, *92*(10), Doi 10.1103/Physrevlett.1192.108501.

Daniels, K. E., and R. P. Behringer (2005), Hysteresis and competition between disorder and crystallization in sheared and vibrated granular flow, *Physical Review Letters*, *94*(16)

Dieterich, J. (1994), A Constitutive Law for Rate of Earthquake Production and Its Application to Earthquake Clustering, *Journal of Geophysical Research-Solid Earth*, *99*(B2), 2601-2618.

Dijksman, J. A., G. H. Wortel, L. T. H. van Dellen, O. Dachot, and M. van Hecke (2011), Jamming, yielding and rheology of weakly vibrated granular media, *Physical review Letters*, *107*(10), 108303.

Elkhoury, J. E., E. E. Brodsky, and D. C. Agnew (2006), Seismic waves increase permeability, *Nature*, *441*(7097), 1135-1138.

Felzer, K. R., T. W. Becker, R. E. Abercrombie, G. Ekstrom, and J. R. Rice (2002), Triggering of the 1999 M-W 7.1 Hector Mine earthquake by aftershocks of the 1992 M-W 7.3 Landers earthquake, *Journal of Geophysical Research*, *107*(B9), doi:10.1029/2001jb000911.

Felzer, K. R., R. E. Abercrombie, and G. Ekstrom (2004), A common origin for aftershocks, foreshocks, and multiplets, *Bulletin of the Seismological Society of America*, *94*(1), 88-98.

Felzer, K. R., and E. E. Brodsky (2005), Testing the stress shadow hypothesis, *Journal of Geophysical Research*, *110*(B5), B05S09.

Felzer, K. R., and E. E. Brodsky (2006), Decay of aftershock density with distance indicates triggering by dynamic stress, *Nature*, *441*(7094), 735-738.

Freed, A. M., and J. Lin (1998), Time-dependent changes in failure stress following thrust earthquakes, *Journal of Geophysical Research*, *103*(B10), 24393-24409.

Freed, A. M. (2005), Earthquake triggering by static, dynamic, and postseismic stress transfer, *Annual Review of Earth and Planetary Sciences*, *33*, 335-367.

Gardner, J. K., and L. Knopoff (1974), Sequence of Earthquakes in Southern-California, with Aftershocks Removed, Poissonian, *Bulletin of the Seismological Society of America*, *64*(15), 1363-1367.

Gasperini, P., and B. Lolli (2006), Correlation between the parameters of the aftershock rate equation: Implications for the forecasting of future sequences, *Physics of the Earth and Planetary Interiors*, *156*(1-2), 41-58.

GDR Midi (2004) On dense granular flows, *Eur. Phys. J. E, 14,* 341-365

Gomberg, J., and D. Agnew (1996), The accuracy of seismic estimates of dynamic strains: An evaluation using strainmeter and seismometer data from Pinon Flat Observatory, California, *Bulletin of the Seismological Society of America*, *86*(1), 212-220.

Gomberg, J., and S. Davis (1996), Stress strain changes and triggered seismicity at The Geysers, California, *Journal of Geophysical Research*, *101*(B1), 733-749.

Gomberg, J., M. L. Blanpied, and N. M. Beeler (1997), Transient triggering of near and distant earthquakes, *Bulletin of the Seismological Society of America*, *87*(2), 294-309.

Gomberg, J. (2001), The failure of earthquake failure models, *Journal of Geophysical Research-Solid Earth*, *106*(B8), 16253-16263.

Gomberg, J., P. A. Reasenberg, P. Bodin, and R. A. Harris (2001), Earthquake triggering by seismic waves following the Landers and Hector Mine earthquakes, *Nature*, *411*(6836), 462-466.

Gomberg, J., P. Bodin, and P. A. Reasenberg (2003), Observing Earthquakes Triggered in the Near Field by Dynamic Deformations, *Bulletin of the Seismological Society of America*, *93*(1), 118-138.

Gomberg, J., P. Bodin, K. Larson, and H. Dragert (2004), Earthquake nucleation by transient deformations caused by the M=7.9 Denali, Alaska, earthquake, *Nature*, *427*(6975), 621-624.

Gomberg, J., and P. Johnson (2005), Seismology - Dynamic triggering of earthquakes, *Nature*, *437*(7060), 830-830.

Gomberg, J., and K. Felzer (2008), A model of earthquake triggering probabilities and application to dynamic deformations constrained by ground motion observations, *Journal of Geophysical Research-Solid Earth*, *113*(B10), B10317, doi:10310.11029/12007jb005184.

Grinstead, C. M., and J. L. Snell (1997), *Introduction to Probability*, American Mathematical Society.

Hainzl, S., F. Scherbaum, and C. Beauval (2006), Estimating background activity based on interevent-time distribution, *Bulletin of the Seismological Society of America*, *96*(1), 313-320.

Hardebeck, J. L., K. R. Felzer, and A. J. Michael (2008), Improved tests reveal that the accelerating moment release hypothesis is statistically insignificant, *Journal of Geophysical Research*, *113*(B8), B08310, doi:08310.01029/02007jb005410.

Harrington, R. M., and E. E. Brodsky (2006), The absence of remotely triggered seismicity in Japan, *Bulletin of the Seismological Society of America*, *96*(3), 871-878.

Helmstetter, A., and D. Sornette (2003), Predictability in the epidemic-type aftershock sequence model of interacting triggered seismicity, *Journal of Geophysical Research*, *108*(B10), doi:10.1029/2003jb002485.

Helmstetter, A., Y. Y. Kagan, and D. D. Jackson (2005), Importance of small earthquakes for stress transfers and earthquake triggering, *Journal of Geophysical Research*, *110*(B5), B05S08.

Hickman, S., R. Sibson, and R. Bruhn (1995), Introduction to Special Section - Mechanical Involvement of Fluids in Faulting, *Journal of Geophysical Research-Solid Earth*, *100*(B7), 12831-12840.

Hill, D. P., P. A. Reasenberg, A. Michael, W. J. Arabaz, G. Beroza, D. Brumbaugh, J. N. Brune, R. Castro, S. Davis, D. Depolo, W. L. Ellsworth, J. Gomberg, S. Harmsen, L. House, S. M. Jackson, M. J. S. Johnston, L. Jones, R. Keller, S. Malone, L. Munguia, S. Nava, J. C. Pechmann, A. Sanford, R. W. Simpson, R. B. Smith, M. Stark, M. Stickney, A. Vidal, S. Walter, V. Wong, and J. Zollweg (1993), Seismicity remotely triggered by the magnitude 7.3 Landers, California, Earthquake, *Science*, *260*(5114), 1617-1623.

Hill, D. P., and S. G. Prejean (2007), *Dynamic Triggering*, Treatise on Geophysics, Ed. H. Kanamori, Elsevier.

Hill, D. P. (2008), Dynamic stresses, Coulomb failure, and remote triggering, *Bulletin of the Seismological Society of America*, *98*(1), 66-92.

Holliday, J. R., D. L. Turcotte, and J. B. Rundle (2008), A review of earthquake statistics: Fault and seismicity-based models, ETAS and BASS, *Pure and Applied Geophysics*, *165*(6), 1003-1024.

Hough, S. E. (2005), Remotely triggered earthquakes following moderate mainshocks (or, why California is not falling into the ocean), *Seismological Research Letters*, *76*(1), 58-66.

Hutton, C. O. (1959), Mineralogy of beach sands between halfmoon and monterey bays, California, *California Div. Mines Spec. Rept.*, *59*

Iverson, R. M. (1997), The physics of debris flows, *Reviews of Geophysics*, *35*(3), 245-296.

Jaeger, H. M., S. R. Nagel, and R. P. Behringer (1996), Granular solids, liquids, and gases, *Reviews of Modern Physics*, *68*(4), 1259-1273.

Jia, X., C. Caroli, and B. Velicky (1999), Ultrasound propagation in externally stressed granular media, *Physical Review Letters*, *82*(9), 1863-1866.

Johnson, P. A., and X. Jia (2005), Nonlinear dynamics, granular media and dynamic earthquake triggering, *Nature*, *437*(7060), 871-874.

Johnson, P. A., H. Savage, M. Knuth, J. Gomberg, and C. Marone (2008), Effects of acoustic waves on stick-slip in granular media and implications for earthquakes, *Nature*, *451*(7174), 57-U55.

Johnson, P. A., B. M. Carpenter, M. Knuth, B. M. Kaproth, P.-Y. Le Bas, E. G. Daub, and C. Marone (in press 2012), Nonlinear dynamical triggering of slow-slip on simulated earthquake faults, *J. Geophys. Res.*

Jop, P., Y. Forterre, and O. Pouliquen (2006), A constitutive law for dense granular flows, *Nature*, *441*, 727-730.

Joyner, W. B., and D. M. Boore (1981), Peak Horizontal Acceleration and Velocity from Strong-Motion Records Including Records from the 1979 Imperial-Valley, California, Earthquake, *Bulletin of the Seismological Society of America*, *71*(6), 2011-2038.

Kagan, Y. Y., and D. D. Jackson (2000), Probabilistic forecasting of earthquakes, *Geophysical Journal International*, *143*(2), 438-453.

Kagan, Y. Y. (2004), Short-term properties of earthquake catalogs and models of earthquake source, *Bulletin of the Seismological Society of America*, *94*(4), 1207-1228.

Kilb, D., J. Gomberg, and P. Bodin (2000), Triggering of earthquake aftershocks by dynamic stresses, *Nature*, *408*(6812), 570-574.

King, G. C. P., R. S. Stein, and J. Lin (1994), Static Stress Changes and the Triggering of Earthquakes, *Bulletin of the Seismological Society of America*, *84*(3), 935-953.

Knight, J. B., C. G. Fandrich, C. N. Lau, H. M. Jaeger, and S. R. Nagel (1995), Density Relaxation in a Vibrated Granular Material, *Physical Review E*, *51*(5), 3957-3963.

Kuwano, O., and H. Takahiro (2011), Flash weakening is limited by granular dynamics, *Geophysical Research Letters*, *38*(L17305)

Lay, T., and T. C. Wallace (1995), *Modern Global Seismology*, Academic Press, San Diego.

Lei, X. L., C. D. Xie, and B. H. Fu (2011), Remotely triggered seismicity in Yunnan, southwestern China, following the 2004 M(w)9.3 Sumatra earthquake, *Journal of Geophysical Research*, *116*

Liu, A. J., and S. R. Nagel (1998), Nonlinear dynamics - Jamming is not just cool any more, *Nature*, *396*(6706), 21-22.

Liu, A. J., and S. R. Nagel (2010), The Jamming Transition and the Marginally Jammed Solid, *Annual Review of Condensed Matter Physics, Vol 1*, *1*, 347-369.

Love, A. E. H. (1927), *Mathematical Theory of Elasticity*, Cambridge Univ., Cambridge, UK.

Lu, K., E. E. Brodsky, and H. P. Kavehpour (2007), Shear-weakening of the transitional regime for granular flow, *Journal of Fluid Mechanics*, *587*, 347-372.

Lu, K., E. E. Brodsky, and H. P. Kavehpour (2008), A thermodynamic unification of jamming, *Nature Physics*, *4*(5), 404-407.

Mair, K., and C. Marone (1999), Friction of simulated fault gouge for a wide range of velocities and normal stresses, *Journal of Geophysical Research-Solid Earth*, *104*(B12), 28899-28914.

Majmudar, T. S., and R. P. Behringer (2005), Contact force measurements and stress-induced anisotropy in granular materials, *Nature*, *435*(7045), 1079-1082.

Makse, H. A., N. Gland, D. L. Johnson, and L. Schwartz (2004), Granular packings: Nonlinear elasticity, sound propagation, and collective relaxation dynamics, *Physical Review E*, *70*(6)

Marone, C., C. B. Raleigh, and C. H. Scholz (1990), Frictional Behavior and Constitutive Modeling of Simulated Fault Gouge, *Journal of Geophysical Research-Solid Earth and Planets*, *95*(B5), 7007-7025.

Marone, C. (1991), A Note on the Stress-Dilatancy Relation for Simulated Fault Gouge, *Pure and Applied Geophysics*, *137*(4), 409-419.

Marsan, D. (2003), Triggering of seismicity at short timescales following Californian earthquakes, *Journal of Geophysical Research-Solid Earth*, *108*(B5), Doi 10.1029/2002jb001946.

Matthews, M. V., and P. A. Reasenberg (1988), Statistical methods for investigating quiescence and other temporal seismicity patterns, *Pure and Applied Geophysics*, *126*(2-4), 357-372.

Mehta, A. (Ed.) (2007), *Granular Physics*, Cambridge Univ. Press, Cambridge.

Melosh, H. J. (1979), Acoustic Fluidization - New Geologic Process, *Journal of Geophysical Research*, *84*(Nb13), 7513-7520.

Melosh, H. J. (1996), Dynamical weakening of faults by acoustic fluidization, *Nature*, *379*(6566), 601-606.

Michael, A. J. (2011), Random variability explains apparent global clustering of large earthquakes, *Geophysical Research Letters*, *38*

Molchan, G. (2006), Interevent time distribution in seismicity: A theoretical approach by (vol 162, pg 1135, 2005), *Pure and Applied Geophysics*, *163*(7), 1453-1455.

Nalbant, S. S., S. Steacy, K. Sieh, D. Natawidjaja, and J. McCloskey (2005), Earthquake risk on the Sunda trench, *Nature*, *435*(7043), 756-757.

Nowak, E. R., J. B. Knight, M. L. Povinelli, H. M. Jaeger, and S. R. Nagel (1997), Reversibility and irreversibility in the packing of vibrated granular material, *Powder Technology*, *94*(1), 79-83.

Ogata, Y. (1992), Detection of precursory relative quiescence before great earthquakes through a statistical-model, *Journal of Geophysical Research*, *97*(B13), 19845-19871.

Ogata, Y. (1998), Space-time point-process models for earthquake occurrences, *Annals of the Institute of Statistical Mathematics*, *50*(2), 379-402.

Ogata, Y. (1999), Seismicity analysis through point-process modeling: A review, *Pure and Applied Geophysics*, *155*(2-4), 471-507.

Parsons, T. (2005), A hypothesis for delayed dynamic earthquake triggering, *Geophysical Research Letters*, *32*(4), L04302, doi:04310.01029/02004gl021811.

Parsons, T., and A. A. Velasco (2011), Absence of remotely triggered large earthquakes beyond the mainshock region, *Nature Geoscience*, *4*(5), 312-316.

Paull, C. K., P. Mitts, W. Ussler, R. Keaten, and H. G. Greene (2005), Trail of sand in upper Monterey Canyon: Offshore California, *Geological Society of America Bulletin*, *117*(9-10), 1134-1145.

Peng, Z., J. E. Vidale, M. Ishii, and A. Helmstetter (2007), Seismicity rate immediately before and after main shock rupture from high-frequency waveforms in Japan, *J. Geophys. Res.*, *112*(B03306)

Peng, Z. G., and P. Zhao (2009), Migration of early aftershocks following the 2004 Parkfield earthquake, *Nature Geoscience*, *2*(12), 877-881.

Peng, Z. G., D. P. Hill, D. R. Shelly, and C. Aiken (2010), Remotely triggered microearthquakes and tremor in central California following the 2010 M(w) 8.8 Chile earthquake, *Geophysical Research Letters*, *37*

Perfettini, H., and J. P. Avouac (2007), Modeling afterslip and aftershocks following the 1992 Landers earthquake, *Journal of Geophysical Research-Solid Earth*, *112*(B7), Doi 10.1029/2006jb004399.

Pollitz, F. F., R. Burgmann, and B. Romanowicz (1998), Viscosity of oceanic asthenosphere inferred from remote triggering of earthquakes, *Science*, *280*(5367), 1245-1249.

Pollitz, F. F., and M. J. S. Johnston (2006), Direct test of static stress versus dynamic stress triggering of aftershocks, *Geophysical Research Letters*, *33*(15), L15318 Artn l15318.

Prejean, S. G., D. P. Hill, E. E. Brodsky, S. E. Hough, M. J. S. Johnston, S. D. Malone, D. H. Oppenheimer, A. M. Pitt, and K. B. Richards-Dinger (2004), Remotely triggered seismicity on the United States west coast following the M-W 7.9 Denali fault earthquake, *Bulletin of the Seismological Society of America*, *94*(6), S348-S359.

Reasenberg, P. A., and L. M. Jones (1989), Earthquake hazard after a mainshock in California, *Science*, *243*(4895), 1173-1176.

Reynolds, O. (1885), On the dilatancy of media composed of rigid particles in contact, *Philos. Mag.*, *20*(469)

Rezapour, M., and R. G. Pearce (1998), Bias in surface-wave magnitude M-s due to inadequate distance corrections, *Bulletin of the Seismological Society of America*, *88*(1), 43-61.

Richter, C. F. (1935), An instrumental earthquake magnitude scale, *Bulletin of the Seismological Society of America*, *25*(1), 1-32.

Rubinstein, J. L., G. C. Beroza, J. Brown, M. Brudzinski, J. Gomberg, S. Malone, D. H. Oppenheimer, Z. G. Peng, S. G. Prejean, H. M. Savage, D. R. Shelly, A. Wech, and M. West (2011), Widespread triggering of earthquakes and tremor by the 2011 M9.0 off-Tohoku earthquake, *Seismological Research Letters*, *82*(2), 273-361.

Saichev, A., and D. Sornette (2006), "Universal" distribution of interearthquake times explained, *Physical Review Letters*, *97*(7), Doi 10.1103/Physrevlett.1197.078501.

Savage, H. M., and C. Marone (2008), Potential for earthquake triggering from transient deformations, *Journal of Geophysical Research*, *113*(B5), B05302, doi 05310.01029/02007jb005277.

Savage, S. B. (1984), The mechanics of rapid granular flows, *Adv. Appl. Mech*, *24*, 289-366.

Scholz, C. H. (2003), Earthquakes - Good tidings, *Nature*, *425*(6959), 670-671.

Shearer, P. M., and P. B. Stark (2011), Global risk of big earthquakes has not recently increased, *Proc. Natl. Acad. Sci.*, *109*(3), 717-721.

Shelly, D. R., Z. G. Peng, D. P. Hill, and C. Aiken (2011), Triggered creep as a possible mechanism for delayed dynamic triggering of tremor and earthquakes, *Nature Geoscience*, *4*(6), 384-388.

Sleep, N. H., and M. L. Blanpied (1992), Creep, Compaction and the Weak Rheology of Major Faults, *Nature*, *359*(6397), 687-692.

Sornette, D., and M. J. Werner (2005a), Apparent clustering and apparent background earthquakes biased by undetected seismicity, *Journal of Geophysical Research-Solid Earth*, *110*(B9), Doi 10.1029/2005jb003621.

Sornette, D., and M. J. Werner (2005b), Constraints on the size of the smallest triggering earthquake from the epidemic-type aftershock sequence model, Bath's law, and observed aftershock sequences, *Journal of Geophysical Research-Solid Earth*, *110*(B8), B08304, doi:08310.01029/02004jb003535.

Spudich, P., L. K. Steck, M. Hellweg, J. B. Fletcher, and L. M. Baker (1995), Transient Stresses at Parkfield, California, Produced by the M-7.4 Landers Earthquake of June 28, 1992 - Observations from the Upsar Dense

Seismograph Array, *Journal of Geophysical Research-Solid Earth*, *100*(B1), 675-690.

Stark, M. A., and S. D. Davis (1996), Remotely triggered microearthquakes at The Geysers geothermal field, California, *Geophysical Research Letters*, *23*(9), 945-948.

Stein, R. S., G. C. P. King, and J. Lin (1994), Stress triggering of the 1994 M=6.7 Northridge, California, earthquake by Its predecessors, *Science*, *265*(5177), 1432-1435.

Taira, T., P. G. Silver, F. L. Niu, and R. M. Nadeau (2009), Remote triggering of fault-strength changes on the San Andreas fault at Parkfield, *Nature*, *461*(7264), 636-U677.

Thompson, P. A. (1971), *Compressible-fluid dynamics*, McGraw-Hill, New York.

Toiya, M., J. Stambaugh, and W. Losert (2004), Transient and oscillatory granular shear flow, *Physical Review Letters*, *93*(8)

Tordesillas, A., J. Y. Shi, and T. Tshaikiwsky (2011), Stress-dilatancy and force chain evolution, *International Journal for Numerical and Analytical Methods in Geomechanics*, *35*(2), 264-292.

Umbanhowar, P., and M. van Hecke (2005), Force dynamics in weakly vibrated granular packings, *Phys. Rev. E.*, *72*(3)

Uspensky, J. B. (1937), *Introduction to Mathematical Probability*, McGraw-Hill, New York.

van der Elst, N. J., and E. E. Brodsky (2010), Connecting near-field and far-field earthquake triggering to dynamic strain, *J. Geophys. Res.*, *115*(B07311)

Veje, C. T., D. W. Howell, and R. P. Behringer (1999), Kinematics of a two-dimensional granular Couette experiment at the transition to shearing, *Physical Review E*, *59*(1), 739-745.

Velasco, A. A., S. Hernandez, T. Parsons, and K. Pankow (2008), Global ubiquity of dynamic earthquake triggering, *Nature Geoscience*, *1*(6), 375-379.

Wald, D. J., V. Quitoriano, T. H. Heaton, H. Kanamori, C. W. Scrivner, and C. B. Worden (1999), TriNet "ShakeMaps": rapid generation of peak ground motion and intensity maps in California, *Earthquake Spectra*, *15*, 537-556.

Wald, D. J., B. C. Worden, V. Quitoriano, and K. L. Pankow (2006), Shakemap manual: technical manual, user's guide, and software guide, Version 1.0, http://pubs.usgs.gov/tm/2005/12A01/

Walpole, R. E., and R. H. Myers (1989), *Probability and Statistics for Engineers and Scientists*, 4th ed., Macmillan Publishing Compant, New York.

Walton, K. (1987), The Effective Elastic-Moduli of a Random Packing of Spheres, *Journal of the Mechanics and Physics of Solids*, *35*(2), 213-226.

West, M., J. J. Sanchez, and S. R. McNutt (2005), Periodically triggered seismicity at Mount Wrangell, Alaska, after the Sumatra earthquake, *Science*, *308*(5725), 1144-1146.

Wiemer, S. (2000), Introducing probabilistic aftershock hazard mapping, *Geophysical Research Letters*, *27*(20), 3405-3408.

Wiseman, K., and R. Burgmann (2011), Stress and Seismicity Changes on the Sunda Megathrust Preceding the 2007 M(w) 8.4 Earthquake, *Bulletin of the Seismological Society of America*, *101*(1), 313-326.

Wu, C. Q., Z. G. Peng, W. J. Wang, and Q. F. Chen (2011), Dynamic triggering of shallow earthquakes near Beijing, China, *Geophysical Journal International*, *185*(3), 1321-1334.

Yamanaka, Y., and K. Shimazaki (1990), Scaling relationship between the number of aftershocks and the size of the main shock, *J. Phys. Earth*, *38*, 305-324.

Ziv, A. (2003), Foreshocks, aftershocks, and remote triggering in quasi-static fault models, *Journal of Geophysical Research-Solid Earth*, *108*(B10), Doi 10.1029/2002jb002318.